TRIBOLOGICAL THIN FILMS

ON STEEL ROLLING ELEMENT BEARING SURFACES

by

RYAN DAVID EVANS

Submitted in partial fulfillment of the requirements

For the degree of Doctor of Philosophy

Dissertation Adviser: Prof. Jeffrey T. Glass

Department of Chemical Engineering

CASE WESTERN RESERVE UNIVERSITY

January 2006

CASE WESTERN RESERVE UNIVERSITY

SCHOOL OF GRADUATE STUDIES

We hereby approve the dissertation of

_____

candidate for the Ph.D. degree *.

(signed)_____
                        (chair of the committee)

_____

_____

_____

_____

_____

(date) _____

*We also certify that written approval has been obtained for any
proprietary material contained therein.

Dedicated to

Melinda,

Kyle, Kaylee,

and the rest of my supportive family.

TABLE OF CONTENTS

LIST OF FIGURES

Chapter 4

Chapter 5

ACKNOWLEDGMENTS

Tribological Thin Films on Steel Rolling Element Bearing Surfaces

Abstract

by

RYAN DAVID EVANS

Tribological thin films are of interest to designers and end-users of friction management and load transmission components such as steel rolling element bearings. This study sought to reveal new information about the properties and formation of such films, spanning the scope of their technical evolution from natural oxide films, to antiwear films from lubricant additives, and finally engineered nanocomposite metal carbide/amorphous hydrocarbon (MC/a-C:H) films.

Transmission electron microscopy (TEM) was performed on the near-surface material (depth < 500 nm) of tapered roller bearing inner rings (cones) that were tested at two levels of boundary-lubricated conditions in mineral oil with and without sulfur- and phosphorus-containing gear oil additives. Site-specific thinning of cross-section cone surface sections for TEM analyses was conducted using the focused ion beam milling technique. Two types of oxide surface films were characterized for the cones tested in mineral oil only, each one corresponding to a different lubrication severity. Continuous and adherent antiwear films were found on the cone surfaces tested with lubricant additives, and their composition depended on the lubrication conditions. A sharp

interface separated the antiwear film and base steel. Various TEM analytical techniques were used to study the segregation of elements throughout the film volume.

The properties of nanocomposite tantalum carbide/amorphous hydrocarbon (TaC/a-C:H) thin films depend sensitively on reactive magnetron sputtering deposition process conditions. TaC/a-C:H film growth was studied as a function of three deposition parameters in designed experiments: acetylene flow rate, applied d.c. bias voltage, and substrate carousel rotation rate. Empirical models were developed for the following film characteristics to identify process-property trend relationships: Ta/C atomic ratio, hydrogen content, film thickness, TaC crystallite size, Raman spectrum, compressive stress, hardness, and elastic modulus. TEM measurements revealed the film base structure consisted of equiaxed cubic B1-TaC crystallites (< 5 nm) suspended in an a-C:H matrix. At the nanometer-scale, the film structure was lamellar with alternating TaC- and a-C:H-rich layers, the periodicity and distinctness of which were affected by deposition factors. The empirical property trends were interpreted with hypothesized growth mechanisms that incorporate elements of physical vapor deposition and plasma-enhanced chemical vapor deposition.

CHAPTER 1

INTRODUCTION[*]

1.1   TRIBOLOGICAL THIN FILMS

Tribology is the study of interacting surfaces in relative motion, including studies of the friction, lubrication, and wear of those surfaces. The word tribology is derived from the ancient Greek word *tribos*, which means "rub."

Thin films are material layers that cover a substrate and typically have a thickness on the order of one micrometer. Liquid thin films can exist on either liquid or solid surfaces. For example, the layer of lubricant that forms and separates two surfaces in relative motion is sometimes referred to as a "film" in hydrodynamic lubrication analyses. A "thin film" in the present context is limited to a solid layer attached to a solid surface.

Tribological thin films may be formed on interacting surfaces *in situ* by chemical reactions with species from the environment and/or lubricant. Alternatively, they may be deposited or formed intentionally on tribological surfaces prior to service with the goal of improving friction and wear performance. Regardless of their origin, tribological thin films can be beneficial or deleterious in an application, depending on film properties such as composition, structure, and/or mechanical properties. Thus, the topic of tribological thin films is important to designers and end-users of friction management and load transmission components such as steel rolling element bearings.

---

[*] Portions of this chapter have been published in: R. D. Evans, E. P. Cooke, C. R. Ribaudo, and G. L. Doll: Nanocomposite tribological coatings for rolling element bearings, in *Surface Engineering 2002 – Synthesis, Characterization and Applications*, edited by A. Kumar, W. J. Meng, Y. T. Cheng, J. S. Zabinski, G. L. Doll, and S. Veprek. (Mater. Res. Soc. Symp. **750**, Warrendale, PA, 2003).

1.2   ROLLING ELEMENT BEARINGS

Rolling element bearings are comprised of rolling elements such as balls, rollers, or needles that separate inner and outer rings. The rolling element type is determined by the application demands on the bearing, such as the loading mode. Tapered roller bearings have a versatile design that typically can accommodate both radial and thrust loads. As a result, both rolling and sliding tribological contact motions are present during operation [1]. Tapered roller bearings are used in many application areas such as industrial machinery, gear drives, passenger cars, light trucks, rolling mills, mining trucks, aircraft, and railroad cars.

In a tapered roller bearing, the rollers are truncated cones that ride between an inner ring (cone) that has two retaining lips (ribs) and a lipless outer ring (cup). A cage separates the rollers and holds them in position against the cone. A schematic of a tapered roller bearing is shown in Figure 1.1. Sliding occurs between the large ends of the rollers and the larger cone rib with elliptical contact geometry. Rolling line contact is experienced between the roller bodies and the cup/cone raceways. There is sliding contact between the rollers and the cages.
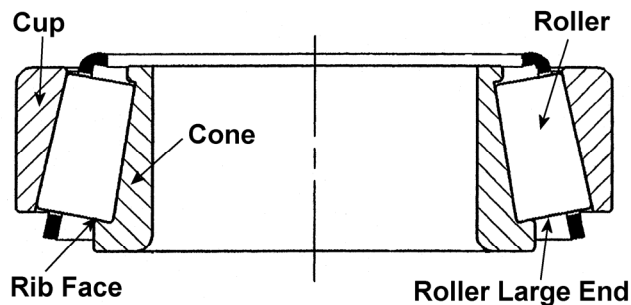
Figure 1.1. Schematic of a tapered roller bearing.

1.3   TECHNOLOGY EVOLUTION OF TRIBOLOGICAL THIN FILMS

Surfaces in rolling and/or sliding tribological contact within steel tapered roller bearings are susceptible to wear. Scuffing is a form of adhesive wear that occurs when "clean" steel asperity surfaces micro-weld and tear while in intimate contact. The use of an organic lubricant such as mineral oil can help minimize adhesive wear by separating the surfaces through hydrodynamic forces. However, oil alone cannot prevent the occurrence of scuffing under boundary lubrication conditions when surface asperities from the opposing surfaces are in frequent direct contact. Boundary lubrication conditions can occur in bearings at low speeds, high temperatures, in low viscosity oils, or during oil-out conditions. It was recognized by Bjerk [2] and others that scuffing in mineral oil can be delayed in the presence of atmospheric oxygen. A "natural" oxide layer was detected with microprobe analysis on roller surfaces tested in mineral oil without additives. Identical tests in a nominally oxygen-free environment produced scuffing under comparatively milder tribological conditions. Batchelor et al. [3] reviewed possible models for natural oxide layer formation on steel wear surfaces, but indicated the need for further experimental knowledge about the physical state of worn oxide films. Given the unavoidable occurrence of an oxygenated environment (i.e., air) around lubricated steel contacts, it is likely that natural oxide films were the first technically useful thin films in bearings.

Reliance upon oxide formation in steel tribological contacts as the main protection against scuffing presumably left the design engineer at the mercy of many variables, such as environment, temperature, the lubricant's tendency to absorb oxygen or form acids, and the severity of boundary lubrication conditions. The formation tendencies of natural

oxide films were difficult to control, and their wear protection was minimal. Engineers recognized in the early 1900's that adding chemicals to the lubricant could offer some measure of control by creating "antiwear" thin films in steel contacts. The chronology of lubricant additive development is outlined in a review by Spikes [4]. Additives that were used to promote "oiliness" were first used in marine applications in 1918. Many of the other general classes of additives such as pour point depressants, extreme pressure (EP) additives, antioxidants, corrosion inhibitors, detergents, and antiwear (AW) additives were developed in the 1930's to 1950's. This rapid development was in response to the rapid growth of the automobile and aircraft industries during that period [4]. Although extensive work has been conducted on lubricant additives, especially zinc dialkyl dithiophosphate (ZDDP) [4,5], many details about the structure of thin antiwear films that form on contact surfaces in real tribological components remain to be explored.

A desired end result of lubricant additives is the controlled formation of a thin film on steel tribological surfaces that make them more wear- or scuff-resistant. For many years, engineers have used electrolytic or chemical conversion treatments such as black oxiding, phosphating, sulfiding, and thin-dense chrome plating to create thin film layers on tribological surfaces prior to service, albeit with limited control over film properties such as adhesion or wear resistance. These limitations were overcome in the 1980's when *in vacuo* plasma discharge thin film deposition processes were developed for steel substrates. Films could be engineered to have a broad range of mechanical and tribological properties, thus reducing the uncertainties associated with *in situ* natural oxide or lubricant additive antiwear film formation. One technically useful film variety was "nanocomposite" metal carbide incorporated amorphous hydrocarbon (MC/a-C:H)

18

thin film coatings, which were first offered commercially on rolling element bearing surfaces in 1991 [6]. Since then, The Timken Company has developed and sold this type of thin film coating on bearing component surfaces to enhance performance [7]. The films typically contain ~2-10 nm metal carbide crystals dispersed in an amorphous hydrocarbon (a-C:H) matrix [8]. Hard a-C:H thin films have been referred to as "diamond-like" carbon (DLC), and they consist of a mostly amorphous mixture of interlinked Csp^3, Csp^2, and H atoms. The most popular structural model for a-C:H is that of an interlinked Csp^3 matrix with clustered graphitic (or graphene) inclusions and interspersed hydrogen [9]. Nanocomposite structures can be very hard and wear resistant in general. Veprek [10] suggested that the enhanced mechanical properties of such films might be related to the lack of dislocations in nanocrystals and the inability of nano-cracks to propagate through the amorphous matrix. Furthermore, MC/a-C:H films typically have a high ratio of hardness to elastic modulus, making them especially wear resistant and durable in tribological applications [11]. Precise control over the nanometer-scale film structure features during growth is possible using magnetron sputtering physical vapor deposition with a blended reactive/inert gas plasma, i.e., reactive sputtering. Reactive sputtering process fundamentals employed in the deposition of MC/a-C:H films have not yet been fully developed in texts, but several references describe the basic elements of physical and plasma-enhanced chemical vapor deposition [12,13,14].

Interestingly, the evolution of tribological thin film technology for bearings seems to be consistent with a general technology development pattern type that is taught by TRIZ researchers (Russian acronym for the "Theory of Inventive Problem Solving" [15]). The

properties of thin films on the surfaces of bearing components have become increasingly controllable over time. This is consistent with the "action coordination" TRIZ line of evolution, which suggests a technology trend of non-coordinated action to partially-coordinated action to fully-coordinated action [16]. "Action" in this example is the tribological performance, which is intimately related to the film properties. A schematic of this analogy for tribological thin films on bearing surfaces is shown in Figure 1.2.

"Natural" oxide formation by environment (*in situ*)	→	Antiwear film formation by lubricant additives (*in situ*)	→	Engineered thin films deposited prior to service (*ex situ*)
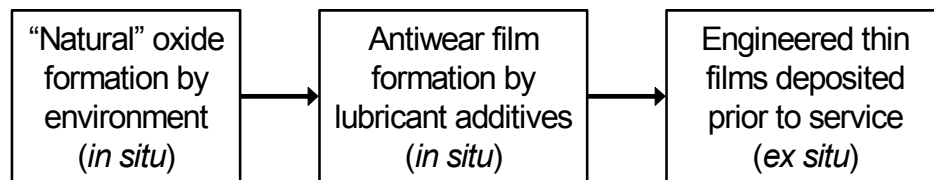
Figure 1.2. Evolution of tribological thin films on steel rolling element bearing surfaces.

1.4   TECHNICAL BENEFITS OF THIN FILMS IN BEARINGS

Surface-initiated failures limit the life of modern rolling element bearings, and their occurrence may be minimized by using tribological thin films. One hundred years of research to optimize steel cleanliness, bearing geometries, and grinding/honing treatments have shifted the primary bearing failure modes from the bulk material to the raceway surfaces. In demanding applications with low lubrication, high load, debris, low rotational speed, or oscillatory motion, the intentional use of tribological thin films on bearing surfaces with pre-designed properties may be necessary to achieve adequate bearing performance.

Natural oxide thin films offer some measure of adhesive wear protection [2] as mentioned in Section 1.3. Antiwear thin films that are deposited during service from lubricant chemical additives may also help minimize adhesive wear and scuffing.

Antiwear film formation can be thermally-activated, and/or it may require "extreme pressure" asperity contact events for reactions to occur that produce easy-shear compounds [17]. Thin films deposited prior to service can also improve surface mechanical properties and wear resistance. MC/a-C:H thin films have been shown to improve fatigue life in clean and debris-laden lubricant, delay rib-roller end scuffing under "oil-out" conditions, and to minimize false brinelling damage in steel rolling element bearings [18,19]. These benefits were attributed to two tribological effects: (i) minimization of adhesive interactions in the contact, and (ii) micro-polishing of uncoated counterface asperities, thereby increasing the separation of surfaces by lubricant in the contact. The following discussion addresses these mechanisms in greater detail.

Adhesive wear is due to the adhesion of asperity tips in a contact, followed by destructive transfer of one material to the other. Severe instances of adhesive wear in poorly lubricated conditions are often termed "scuffing" or "galling." In general, minimization of adhesive wear is achieved by using non-welding, insoluble, non-wetting, low surface energy, low ductility, high-hardness material pairs [20]. It is well known that MC/a-C:H films can have higher hardness values than bearing steels (e.g., $H_{steel} \sim 7$ GPa and $H_{MC/a-C:H} \sim 11$-20 GPa), and it is qualitatively accepted that MC/a-C:H films do not dissolve or weld with steel counterfaces. More importantly, the following discussion is intended to demonstrate how the low surface free energy of MC/a-C:H films is important in preventing damaging adhesive interactions with steel. These principles are applicable to any tribological thin film with a low surface free energy relative to steel.

The relationship between surface free energies and adhesion of solids is demonstrated by considering an ideal unlubricated a-C:H/steel contact in air. The work of adhesion ($W_{a-C:H/Steel}$) is given by [21]:

$$W_{a-C:H/Steel} = \gamma_{a-C:H} + \gamma_{Steel} - \gamma_{a-C:H/Steel} \qquad (1.1)$$

where $\gamma_{a-C:H}$ is the surface free energy (surface tension) of the a-C:H film coated surface, γ_{Steel} is the surface free energy of the steel surface, and $\gamma_{a-C:H/Steel}$ is the interface energy. Practically, the work of adhesion represents the amount of work per unit area necessary to separate the interface into two new solid-air interfaces. Many of the popular formulae for "pull-off forces" are directly proportional to the work of adhesion [22]. Surface free energy values for MC/a-C:H films have not been reported in the literature so the subsequent calculations were made for undoped a-C:H (the matrix material for MC/a-C:H films). Contributions due to native oxide films or absorbed gases on the solids are also neglected in this ideal scenario. Grischke et al. [23] reported values of $\gamma_{a-C:H} = 41.3$ mN/m and $\gamma_{Steel} > 1000$ mN/m. A value for $\gamma_{a-C:H/Steel}$ is much more difficult to measure. To account for the general uncertainty of measuring interfacial free energies, Good and Girifalco [24] proposed that the work of adhesion could be expressed alternatively as:

$$W_{a-C:H/Steel} = 2\,\Phi\sqrt{\gamma_{a-C:H}\gamma_{Steel}} \qquad (1.2)$$

where Φ is the Good-Girifalco interaction parameter that corrects for intermolecular interaction across the interface. Unfortunately, the computation of this parameter is not very straightforward. In the rigorous calculation, Φ is represented as a function of the appropriate Hamaker coefficients for the interface and the interfacial separation difference. Chaudhury [25] presented a review of these techniques, and noted that Φ

often falls between 0.5 and 1, with $\Phi = 1$ for the case when the two contacting materials interact only by London dispersion forces. The $\Phi = 1$ assumption is not unreasonable for the a-C:H/steel interface, and so Equation 1.2 gives the following values, appropriate for relative comparisons: $W_{\text{a-C:H/Steel}} \sim 406$ mN/m and $W_{\text{Steel/Steel}} \sim 2000$ mN/m.

Rabinowicz [26] suggested a similar heuristic approach for estimating work of adhesion values for relative comparisons. His analysis of published data suggested that interface energy values tended to be approximately 0.25 - 0.5 of the sum of the individual surface free energies. Therefore, for two materials a and b:

$$
\begin{aligned}
&(i) \quad W_{ab} \approx 2\gamma_a \\
&(ii) \quad W_{ab} \approx \frac{3}{4}\left(\gamma_a + \gamma_b\right) \qquad\qquad (1.3)\\
&(iii) \quad W_{ab} \approx \frac{1}{2}\left(\gamma_a + \gamma_b\right)
\end{aligned}
$$

where (i) is for the case where a and b are identical, (ii) is for when a and b are "compatible," and (iii) is for when a and b are "incompatible." Since a-C:H and steel are insoluble and do not readily form compounds, Equation 1.3(iii) is used to estimate $W_{\text{a-C:H/Steel}} \sim 521$ mN/m and Equation 1.3(i) to obtain $W_{\text{Steel/Steel}} \sim 2000$ mN/m as a comparison. Using the Good-Girifalco and Rabinowicz techniques to compute approximate work of adhesion values, it was shown that less energy is required to separate the a-C:H/steel interface than the steel/steel interface under ideal conditions.

The ability to minimize solid-solid adhesion tendencies between bearing surfaces in poorly lubricated rolling contact is desirable. Giannakopoulos et al. [27] addressed the role of solid-solid adhesion in contact fatigue. In that work, a tensile square root singularity in the raceway stress field was identified at the edges of the contact radius for adhesive contacts. Such tensile stresses may increase the tendency for contact fatigue

crack initiation. On the other hand, it was shown that the raceway stress field was Hertzian and compressive for non-adhesive contacts. Simplistically, the role of adhesion on contact fatigue can be envisioned as the mechanical difference between pushing plus pulling versus only pushing between contacting surface asperities [28]. In well-lubricated bearings, the effects of solid-solid adhesion on contact fatigue and surface wear are not a primary concern. However, for boundary lubrication conditions that are often present in bearings during false brinelling, oil-out, or start-up situations, tribological thin films can help minimize the damaging effects of solid-solid adhesion.

MC/a-C:H thin film coatings can also increase bearing life in poorly lubricated conditions by micro-polishing the asperities on uncoated mating surfaces. Such counterface polishing by hard coatings is a well-documented effect. Wei et al. [29] attributed increases in rolling contact fatigue life of a-C:H coated rods in "three-ball-on-rod" tests to the polishing effect of the coating on the counterface balls that increases the separation of surfaces by lubricant in the contacts. Polonsky et al. [30] concluded the same for TiN coated rods in rolling contact fatigue tests. Harris and Weiner [31] developed a method to quantify the effects of thin film coatings on the average wear rate of uncoated steel via a power-law model:

$$\overline{A(n)} = \alpha \, n^{\beta} \qquad\qquad (1.4)$$

where $A(n)$ is the average abrasion rate of the steel, n is the number of sliding passes or cycles, α is the degree of abrasiveness, and β represents the durability of the film's abrasive nature. For example, a highly abrasive film has a large value of α relative to a non-abrasive film. The bounds on β are $-1 < \beta < 0$, where $\beta = 0$ for a film that never loses its abrasiveness and $\beta = -1$ for a film that loses its abrasive qualities immediately

after the first sliding cycle. Pin-on-disk testing was conducted to obtain α and β values for sample TiC/a-C:H and WC/a-C:H thin films. The results are presented in Figure 1.3. The results indicate that the WC/a-C:H film had a higher overall abrasiveness than the TiC/a-C:H film because $\alpha_{WC/a\text{-}C:H} > \alpha_{TiC/a\text{-}C:H}$. However, the abrasive nature of the TiC/a-C:H lasts for more cycles than that of the WC/a-C:H since $\beta_{TiC/a\text{-}C:H} > \beta_{WC/a\text{-}C:H}$. In these tests, it appeared that the harder film imparted abrasive wear by plastic deformation to the steel ball (pin), as evidenced by the appearance of ridges and valleys in the ball wear scar.
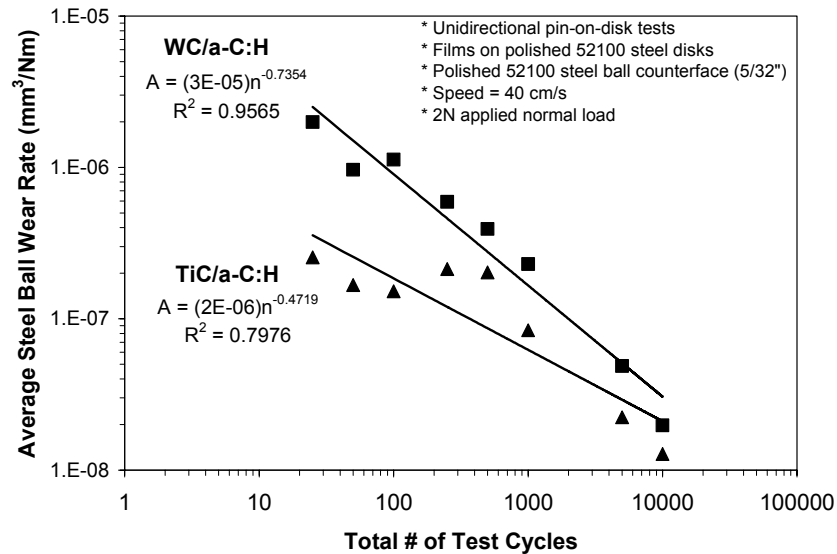
Figure 1.3. Coating abrasiveness against uncoated steel balls in dry sliding.

While the mating steel surface appeared to experience abrasive wear by the hard coating in unlubricated dry sliding, the MC/a-C:H film appeared to wear via a chemical-mechanical polishing mechanism. Atomic force microscopy and scanning electron microscopy of MC/a-C:H films at various stages of wear indicated that the asperity tips were gradually flattened and polished as the number of cycles increased during pin-on-disk tests against steel. Figure 1.4 shows transmission electron micrographs of TiC/a-

C:H wear debris particles from unlubricated sliding against steel in air. The inset selected area diffraction pattern was consistent with small crystalline graphite and metal-oxide particles (e.g., Fe_2O_3). These small particles appear as dark spots in the micrographs. The graphite particles were not present in the original film, but rather were formed in the contact as a result of tribochemical-mechanical interactions with the steel counterface. The Fe_2O_3 crystals were wear particles from the steel ball counterface. As unlubricated sliding occurs in air, it is believed that thin local surface layers of the MC/a-C:H film chemically react with the environment under high local heat and stress conditions to produce debris that may compact into a lubricating transfer film or "tribo-layer" [32]. Although the discussion accompanying Figures 1.3 and 1.4 directly applies to the results of unlubricated sliding tests, experience indicates that TiC/a-C:H and WC/a-C:H-coated rollers likewise micro-polish uncoated raceways in oil-lubricated bearings.
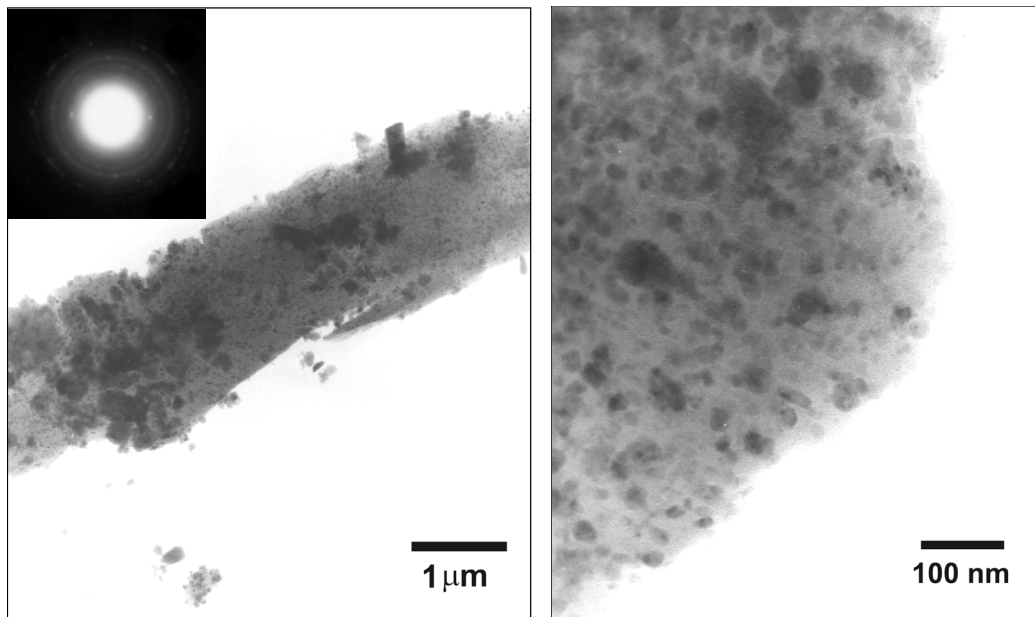
Figure 1.4. Transmission electron micrographs of TiC/a-C:H film wear debris from dry sliding pin-on-disk tests against steel.

1.5   OBJECTIVES AND OUTLINE

The discussions thus far have highlighted several opportunities for further work on tribological thin films. The structure of natural oxide films on steel rolling element bearing surfaces as a function of tribological conditions has not been characterized in cross-section with nanometer-scale spatial resolution. The same holds true for antiwear films formed by conventional, commercially available gear oil additives. It was emphasized that films such as MC/a-C:H can work to improve bearing performance, and that their properties can be tailored for specific applications. However, an improved understanding of process-property relationships for reactive sputtering of MC/a-C:H is needed to improve the fundamental understanding of these films in wear applications and to probe the limits of nanocomposite material properties.

The present research seeks to address those objectives by:

- Characterizing the cross-sectional composition and structure of naturally-occurring oxide films and additive antiwear films on real bearing surfaces as a function of contact severity (Chap. 2 & 3);

- Determining the impact of key deposition process conditions on the composition, structure, and mechanical properties of TaC/a-C:H thin films that could be used on bearing surfaces to improve performance (Chap. 4 & 5);

- Proposing a schematic mechanistic understanding of the development of TaC/a-C:H film properties as a function of reactive sputter deposition conditions (Chap. 4 & 5);

- Further exploring the effects of a key process parameter, applied d.c. bias voltage, on the growth of TaC/a-C:H thin films (Chap. 6).

Chapters 2-6 were written to be stand-alone, including background, experimental details, results and analysis, discussion, and conclusions, such that an understanding of the entire dissertation is not required for the appreciation of one chapter/topic. Chapter 7 summarizes important results and conclusions from Chapters 2-6, and speculates about the direction of future work.

1.6   REFERENCES

1. T. A. Harris: *Rolling Bearing Analysis*, 2nd ed. (John Wiley & Sons, New York, 1984).

2. R. O. Bejerk: Oxygen – an 'extreme-pressure agent'. *ASLE Trans.* **16**, 97 (1973).

3. A. W. Batchelor, G. W. Stachowiak, and A. Cameron: The relationship between oxide films and the wear of steels. *Wear* **113,** 203 (1986).

4. H. Spikes: The history and mechanisms of ZDDP. *Tribol. Lett.* **17**, 469 (2004).

5. A. J. Gellman and N. D. Spencer: Surface chemistry in tribology. *Proc. I. Mech. E. Ser. J.* **216**, 443 (2002).

6. Balzers Balinit Product Catalog. (Balzers AG, Liechtenstein, 1991).

7. G. L. Doll and B. K. Osborn: Engineering surfaces of precision steel components, in *44th Annual Technical Conference Proceedings*. (Society of Vacuum Coaters, Philadelphia, PA, Apr. 21-26, 2001).

8. W. J. Meng, R. C. Tittsworth, J. C. Jiang, B. Feng, D. M. Cao, K. Winkler, and V. Palshin: Ti atomic bonding environment in Ti-containing hydrocarbon coatings. *J. Appl. Phys.* **88**, 2415 (2000).

9. J. Robertson: Diamond-like amorphous carbon. *Mater. Sci. Eng. R* **37**, 129 (2002).

10. S. Veprek: Electronic and mechanical properties of nanocrystalline composites when approaching molecular size. *Thin Solid Films* **297**, 145 (1997).

11. A. Leyland and A. Matthews: On the significance of the H/E ratio in wear control: a nanocomposite coating approach to optimised tribological behavior. *Wear* **246**, 1 (2000).

12. D. L. Smith: *Thin Film Deposition: Principles and Practice.* (McGraw Hill, Boston, 1995).

13. M. A. Lieberman and A. J. Lichtenberg: *Principles of Plasma Discharges and Materials Processing.* (John Wiley & Sons, New York, 1994).

14. D. M. Mattox: *Handbook of Physical Vapor Deposition (PVD) Processing.* (Noyes Publications, New Jersey, 1998).

15. G. Altshuller: *The Innovation Algorithm: TRIZ, Systematic Innovation and Technical Creativity.* (Technical Innovation Center, Worcester, MA, 2000).

16. D. Mann: *Hands-On Systematic Innovation.* (Creax, Belgium, 2002).

17. H. S. Hong, M. E. Huston, B. M. O'Connor, and N. M. Stadnyk: Evaluation of surface fatigue performance of gear oils. *Lubri. Sci.* **10**, 365 (1998).

18. R. D. Evans, E. P. Cooke, C. R. Ribaudo, and G. L. Doll: Nanocomposite tribological coatings for rolling element bearings, in *Surface Engineering 2002 – Synthesis, Characterization and Applications*, edited by A. Kumar, W. J. Meng, Y. T. Cheng, J. S. Zabinski, G. L. Doll, and S. Veprek. (Mater. Res. Soc. Symp. **750**, Warrendale, PA, 2003).

19. G. L. Doll, C. R. Ribaudo, and R. D. Evans: Engineered surfaces for steel rolling element bearings and gears, in *Materials Science & Technology Conference Proceedings* **2.** (New Orleans, LA, Sept. 26-29, 2004).

20. M. B. Peterson and W. O. Winer: *Wear Control Handbook.* (American Society of Mechanical Engineers, 1980).

21. A. W. Adamson and A. P. Gast: *Physical Chemistry of Surfaces*, 6th ed. (John Wiley & Sons, New York, 1997).

22. R. G. Horn: Measurement of Surface Forces and Adhesion, in *ASM Handbook: Vol. 18 - Friction, Lubrication, and Wear Technology.* (ASM International, 1992).

23. M. Grischke, A. Hieke, F. Morgenweck, and H. Dimigen: Variation of the wettability of DLC-coatings by network modification using silicon and oxygen. *Diam. Relat. Mater.* **7**, 454 (1998).

24. L. A. Girifalco and R. J. Good: A theory for the estimation of surface and interfacial energies. I. Derivation and application to interfacial tension. *J. Phys. Chem.* **61**, 904 (1957).

25. M. K. Chaudhury: Interfacial interaction between low-energy surfaces. *Mater. Sci. Eng. R* **16**, 97 (1996).

26. E. Rabinowicz: *Friction and Wear of Materials.* (John Wiley & Sons, New York, 1965).

27. A. E. Giannakopoulos, T. A. Venkatesh, T. C. Lindley, and S. Suresh: The role of adhesion in contact fatigue. *Acta. Mater.* **47**, 4653 (1999).

28. G. L. Doll: Internal memo. (The Timken Company, Canton, OH, Mar. 5, 2002).

29. R. Wei, P. J. Wilbur, M. J. Liston, and G. Lux: Rolling-contact-fatigue wear characteristics of diamond-like hydrocarbon coatings on steels. *Wear* **162-164**, 558 (1993).

30. I. A. Polonsky, T. P. Chang, L. M. Keer, and W. D. Sproul: A study of rolling-contact fatigue of bearing steel coated with physical vapor deposition TiN films: Coating response to cyclic contact stress and physical mechanisms underlying coating effect on the fatigue life. *Wear* **215**, 191 (1998).

31. S. J. Harris and A. M. Weiner: Scaling relationships for the abrasion of steel by diamondlike carbon coatings. *Wear* **223**, 31 (1998).

32. R. D. Evans, G. L. Doll, and J. T. Glass: Relationships between the thermal stability, friction, and wear properties of reactively sputtered Si-aC:H thin films. *J. Mater. Res.* **17**, 2888 (2002).

CHAPTER 2

NATURALLY-OCCURRING OXIDE FILMS[*]

2.1   INTRODUCTION

The near-surface material (depth < 500 nm) in a tribological contact directly influences lubrication, additive film formation, and wear while acting as a "gateway" for surface-initiated corrosion and cracking.   The near-surface material properties are important under boundary lubrication conditions, which are characterized by asperity-to-asperity contact due to a thin lubricant film and a higher probability of debris contamination interactions.   The film thickness parameter Λ, the ratio of minimum lubricant film thickness to the composite surface roughness, is commonly used to characterize the lubrication regime for tribological contacts.   Fein [1] generalized that boundary lubrication exists when $\Lambda \leq 1$ and partial boundary lubrication (or mixed lubrication) exists when $\Lambda \leq 2$.   Kato [2] schematically indicated similar conditions for mixed lubrication, but suggested that $\Lambda \leq 0.1$ for boundary lubrication.   Practically, asperity-to-asperity contact occurs in the mixed lubrication regime such that part of the load bearing area is in local boundary lubrication.   As Λ decreases, asperity contact and thus local boundary lubrication occurs over an increasing fraction of the total contact area.   Boundary and mixed lubrication regimes may exist in steel rolling element bearings during start-up, at low speeds, at high operating temperatures, or with too low lubricant viscosity.

---

[*] The primary contents of this chapter have been published in: R. D. Evans, K. L. More, C. V. Darragh, and H. P. Nixon: Transmission electron microscopy of boundary-lubricated bearing surfaces. Part I: Mineral oil lubricant. *Tribol. Trans.* **47**, 430 (2004).

The importance of surface durability in tribological contacts and bearings has been recognized for more than 100 years [3]. Previous materials characterization studies on steel tribological surfaces were focused mostly on the following areas: subsurface microstructural alterations due to contact [4,5,6,7,8], subsurface cracking [9,10], deformation of surface layers (e.g., white layers) [11,12,13,14], oxide film formation on surfaces [15,16,17,18,19,20,21,22], and wear debris analysis [23,24,25,26]. Transmission electron microscopy (TEM) was used to reveal nanometer-scale material features in several of these cases. For example, Bush et al. [4] studied subsurface stress affected zones in 52100 steel after rolling contact using TEM of replica samples. Martin et al. [5] further characterized "white etching" microstructural alterations in sections of SAE 52100 steel ball bearings using TEM with electropolished specimens. A cell structure within the "white areas" was reported following imaging and electron diffraction studies. Swahn et al. [6] and Voskamp et al. [7] studied martensite decay in subsurface structures after oil-lubricated rolling contact using TEM. Wang et al. [12,25] evaluated amorphous surface protrusions in worn 52100 steel surfaces via TEM of conventionally ion-thinned specimens. Rainforth et al. [22] used argon ion-milled TEM specimens to identify surface oxides such as Fe_3O_4 and to characterize surface structural changes (martensite $\rightarrow$ ferrite) in tool steel after unlubricated sliding experiments. Brin et al. [26] collected AISI 304 stainless steel pin-on-disk test wear debris on carbon grids for TEM analysis and identified a dominant martensite phase after sliding in aqueous lubricants.

Although there are a few examples of TEM analysis in surface durability studies, the most common methods of analyzing altered surfaces include optical metallography,

atomic force microscopy, scanning electron microscopy, and energy dispersive, Auger electron, x-ray photoelectron, infrared and Raman spectroscopies. Such techniques can reveal valuable information about surface structure, topography, and chemical composition, but none of them can directly image the structure and analyze composition at the nanometer-scale with the spatial resolution of TEM. Thus far, routine use of TEM for steel tribological surface analysis was hindered because of sample preparation complexities for metal surfaces with an oxide layer. Conventional electro-polishing techniques may thin subsurface metal while leaving thick non-transparent surface layers. Argon ion milling may thin the surface oxide layer, but damage the ductile subsurface metal. These difficulties can now be avoided due to the development of focused ion beam (FIB) techniques for preparing cross-section TEM samples. FIB sample preparation may be used for site-specific thinning of surface sections with minimal specimen damage. Electron microscopy investigations of many surface-related areas have benefited by advances in FIB sample preparation, including integrated circuits [27], thermal barrier coatings [28], and tribological coatings [29,30]. More et al. [31] applied FIB sample preparation techniques to study thin alumina scales on nickel-base alloys in cross-section. Muroga and Saka [32] evaluated ball bearing steel microstructures after rolling contact fatigue using FIB-prepared TEM samples. They reported that "bright etching areas" and the surrounding matrix consisted of either ferrite or tempered martensite using electron diffraction.

FIB sample preparation for TEM made it possible to evaluate the cross-sectional structure and composition of near-surface material from actual steel components. In the current study, TEM analyses were performed on the near-surface material from tapered

roller bearing inner rings (cones) that were tested at two levels of boundary-lubricated conditions with a mineral oil base stock. This materials tribology approach revealed information about near-surface microstructural alterations, crack initiation and propagation, and oxide surface films as a function of lubrication conditions. Unlike the Wang et al. [29] and Evans et al. [30] investigations of synthetic tribological coatings, the present study reports characterizations of naturally-occurring oxide films that form in tribological contacts.   Whereas Muroga and Saka [32] investigated subsurface microstructural changes in fatigued steel ball bearings using FIB samples, the present study focuses on near-surface material and surface films < 500 nm from the surface using cross-sectional views.

2.2   EXPERIMENTAL

Tapered roller bearings were evaluated in this study. Nominal dimensions for this bearing type are: 82.55 mm outer diameter, 41.28 mm bore, and 25.65 mm overall bearing width. The bearing material was case carburized 8119 steel with the nominal composition: 0.19 wt.% C, 0.80 wt.% Mn, 0.40 wt.% Cr, 0.30 wt.% Ni and 0.12 wt.% Mo. After heat-treating, the raceways were ground and honed. Optical microscopy of an untested inner ring (cone) raceway revealed a carburized case region containing tempered martensite, 20-25% retained austenite, and fine spheroidal carbides as expected. Bearing tests were performed using a four-bearing life test rig [33] with a 152 mm housing and 10 L oil sump. Each four-bearing set was tested continuously for seven days at 1800 rpm with 33.3 kN radial load per bearing (151% of the 1986 catalog load rating). The loading conditions corresponded to a cone-roller maximum contact pressure of ~2.2 GPa. The

estimated maximum shear stress was calculated to be ~663 MPa located ~119 μm below the surface. The lubrication regime was determined by the dimensionless film thickness parameter Λ, which was calculated using the following formula [1]:

$$\Lambda = \frac{h_{min}}{\sqrt{R_{q,\,cone}^2 + R_{q,\,roller}^2}} \qquad (2.1)$$

where h_{min} was the operating Grubin minimum lubricant film thickness [34] and R_q was the root-mean square roughness corresponding to the cone or roller. The lubricant film thickness was controlled by the inlet oil temperature of 60°C or 121°C, corresponding to Λ ~ 1.1 and 0.3, respectively. Timken Company algorithms were used to calculate h_{min} for each temperature given the initial tapered roller bearing geometry and test conditions. The R_q values were obtained before and after bearing testing using a Talysurf stylus profilometer. After the Λ ~ 1.1 tests were complete, the bearings were removed and new bearings were mounted in the test rig. The temperature of the lubricant was increased to 121°C, and the second seven-day test was started. The lubricant was not drained and refilled between tests. After testing, the bearings were dipped in a naphtha solvent, dried in air, and then stored in a dessicator.

An SAE 20 paraffinic mineral oil base stock without rust and oxidation inhibitors or other antiwear additives was used for the bearing tests. Mineral oil physical properties are given in Table 2-1. Samples of the mineral oil lubricant were collected after the first set of bearing tests at Λ ~ 1.1 and then after the tests at Λ ~ 0.3. The two bearing test lubricant samples and a sample of untested oil were evaluated to help rationalize results from the bearing surface analyses. Water content was evaluated using a CSC Aquapal III coulometric titrator. An ISL VH1 Houillon viscometer was used to verify the lubricant

35

viscosity at 40°C and 100°C. The chemical composition of the lubricants was verified using Philips PW2400 x-ray fluorescence equipment. The acidity of the lubricant samples was evaluated using a Mettler DL67 titrator following ASTM D664. The degree of lubricant oxidation was evaluated using a Nicolet 760 Fourier-transform infrared (FTIR) spectrometer.

Table 2-1. Untested mineral oil physical properties (nominal values).

Property	Value
Specific gravity ($H_2O = 1$)	0.90
Viscosity at 40°C	54.35 cSt
Viscosity at 100°C	7.78 cSt
Viscosity index	108
Acid number (mg KOH/g)	0.03

The cone component was selected for near-surface material analyses. The cones experience uniform cyclic stresses during radial loading and under the test conditions have a propensity for fatigue spalling. One cone from each set of tested bearings and one untested cone were ultrasonically cleaned in isopropyl alcohol for five minutes and then coated with a protective tungsten metal layer (~25 nm thick) using physical vapor deposition. Chemical composition depth profiling with x-ray photoelectron spectrometry was performed after tungsten coating to verify the coating thickness and confirm the preservation of the original surface structure and chemistry. A PHI 5600 ESCA system using an $Al_{K\alpha}$ monochromatic x-ray source and equipped with a PHI 04-303 sputter gun was used for this purpose. A Buehler Abrasimet 2 abrasive cutter and Buehler Isomet 4000 diamond-saw were used to cut the samples into small wafers suitable for further

TEM specimen preparation. Each wafer was cut from precisely the same cone raceway location as shown in Figure 2.1.

Figure 2.1. Approximate location of sample position on cone raceways.

The small wafers were thinned to < 75 μm using a diamond polishing wheel and then mounted with tested surface up on a crescent shaped ring for focused ion beam (FIB) milling. A Hitachi FB-2000 FIB system with a 30 kV beam of Ga+ ions was used to etch trenches at a shallow approach angle creating an electron transparent window < 100 nm thick.[†] Figure 2.2 is a scanning electron micrograph showing the cross-sectional orientation of the circumferential sections, consistent with the coordinates of Figure 2.1. The rectangular electron transparent window is visible in the center of the micrograph

---

[†] Comparisons of the samples studied in Chapters 2 and 3 with published images of electropolished steel samples suggest that sample damage during FIB preparation was minimal. For example, see W. E. Dowling, Jr., W. T. Donlon, W. B. Copple, and C. V. Darragh: The influence of heat treat process and alloy on the surface microstructure and fatigue strength of carburized alloy steel. *SAE Tech. Paper Ser.* 1999-01-0600 (1999).

and is located on the thin sliver between the trenches of removed material. Typical window dimensions were ~4 µm wide by 6 µm deep. TEM and energy dispersive spectroscopy (EDS) were performed using a Hitachi HF-2000 field emission gun analytical electron microscope equipped with a Thermo Electron (Noran) Ultra Thin Window EDS detector for compositional analyses. Comparisons of EDS spectral intensities were made after Fe-Kα peak normalization.
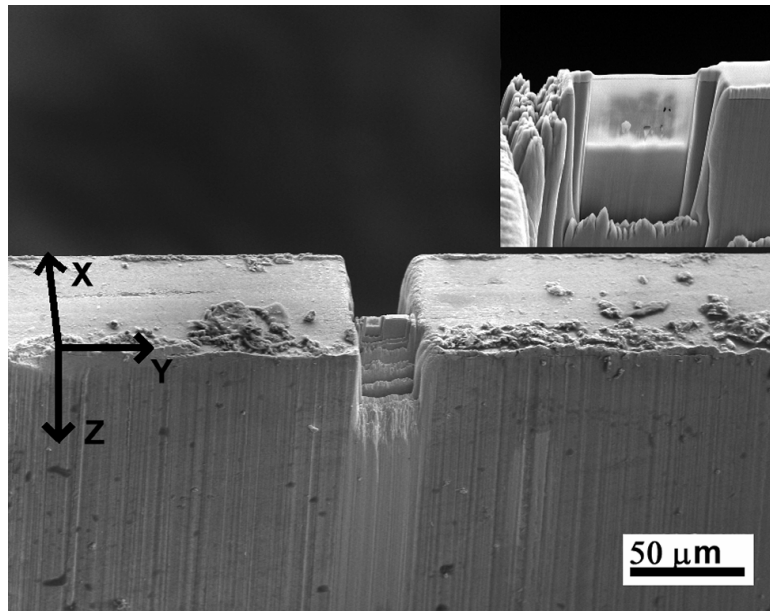
Figure 2.2. Scanning electron micrograph of a cone raceway TEM sample prepared using FIB milling. Inset is a magnified view of the electron-transparent window. Coordinates correspond to Figure 2.1.

2.3   RESULTS

2.3.1   Lubricant Evaluation

Lubricant analyses were performed on three samples: untested mineral oil, mineral oil from the 60°C bearing tests (Λ ~ 1.1), and mineral oil from the 121°C bearing tests (Λ ~ 0.3). The water content was lower than the 0.1 wt.% detection limit for every sample.

The lubricant viscosity, as measured at 40°C and 100°C, increased slightly from the 60°C bearing test sample to the 121°C bearing test sample. Low levels (< 0.09 wt%) of sulfur were detected in the oil samples using x-ray fluorescence spectroscopy. Titration measurements indicated that the lubricant total acid number (TAN) increased as the bearing test temperature increased. The mineral oil TAN was 0.03 mg KOH/g before testing, 0.12 mg KOH/g after the 60°C bearing test, and 0.91 mg KOH/g after the 121°C bearing test. There were no FTIR-detectable differences in lubricant oxidation between the initial mineral oil and the 60°C bearing test oil. However, the oil from the $\Lambda \sim 0.3$ bearing test (121°C) was oxidized as evidenced by an extension of the infrared spectrum peaks around 1715 cm^{-1} that suggests the presence of ketones, aldehydes, and carboxylic acids [35].

2.3.2   Cone Surfaces

Surface profilometry measurements were conducted after the bearing tests to identify major changes in the root-mean square roughness (R_q) of component surfaces. The number of measurements was insufficient for calculating statistically significant differences in R_q. However, the survey suggested that the roller R_q decreased slightly (on the order of ~0.05 μm), the outer ring (cup) load zone R_q increased slightly and the cone raceway R_q was unchanged during testing. No macroscopic evidence of cone raceway surface damage by micropitting, abrasive wear, or adhesive wear was detected by visual inspection after testing. X-ray photoelectron spectroscopy chemical depth profiles verified the presence of the tungsten (W) coating that was deposited on each cone raceway after the bearing tests. Furthermore, each tested cone sample had an oxygen-rich surface layer that was trapped and protected by the W-layer. The chemical shift in

the oxygen 1s peak was consistent with iron oxide or hydroxide. Trace levels of phosphorous were detected in the $\Lambda \sim 0.3$ cone surface layer that were attributed to minor test rig or lubricant contamination. The iron 2p peak shifts for the tested cones were attributable to iron (Fe), hematite (α-Fe_2O_3), or magnetite (Fe_3O_4), an admittedly ambiguous characterization due to slight chemical shift differences between the different Fe configurations.

2.3.3 TEM of an Untested Cone

A low magnification cross-section of the new cone surface is shown in Figure 2.3. The near-surface material (depth < 500 nm) was crystalline and fine-grained, while the subsurface bulk material (depth > 500 nm) consisted of larger grains. A grain size gradient existed in the radial direction with respect to the cone geometry. The grains became larger with increasing depth or distance from the raceway surface. Microstructural distortion was visible in the near-surface material (up to ~1 µm below the surface) as compared to the bulk. The distortion occurred in a direction parallel to the cone raceway surface (i.e., circumferential direction with respect to the cone geometry). Figure 2.4 shows a higher magnification view of the near-surface material. The near-surface grain size was on the order of ~20 nm, and the grain orientations appeared to be stratified. Irregular diffraction contrast throughout the near-surface material suggested a high dislocation density. The expected native oxide layer (~3 nm thick) was not clearly visible on this scale. Selected-area electron diffraction patterns (example inset in Figure 2.3) for the fine-grained near-surface material indicated that the grains were mostly ferrite (body-centered cubic iron). The symmetrical ring intensity in the near-surface diffraction patterns suggested high-angle grain boundaries were dominant. The larger-

grained subsurface material diffraction patterns consisted of spots rather than rings and also indicated ferrite. The presence of ferrous martensite (body-centered tetragonal) phases could not be excluded. Ferrite and martensite share many common plane spacings so precise phase differentiation is difficult, especially when mixtures of the two phases are present (overlap) and the rings and/or spots are diffuse. Electron diffraction patterns such as those inset in Figure 2.3 were directly interpretable as ferrite, but it is possible that martensite regions could be present as well. Direct electron diffraction pattern evidence of martensite and austenite (face-centered cubic iron) was found only at depths exceeding 2 μm.
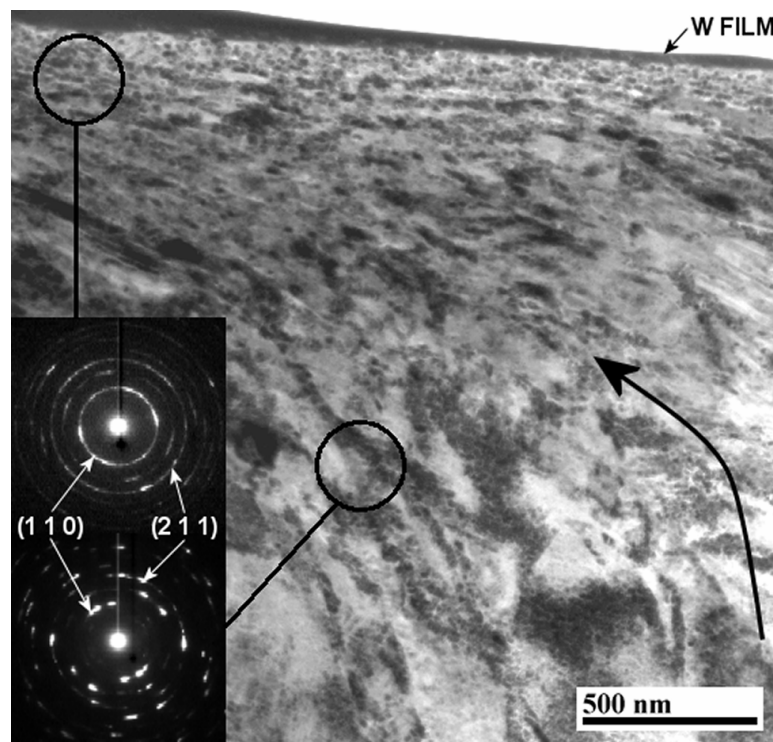
Figure 2.3. Cross-sectional TEM image from an untested cone raceway surface. The dark surface layer is a protective tungsten (W) thin film coating. Selected-area diffraction patterns from near-surface material and subsurface bulk material are inset. Miller indices correspond to ferrite.

Energy dispersive spectroscopy (EDS) results from two spots on the untested cone cross-section are shown in Figure 2.5. Fe, chromium (Cr), and manganese (Mn) were present as expected for 8119 steel. No oxygen within EDS detection limits was detected in the near-surface material or across the Fe/W-layer interface. No native oxide layer was detected by TEM imaging. A low level of gallium (Ga) was detected at the Fe/W-layer interface and was attributed to Ga ion implantation/contamination during FIB processing.
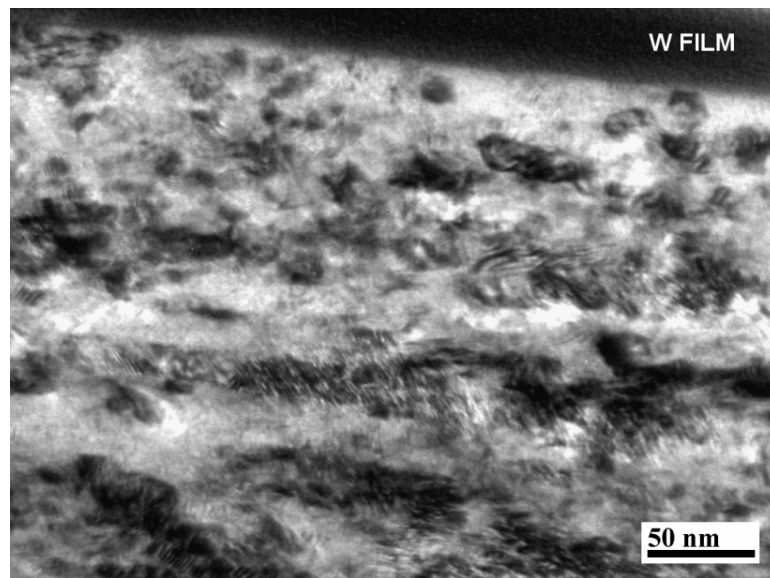
Figure 2.4. Higher magnification cross-sectional TEM image from an untested cone raceway surface.
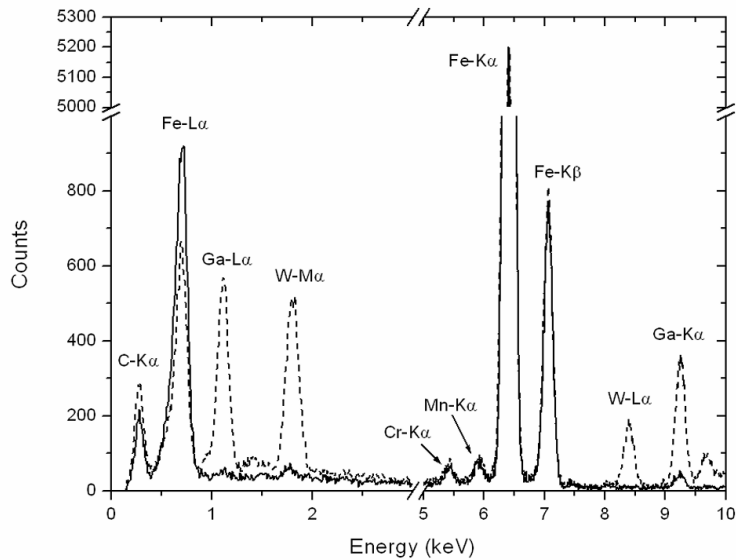
Figure 2.5. Energy dispersive spectroscopy (EDS) spectra from the untested cone. The solid line is from near-surface fine-grained material. The dashed line is from the surface/W film interface.

2.3.4 TEM of a Cone Tested at $\Lambda \sim 1.1$

A cone that was tested at $\Lambda \sim 1.1$ was examined in the same manner as the untested cone. The overall subsurface grain morphology (depth > 500 nm) was similar to that of the untested cone. However, the near-surface material was clearly different, as shown in Figure 2.6. The near-surface material was mostly crystalline, and included a ~50–150 nm thick surface layer with bright-contrast in the TEM images. The bright appearance results when a material is more electron transparent (less dense) or does not exhibit as much diffraction contrast as neighboring regions of material. A higher magnification image of the surface layer (Figure 2.7) shows diffraction contrast that indicates some degree of crystallinity within the layer. The surface layer was continuous across the top of the sample. The interface between the surface layer and underlying substrate material was somewhat diffuse in many areas. Selected-area and convergent-beam diffraction

(inset in Figures 2.6 and 2.7) indicated that the surface layer contained crystalline

material that was consistent with a mixture of magnetite (Fe_3O_4) and ferrite. The inset

convergent beam electron diffraction (CBED) pattern in Figure 2.7 is consistent with a

$[\bar{1}12]$ zone axis view of Fe_3O_4 that has an Fd-3m space group (f.c.c.). No conclusive

evidence of either α-Fe_2O_3 or $Fe_{1-x}O$ was detected in the diffraction patterns for the cone

with $\Lambda \sim 1.1$. Dark-field imaging on the (110) ferrite ring (that may contain contributions

from (101) martensite reflections) further confirmed the grain size gradient and presence

of crystalline ferrite in the surface layer.
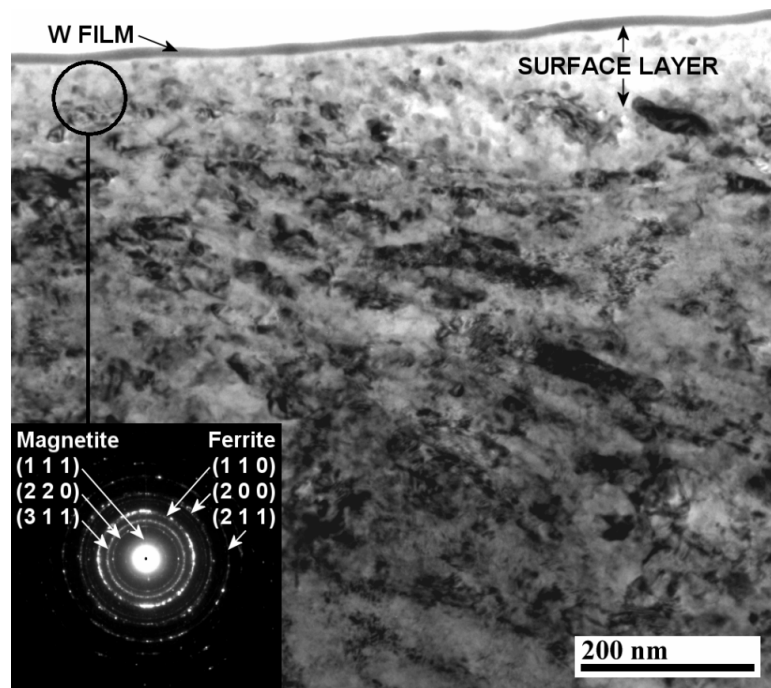
Figure 2.6. Cross-sectional TEM image from a cone tested at $\Lambda \sim 1.1$. The dark surface
layer is the protective W film. Inset is a SAD pattern from the bright near-surface
material. Rings suggesting the presence of magnetite and ferrite are labeled with
appropriate Miller indices.
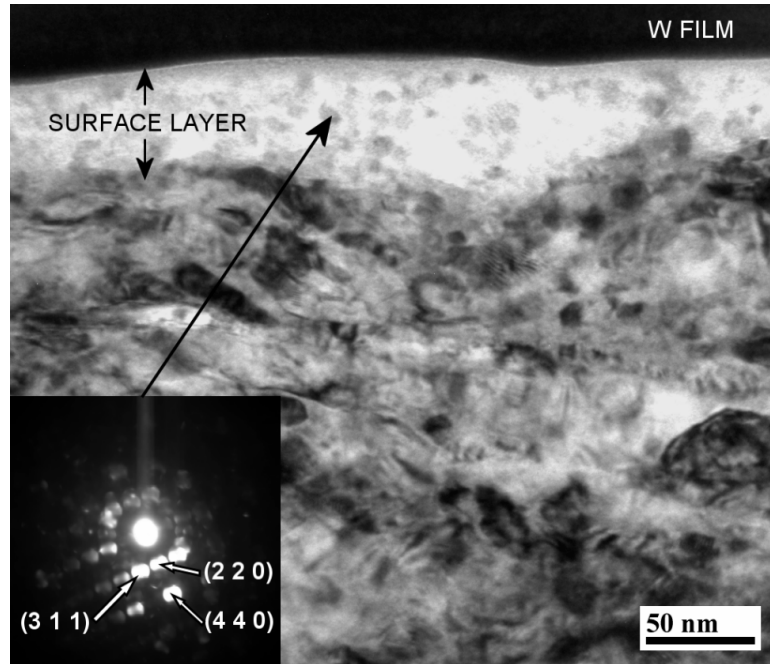
Figure 2.7. Higher magnification cross-sectional TEM image of the surface layer on the cone raceway that was tested at $\Lambda \sim 1.1$. Inset is a convergent beam electron diffraction pattern from a diffracting particle in the surface layer. The labeled Miller indices correspond to magnetite.

EDS spectra from two spots on the tested cone with $\Lambda \sim 1.1$ are shown in Figure 2.8. Fe, Cr, and Mn were present in the surface layer and subsurface material as expected. Significant oxygen was detected in the surface layer, but not in the subsurface material. Trace levels of Ga and W in the surface layer are believed to be contaminants consistent with the results from untested cone. Low levels of phosphorous (P) and sulfur (S) within the surface layer were attributed to residual test rig and lubricant contamination that possibly became incorporated in the surface layer due to mechanical mixing in the contact.
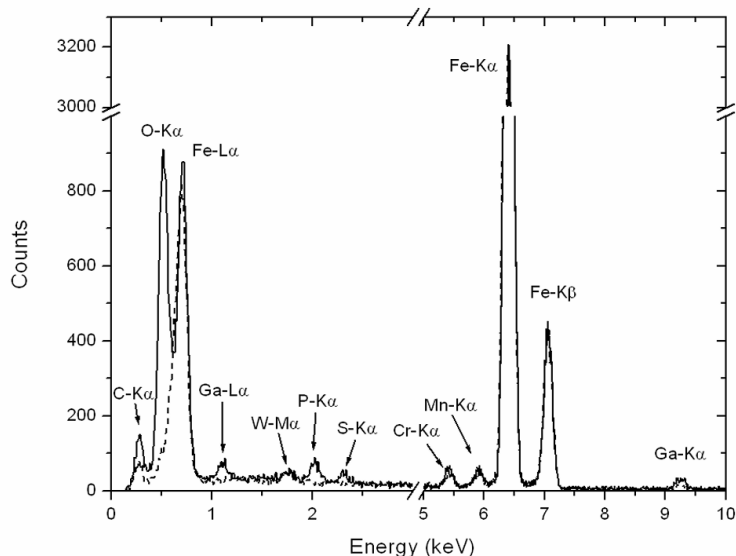
Figure 2.8. EDS spectra from the tested cone with $\Lambda \sim 1.1$. The solid line is from the bright surface layer, while the dashed line is from subsurface bulk material.

2.3.5 TEM of a Cone Tested at $\Lambda \sim 0.3$

Figure 2.9 shows a cross-sectional TEM image from the cone tested at $\Lambda \sim 0.3$. Numerous small surface cracks and portions of a distinct surface layer were observed. No other large cracks were observed in the sample, but the TEM investigation was limited to depths of $\sim 6\mu m$. The subsurface region corresponding to the depth of maximum shear stress ($\sim 119\mu m$) was not investigated for cracks. The uppermost portions of the surface layer delaminated during specimen preparation except for the portions trapped below the tungsten coating that was deposited immediately after testing. The remains of that original tungsten coating are labeled above the intact surface layer on the left side of Figure 2.9. The other bright and dark layers above portions of delaminated oxide film are residual glue and a second tungsten layer from the FIB sample preparation process. Most of the original surface film delaminated during sample

46

preparation. Figure 2.10 shows a high magnification image of an intact portion of the original surface layer (< 100 nm thick) on the cone surface. A sharp interface existed between the surface layer and the base steel. The surface layer appears much brighter in the images with little diffraction contrast that suggests an amorphous structure. The near-surface material below the surface layer appears to have experienced large plastic strains and has a stratified structure at high magnification. Arcs at the ferrite (110) reflections rather than rings or spots in selected-area diffraction patterns (inset in Figure 2.10) suggest a large grain size or textured ferrite polycrystals in close proximity to the surface layer.
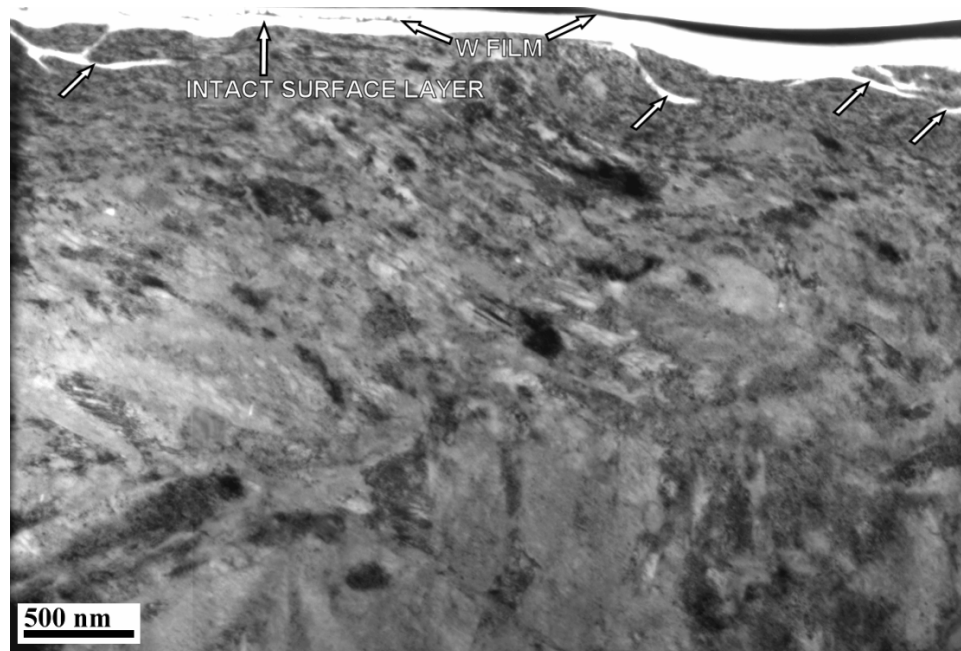
Figure 2.9. Cross-sectional TEM image from a cone tested at $\Lambda \sim 0.3$. The intact original surface layer was preserved under areas of the first protective W film that was deposited immediately after testing. The protective W film toward the top right-hand corner of the image was deposited during FIB processing. Unlabeled arrows denote surface cracks.
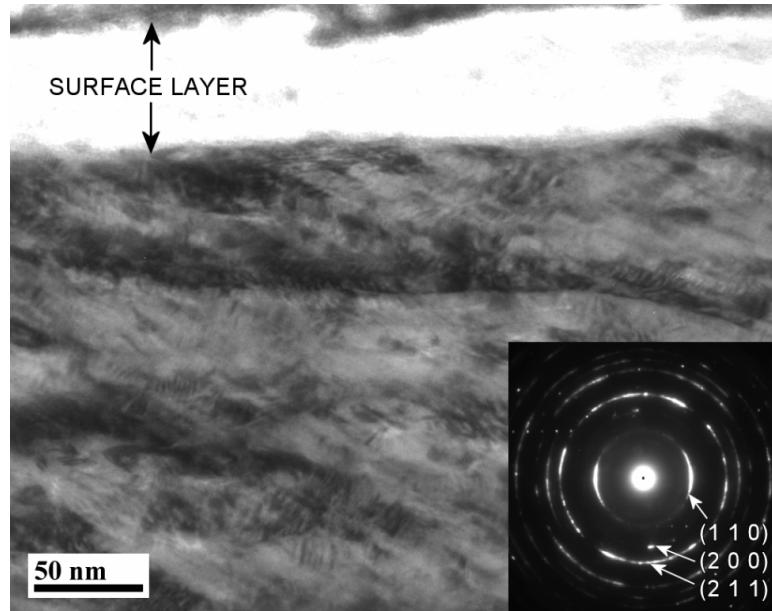
Figure 2.10. Higher magnification cross-sectional TEM image of the intact surface layer on the cone raceway that was tested at $\Lambda \sim 0.3$. Inset is a SAD pattern for the subsurface textured material (below the surface layer) with ferrite Miller indices labeled.

Convergent-beam electron diffraction (CBED) and EDS analyses were conducted within one of the cracks from Figure 2.9. Figure 2.11 shows the region of interest with inset convergent-beam diffraction patterns and annotations (A-F) indicating the spots corresponding to EDS spectra in Figures 2.12-2.14. Analysis of CBED patterns indicated that the surface layer was mostly amorphous (as shown in Figure 2.11) with a modicum of small crystalline regions. The *d*-spacings measured from the CBED patterns from several surface layer crystallites were consistent with α-Fe_2O_3, but the possibility of Fe_3O_4, and $Fe_{1-x}O$ could not be excluded due to overlap of reflections. No direct evidence of ferrite was found in the oxide-rich surface layer via electron diffraction. However, ferrite was detected in the subsurface material (Miller indices in Figure 2.11), consistent with the other samples analyzed in this study. EDS spectra collected from the subsurface material at spots A and B (Figure 2.12) indicated Fe, Mn and Cr as expected

for the steel and consistent with the new cone spectra in Figure 2.5. No oxygen was detected in the bulk material close to the crack at spot B. The low levels of Ga and W are believed to be contaminants from the sample preparation process (as previously discussed). The carbon signal in Figures 2.12-2.14 could be attributed to residual oil or decomposition products that became incorporated in the surface layer during the bearing test. EDS spectra in Figure 2.13 from spots C and D within the crack indicated the presence of Fe, Mn, Cr, and high levels of oxygen and carbon. Ga and W from sample preparation were present in addition to Al and S that likely originated from minor lubricant or test rig contamination. The spectra in Figure 2.14 revealed that the surface layer is mostly oxidized iron containing many low-level impurities such as Al, P, S, Ca, Cu, and Zn.
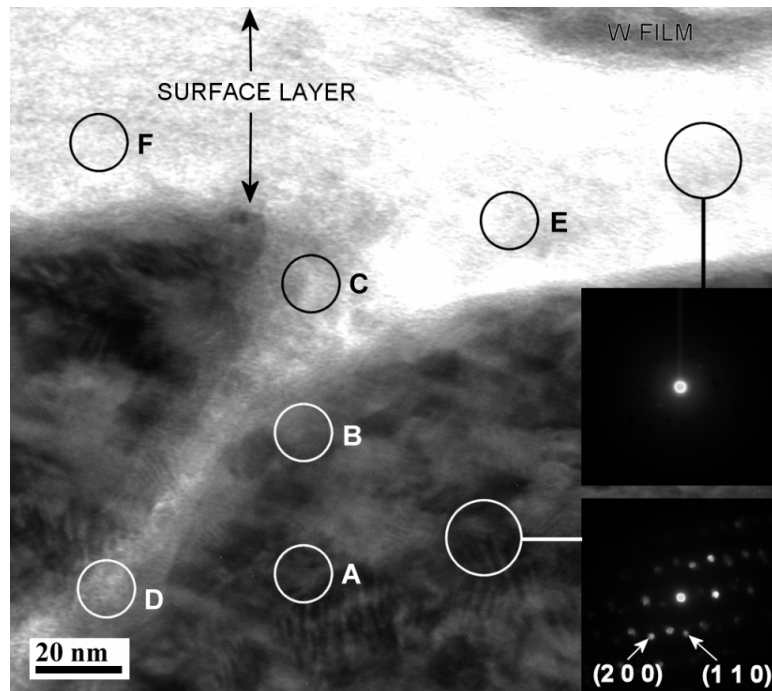
Figure 2.11. High magnification cross-sectional TEM image of a surface crack from the tested cone with $\Lambda \sim 0.3$. Intact original surface layer was preserved under W film. The inset CBED patterns were collected from the indicated spots, and ferrite Miller indices are labeled for the subsurface pattern. The annotations (A-F) indicate the spots corresponding to the EDS spectra shown in Figures 2.12-2.14.

49
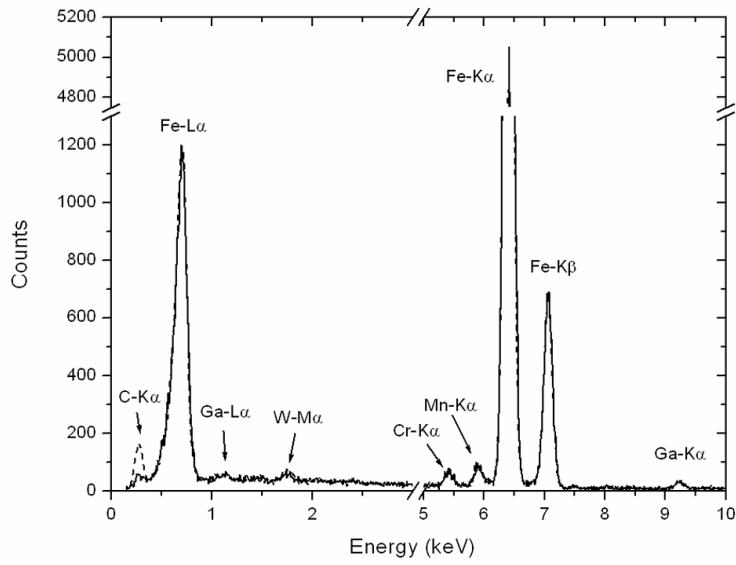
Figure 2.12. EDS spectra for spots A (solid) and B (dashed) from near-surface regions labeled in Figure 2.11.
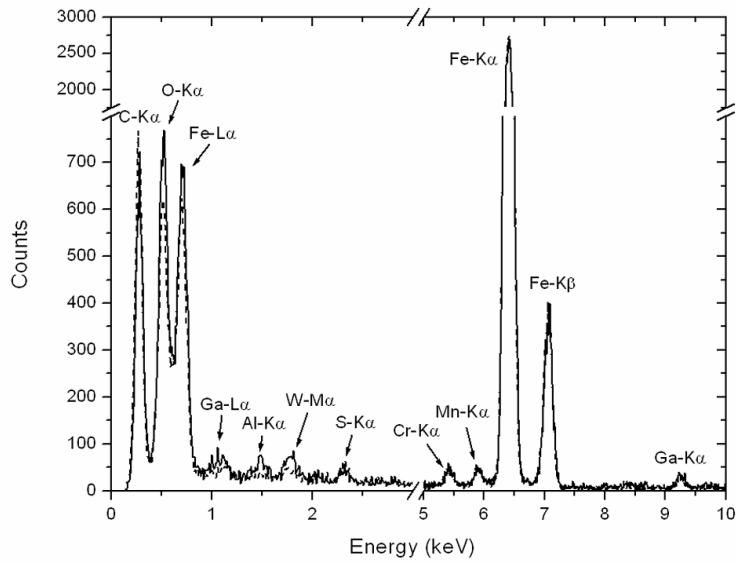
Figure 2.13. EDS spectra for spots C (solid) and D (dashed) within the crack as labeled in Figure 2.11.
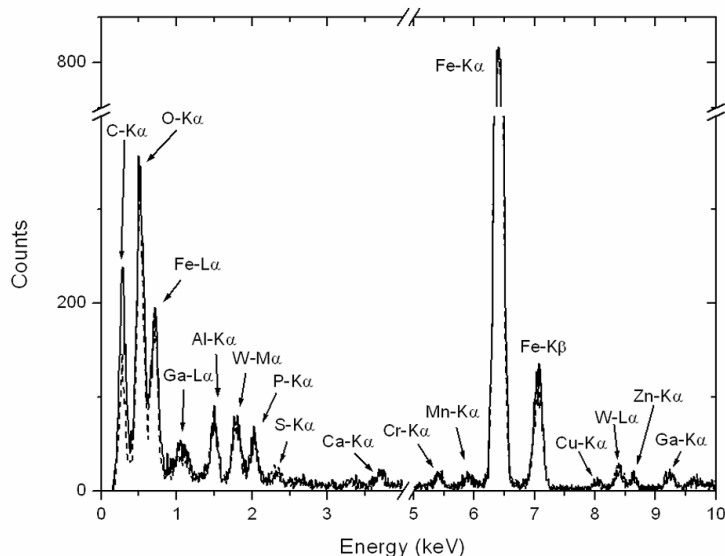
Figure 2.14. EDS spectra for spots E (solid) and F (dashed) within the intact surface layer as labeled in Figure 2.11.

2.4   DISCUSSION

The ability to directly image near-surface material from steel tapered roller bearing cones using TEM reveals a wealth of information about the effects of finish grinding, lubrication regime, and chemical reactions on bearing surfaces. The observed near-surface grain size gradient and microstructural distortion in the untested cone are believed to be consequences of large deformation strains during the grinding surface finishing operation. Following Rigney's analysis of sliding contacts [36], it is suggested that the characteristics of the deformation substructures produced during grinding were dependent on strain gradients imparted to the surface. The fine grains that were found in the near-surface material were consistent with high strain levels, while the relatively larger grains (which may be describable as dislocation cells or subgrains) > 500 nm below the surface would be expected for lower strains. Optical microscopy of Nital-etched cone surface

specimens at magnifications much lower than the TEM analyses (only up to 1000x) revealed deformation-induced transformation of the austenite close to the surface and a directional orientation of the near-surface grains. This mechanical effect is generally associated with a sharp residual stress peak at the surface (< 25 μm) of properly ground components. For example, Voskamp et al. [7] reported initially high residual compressive stresses in mechanically ground SAE 52100 ball bearing surfaces.

Electron diffraction patterns from the near-surface fine-grained material in the untested cone were consistent with ferrite and possibly martensite. Other researchers also identified ferrite in subsurface steel via electron diffraction after rolling contact [5,6,7,32]; however, none of the previous work identified the phases within the near-surface material (depth < 500 nm). The subsurface microstructure in the tested cones > 500 nm from the surface did not appear to deviate significantly from that of the untested cone. Well-known mechanically induced microstructural changes (e.g., white etching bands) in subsurface material are most prominent at depths exceeding 100 μm [4], and were not considered in the present study. Electron diffraction patterns suggested the presence of textured polycrystals in the near-surface material from the $\Lambda \sim 0.3$ cone. Texture development in surface material due to surface deformation and tribological contact has been identified elsewhere using x-ray diffraction. Voskamp [37] found subsurface texture development (at depths > 100 μm) due to rolling in steel ball bearings. Wheeler and Buckley [38] reported the development of a (110) texture in sliding experiments with ferrite.

The severity of local boundary lubrication (Λ) affected the development and structure of the oxygen-rich surface layer in the tested cones. Such chemically changed surface

layers have been termed "boundary films" [1]. The $\Lambda \sim 1.1$ cone had a partially crystalline surface layer that appeared to contain a mixture of magnetite (Fe_3O_4) and ferrite after testing. A native Fe_3O_4 layer (~ 3 nm thick) forms on all iron surfaces in air, but thicker Fe_3O_4 film formation in air typically requires temperatures exceeding 300ºC [21]. The bulk oil temperature in the $\Lambda \sim 1.1$ test was 60ºC, therefore the formation of a $\sim$50-150 nm thick surface layer containing Fe_3O_4 is attributed to high localized asperity contact temperatures and pressures. Bellon and Averback [39] have described systems in which repeated forcing/relaxation events bring about unconventional kinetic pathways and/or non-equilibrium material changes as "driven." FTIR and water content analyses indicated that the lubricant did not contain an abundance of oxidized species or water. Atmospheric oxygen likely reached the cone surface after first dissolving into the mineral oil [15]. Since the expected solubility of oxygen in mineral oil is low, the oxide layer growth rate was presumably oxygen limited. Thus, the formation of a coherent, fine-grained, polycrystalline surface layer containing Fe_3O_4 and ferrite is attributed to low oxygen ion fluxes in contact with near-surface material during testing. This hypothesis is consistent with the Fe-O equilibrium phase diagram, which predicts a stable Fe_3O_4-ferrite mixture for oxygen concentrations less than $\sim$57 at.% and temperatures less than 570°C [40].

The presence of Fe_3O_4 layers on steel surfaces after tribological contact has been observed in other studies. For example, Montgomery [41] used x-ray diffraction to identify Fe_3O_4 in a surface "glaze" that was scraped from gray cast iron internal combustion engine cylinder bores. In mineral oil boundary lubrication experiments, Kang and Ludema [16] found that $\sim$40 nm thick Fe_3O_4 films formed on steel cylinder-on-

flat couples using Auger electron spectroscopy. Rainforth et al. [22] found nanocrystalline Fe_3O_4 particles in worn surface material from a variety of steel sliding test specimens via TEM. No previous work presented images of iron oxide surface layers formed on commercially available bearings after operation under boundary-lubricated conditions.

In contrast to the $\Lambda \sim 1.1$ cone, the $\Lambda \sim 0.3$ cone had a mostly amorphous surface layer containing a non-equilibrium mixture of α-Fe_2O_3 and possibly Fe_3O_4 and $Fe_{1-x}O$ without any detectable ferrite. The cone raceway had a brown appearance after the bearing test and the surface layer was brittle, consistent with the presence of α-Fe_2O_3 on the surface [21]. The sharp interface between the highly oxidized surface layer and the deformed near-surface material (Figures 2.12, 2.14) may indicate that the surface layer repeatedly formed and was removed during bearing operation. An important distinction between the $\Lambda \sim 1.1$ and 0.3 tests was the degree of oil oxidation as measured by FTIR spectroscopy. The solubility of dissolved oxygen is expected to drop with increasing oil temperature (i.e., via Henry's Law), so the oxygen sources for reaction at the bearing surfaces are probably oxidized oil species. Bowman and Stachowiak [42] reported that oxidized paraffinic mineral oils offer mild scuffing protection for steel by the adsorption of carboxylic acid species on the contacting surfaces. However, they warned that oils with high carboxylic acid concentrations might be corrosive. It is suggested that oxidized oil species may have preferentially adsorbed on the contacting surfaces serving as an oxygen source for near-surface oxidation reactions. Severe asperity-to-asperity contact and readily available oxygen-containing species appeared to accelerate oxide formation reaction kinetics resulting in a non-equilibrium, highly oxidized surface layer. Other

researchers have found that α-Fe_2O_3 preferentially forms in an oxygen-rich environment while Fe_3O_4 forms under oxygen-starved conditions. Saito et al. [20] compared the chemical states of oxide films formed on steel surfaces under various types of aqueous lubrication with an electron probe microanalyzer. They found that the oxide type was dependent on the sliding conditions, including temperature and PV (P = normal applied load, V = sliding speed) mechanical work. Fe_3O_4 and $Fe_{1-x}O$ were the dominant species at high PV values in distilled water, while in a hydrogen peroxide solution (strong oxidizer) α-Fe_2O_3 was prominent even at high PV values.

The events that led to cracking in the near-surface layer for the $\Lambda \sim 0.3$ cone are unclear (Figure 2.11). Crack initiation may have resulted from oxidative attack of surface weaknesses, mechanical straining of near-surface material, or a combination of both mechanisms. The $\Lambda \sim 0.3$ surface layer was highly oxidized as evidenced by the highly amorphous structure and presence of α-Fe_2O_3 crystallites. No conclusive evidence was found in this study that confirmed or rejected the premise that pit and crack initiation was due to oxidation only. Nano-scale cracks propagated at shallow acute angles away from the surface, apparently traveling in parallel with textured and distorted near-surface material (Figure 2.9). Both oxidation and mechanical damage likely contributed to crack formation and propagation. Practically, the surface cracking appeared to be consistent with early stages of "peeling" as defined in conventional bearing failure analysis. Peeling, or micro-spalling, is commonly attributed to asperity-to-asperity contact due to a thin lubricant film [43]. Those criteria were met by the local boundary lubrication conditions of the $\Lambda \sim 0.3$ bearing tests by design. Peeling can lead to premature tapered roller bearing damage by initiating larger cracks and ultimately

resulting in point surface origin spalling [33]. It can also alter geometry, leading to geometrical stress concentration damage and failure. Well-lubricated contacts ($\Lambda \geq 3$) and oxidation-inhibiting lubricant additives may be required to prevent or postpone peeling or near-surface fatigue spalling.

TEM of FIB-prepared samples is an effective method for evaluating the effects of lubricant chemistry on near-surface material. Fundamental information was revealed about how grain size and morphology, microstructural distortion of near-surface material and oxide surface layers change as a function of lubrication conditions. Similar approaches are used in Chapter 3 to study near-surface material from boundary-lubricated bearing surfaces tested with lubricants containing additive formulations.

2.5   CONCLUSIONS

- Focused ion beam milling was used to produce high-quality transmission electron microscopy (TEM) cross-sectional surface samples from steel tapered roller bearing cones that were tested in mineral oil.

- TEM was used to obtain surface layer images, crystallographic information, and chemical compositions from cone near-surface material (depth < 500 nm) with nanometer-scale spatial resolution.

- The near-surface material in an untested steel tapered roller bearing cone was mostly ferrite (with possible martensite), had a grain size gradient as a function of depth, and microstructural distortion in a direction parallel to the cone raceway surface.

- Two types of oxide surface layers (or boundary films) were characterized in cross-section, each one corresponding to a different severity of local boundary lubrication during testing. For the cone tested at $\Lambda \sim 1.1$, a continuous, coherent and partially crystalline surface layer containing Fe_3O_4 and ferrite was observed. For the cone tested at $\Lambda \sim 0.3$, a mostly amorphous oxygen-rich surface layer containing $\alpha\text{-}Fe_2O_3$ crystallites and possibly Fe_3O_4 and $Fe_{1-x}O$ was observed.

- Microcracks were observed in the near-surface material of the cone tested at $\Lambda \sim 0.3$. Energy dispersive spectroscopy analysis revealed a significant amount of oxygen and carbon in the cracks.

2.6   REFERENCES

1. R. S. Fein: Boundary lubrication relations, in *Tribology Data Handbook*, edited by E. R. Booser. (CRC Press, New York, 1997).

2. K. Kato: Wear in boundary or mixed lubrication regimes, in *Boundary and Mixed Lubrication: Science and Applications*, edited by D. Dowson, G. Dalmaz, and A. Lubrecht. (Elsevier Science, Amsterdam, 2002).

3. B. H. Pruitt: *Timken: From Missouri to Mars - A century of leadership in manufacturing.* (Harvard Business School Press, Boston, 1998).

4. J. J. Bush, W. L. Grube, and G. H. Robinson: Microstructural and residual stress changes in hardened steel due to rolling contact. *ASM Trans.* **54**, 390 (1961).

5. J. A. Martin, S. F. Borgese, and A. D. Eberhardt: Microstructural alterations of rolling bearing steel undergoing cyclic stressing. *J. Basic Eng.* **88**, 555 (1966).

6. H. Swahn, P. C. Becker, and O. Vingsbo: Martensite decay during rolling contact fatigue in ball bearings. *Metall. Trans. A* **7A,** 1099 (1976).

7. A. P. Voskamp, R. Osterlund, P. C. Becker, and O. Vingsbo: Gradual changes in residual stress and microstructure during contact fatigue in ball bearings. *Met. Technol.* **7**, 14 (1980).

8. V. Bhargava, G. T. Hahn, and C. A. Rubin: Rolling contact deformation and microstructural changes in high strength bearing steel. *Wear* **133**, 65 (1989).

9. C. Longching, C. Qing, and S. Eryu: Study on initiation and propagation angles of subsurface cracks in GCr15 bearing steel under rolling contact. *Wear* **133**, 205 (1989).

10. I. I. Kudish, and K. W. Burris: Modern state of experimentation and modeling in contact fatigue phenomenon: Part I—Contact fatigue. *Tribol. Trans.* **43**, 187 (2000).

11. B. J. Griffiths: Mechanisms of white layer generation with reference to machining and deformation processes. *J. Tribol.* **109**, 525 (1987).

12. Y. Wang, C. Q. Gao, T. C. Lei, and H. X. Lu: Amorphous structure of worn surface in 52100 steel. *Scr. Metall.* **22**, 1251 (1988).

13. E. Sauger, L. Ponsonnet, J. M. Martin, and L. Vincent: Study of the tribologically transformed structure created during fretting tests. *Tribol. Int.* **33**, 743 (2000).

14. J. Schofer, P. Rehbein, U. Stolz, D. Lohe, and K. H. Zum Gahr: Formation of tribochemical films and white layers on self-mated bearing steel surfaces in boundary lubricated sliding contact. *Wear* **248**, 7 (2001).

15. K. C. Ludema: A review of scuffing and running-in of lubricated surfaces, with asperities and oxides in perspective. *Wear* **100**, 315 (1984).

16. S. C. Kang and K. C. Ludema: The 'breaking-in' of lubricated surfaces. *Wear* **108**, 375 (1986).

17. Y. W. Zhao, J. J. Liu, and L. Q. Zheng: The oxide film and oxide coating on steels under boundary lubrication, in *Proc. of 16th Leeds Lyon Symposium on Tribology.* (Elsevier, New York, 1990).

18. E. C. Cutiongco and Y. W. Chung: Prediction of scuffing failure based on competitive kinetics of oxide formation and removal: Application to lubricated sliding of AISI 52100 steel on steel. *Tribol. Trans.* **37**, 622 (1994).

19. H. Kong, E. S. Yoon, and O. K. Kwon: Self-formation of protective oxide films at dry sliding mild steel surfaces under a medium vacuum. *Wear* **181-183**, 325 (1995).

20. T. Saito, Y. Imada, K. Sugita, and F. Honda: Tribological study of chemical states of protective oxide film formed on steel after sliding in humid atmosphere and in aqueous solutions. *J. Tribol.* **119**, 613 (1997).

21. D. Godfrey: Iron oxides and rust (hydrated iron oxides) in tribology. *Lub. Eng.* **55**, 33 (1999).

22. W. M. Rainforth, A. J. Leonard, C. Perrin, A. Bedolla-Jacuinde, Y. Wang, H. Jones, and Q. Luo: High resolution observations of friction-induced oxide and its interaction with the worn surface. *Tribol. Int.* **35**, 731 (2002).

23. R. S. Fein and K. L. Kreuz: Chemistry of boundary lubrication of steel by hydrocarbons. *ASLE Trans.* **8**, 29 (1965).

24. S. M. Hsu and E. E. Klaus: Some chemical effects in boundary lubrication Part I: Base oil-metal interaction. *ASLE Trans.* **22**, 135 (1977).

25. Y. Wang, T. C. Lei, and C. Q. Gao: An observation of a filiform wear product in bearing steel 52100. *Wear* **134**, 231 (1989).

26. C. Brin, J. P. Riviere, J. P. Eymery, and J. P. Villain: Structural characterization of wear debris produced during friction between two austenitic stainless steel antagonists. *Tribol. Lett.* **11**, 127 (2001).

27. M. H. F. Overwijk, F. C. van den Heuvel, and C. W. T. Bulle-Lieuwma: Novel scheme for the preparation of transmission electron microscopy specimens with a focused ion beam. *J. Vac. Sci. Technol. B* **11**, 2021 (1993).

28. K. S. Murphy, K. L. More, and M. J. Lance: As-deposited mixed zone in thermally grown oxide beneath a thermal barrier coating. *Surf. Coat. Tech.*, **146-147**, 152 (2001).

29. R. Wang, C. Mercer, A. G. Evans, C. V. Cooper, and H. K. Yoon: Delamination and spalling of diamond-like carbon tribological surfaces. *Diam. Relat. Mater.* **11**, 1797 (2002).

30. R. D. Evans, G. L. Doll, P. W. Morrison Jr., J. Bentley, K. L. More, and J. T. Glass: The effects of structure, composition, and chemical bonding on the mechanical properties of Si-aC:H thin films. *Surf. Coat. Tech.* **157**, 197 (2002).

31. K. L. More, D. W. Coffey, B. A. Pint, K. S. Trent, and P. F. Tortorelli: TEM specimen preparation of oxidized Ni-base alloys using the focused ion beam (FIB) technique, in *Proc. of Microscopy and Microanalysis.* (Philadelphia, PA, 2000).

32. A. Muroga and H. Saka: Analysis of rolling contact fatigued microstructure using focused ion beam sputtering and transmission electron microscopy observation. *Scr. Metall. Mater.* **33**, 151 (1995).

33. W. E. Littmann, R. L. Widner, J. O. Wolfe, and J. D. Stover: The role of lubrication in propagation of contact fatigue cracks. *J. Tribol.* **90**, 89 (1968).

34. D. Dowson and G. R. Higginson: *Elasto-hydrodynamic Lubrication.* (Pergamon Press, Oxford, 1977).

35. D. R. Lide, ed.: *CRC Handbook of Chemistry and Physics*, 81st ed. (CRC Press, Boca Raton, 2000).

36. D. A. Rigney: Large strains associated with sliding contact of metals. *Mater. Res. Innovat.* **1**, 231 (1998).

37. A. P. Voskamp: Material response to rolling contact loading. *J. Tribol.* **107**, 359 (1985).

38. D. R. Wheeler and D. H. Buckley: Texturing in metals as a result of sliding. *Wear* **33**, 65 (1975).

39. P. Bellon and R. S. Averback: Preface to viewpoint set on: materials under driving forces. *Scr. Mater.* **49**, 921 (2003).

40. H. A. Wriedt: Iron-Oxygen Binary Phase Diagram, in *ASM Handbook: Alloy Phase Diagrams, vol. 3* (American Society for Metals, Metals Park, OH, 1992).

41. R. S. Montgomery: Run-in and glaze formation on gray cast iron surfaces. *Wear* **14**, 99 (1969).

42. W. F. Bowman and G. W. Stachowiak: The effect of base oil oxidation on scuffing. *Tribol. Lett.* **4**, 59 (1998).

43. R. L. Widner, ed.: Failures of Rolling Element Bearings, in *Metals Handbook: Failure Analysis and Prevention, vol. 11*, 9th ed. (American Society for Metals, Metals Park, OH, 1986).

CHAPTER 3

ANTIWEAR FILMS FROM LUBRICANT ADDITIVES[*]

3.1   INTRODUCTION

Gear oil lubricants containing sulfur- and phosphorus-containing additives are used widely in power transmission equipment, including industrial gear drives and both light and heavy truck transmissions and axles. Steel tapered roller bearings are used in these applications and sometimes experience corrosive wear and micropitting under various conditions. For this reason, a better understanding of the interaction between gear oil additives and rolling element bearing contact surfaces is desired.

Transmission electron microscopy (TEM) studies of near-surface material (depth < 500 nm) from tapered roller bearing cones tested in base mineral oil were the subject of Chapter 2. Cross-sectional TEM imaging and elemental analysis revealed the structure and composition of surface layers that formed on the cones during bearing testing. The characteristics of iron oxide in the layers depended on lubrication conditions. The preparation of intact surface samples was possible using focused ion beam (FIB) milling techniques. In this Chapter, TEM of FIB samples was used to study the structure and composition of surface layers (i.e., "antiwear films" or "boundary films" or "tribofilms") that formed on cones tested in mineral oil with sulfur- and phosphorus-containing gear oil additives (S-P additives).

The literature contains two general approaches for evaluating the benefits of S-P additives in base oils: single chemical studies and formulation studies. Single chemical

---

[*] The primary contents of this chapter have been published in: R. D. Evans, K. L. More, C. V. Darragh, and H. P. Nixon: Transmission electron microscopy of boundary-lubricated bearing surfaces. Part II: Mineral oil lubricant with sulfur- and phosphorus-containing gear oil additives. *Tribol. Trans.* **48**, 299 (2005).

studies are used to develop mechanistic understanding of specific additive actions, but lack practical relevancy since they tend to ignore synergistic effects. Commercial additive formulation studies are useful for equipment design engineering, but they can be scientifically vague if proprietary additive chemical compositions are unknown. Several examples of each approach from the literature are referenced throughout this Chapter, but the present experimental work follows the latter.

Conventional wisdom exists about the function of chemical constituents in gear oil S-P additive formulations, even in the absence of complete knowledge about their chemistry. The phosphorus-containing components in S-P additive formulations are known as antiwear (AW) additives. Phosphate-type antiwear surface layers form in the contacts to minimize damage during asperity-asperity contact. Sulfur-containing components are commonly referred to as extreme pressure (EP) additives. When nascent iron surfaces are exposed after shearing of asperities in severe conditions, sulfur reacts with the surface to form iron sulfides, thus reducing the probability of adhesive wear. The antiwear films that result from S-P additive action are continuously replenished during operation and wear. In addition, synergism between dissolved oxygen in the oil and additives may impart antiwear or antiscuff properties to the contacting surfaces. Further understanding about the structure and composition of S-P additive films as a function of contact severity is necessary for continued progress in the optimization of tribological materials and additive formulations.

S-P additive packages are added to base stock oils to help minimize surface damage due to asperity contact in the boundary and mixed lubrication regimes. Several studies have reported S-P additive performance in real applications such as gears [1,2,3] and

bearings [4,5,6]. The use of zinc dialkyl dithiophosphate (ZDDP) and EP additives increased the scuffing load limit in spur gear tests by Haizuka et al. [1]. Hong et al. [2] found that S-P additives were essential for spur gear surface fatigue durability in tests. They attributed long fatigue lives to the presence of antiwear surface layers. Likewise, Wu [3] observed that the use of commercial S-P additives increased the scuffing resistance of carburized test gears at $\Lambda \sim 0.9$ compared to oil without additives. Wan et al. [4], Torrance et al. [5] and Nixon and Zantopulos [6] reported that the use of commercial S-P additive packages was detrimental to rolling element bearing fatigue life under the conditions tested. Adhesive wear resistance in the gear tests was attributed to antiwear film formation from reactive S-P additives in the sliding contacts. In contrast, it was suspected in the bearing studies that excessive additive reactivity led to surface damage that shortened bearing fatigue life.

S-P additive single chemical and formulation performance studies have been conducted in test rig configurations including four-ball [7,8,9], ball-on-disk [10], and others [11,12,13,14]. Overall, the test rig studies have shown that tribological performance is directly affected by antiwear film formation due to the interaction of additive chemicals with contact surfaces.

The most frequently studied S-P additive chemical has been ZDDP, with many reports in the literature about film-formation mechanisms and antiwear film structure. ZDDP was probably not present in the commercial S-P additive formulation tested in the present study (no Zn was detected in oil or antiwear films). However, demonstrations of advanced surface-layer characterizations on ZDDP antiwear films are relevant to the study of antiwear films in general. Gellman and Spencer [15] comprehensively reviewed

the variety of surface analytical techniques that have been applied to study ZDDP antiwear films. Another complete review of those results is not attempted here, but key reports that demonstrate ZDDP antiwear surface layer characterization are highlighted.

Many ZDDP antiwear surface-layer characterization studies were performed on films deposited by immersion tests or tribometers rather than actual bearings or gears. Yin et al. [16] used x-ray absorption near edge structure (XANES) spectroscopy to reveal the presence of both short-chain and long-chain polyphosphate layers in ZDDP antiwear films. In subsequent work, the same group found that the presence of calcium-containing detergent additives affected polyphosphate chain lengths in ZDDP antiwear films [17]. Warren et al. [18] examined immersion test and reciprocating wear test films with atomic force microscopy and nanoindentation. The films generated by static immersion tests had similar mechanical responses to those formed by lightly loaded wear tests. The light load and static immersion test films had elastic-plastic properties, whereas in highly loaded regions the film had predominately elastic properties. Martin [19] presented schematic models of ZDDP antiwear film formation and structure. Wear debris were analyzed with TEM/energy dispersive spectroscopy (EDS), and nanometer-scale iron sulfide particles were found in an amorphous phosphate-based matrix. Varlot et al. [20] compared antiwear film formation from neutral and basic ZDDP and found subtle differences in the film chemical compositions using XANES. They did not detect iron sulfide precipitates in the wear debris and attributed that fact to non-severe wear test conditions. Martin et al. [21] studied ZDDP antiwear surface layers with Auger electron spectroscopy and proposed a two-layer structure consisting of a long-chain polyphosphate surface layer with a mixed iron and short-chain polyphosphate subsurface layer. They observed a

sharp interface between the antiwear film and the substrate, with no iron sulfide or iron oxide interlayer. Kasrai et al. [22] found using XANES that calcium sulfonate in conjunction with ZDDP prohibited the formation of long-chain polyphosphates and reduced their antiwear effectiveness. Instead, calcium phosphates and short-chain polyphosphates were found. Furthermore, sulfides were detected in the films, but they were presumably dissolved in the phosphate matrix since no iron sulfide "adhesion" interlayer was detected [23]. From these examples it is clear that general insight into antiwear surface layer composition and structure is attainable using tools such as XANES, x-ray photoelectron spectroscopy (XPS), Auger electron spectroscopy, nanoindentation as well as TEM of wear debris.

The models from the literature for ZDDP antiwear surface layer formation are schematic, and the three-dimensional film structure has not been imaged previously. The schematic models are limited to a layer-by-layer understanding of film structure and chemistry because of the limited extent of lateral resolution in depth profiling techniques. Furthermore, crystallographic analysis of antiwear films has only been practiced on debris samples that were detached from the base part. Antiwear film samples have been generated with wear testers on flat, low roughness test substrates to compensate for the probe size limitations of certain surface analysis instruments. TEM analysis of FIB cross-sectional surface-layer specimens in additives tribology has been reported only once to the authors' knowledge. Smith et al. [24] imaged and analyzed the structure of intact diesel engine piston deposits from ZDDP and calcium-based detergents in cross section. The present work is believed to be the first TEM study of S-P additive antiwear films from commercial rolling element bearing surfaces using cross-sectional FIB

samples. Furthermore, the studied antiwear films were generated at two levels of local boundary lubrication severity ($\Lambda \sim 0.3$ and 1.1) to identify differences in film structure attributable to the frequency of asperity-asperity interaction.

3.2   EXPERIMENTAL

A brief review of the tapered rolling element bearing tests follows. Additional details may be found in Chapter 2. The dimensions of the test bearings were: 82.55 mm outer diameter, 41.28 mm bore, and 25.65 mm overall bearing width. The bearing material was case carburized 8119 steel with the nominal composition: 0.19 wt.% C, 0.80 wt.% Mn, 0.40 wt.% Cr, 0.30 wt.% Ni, and 0.12 wt.% Mo. After heat-treating, the raceways were ground and honed. Bearing tests were performed on a four-bearing life test rig with a 10-L oil sump. The bearing test lubricant was SAE 20 paraffinic mineral oil base stock containing commercially available sulfur- and phosphorus-containing gear oil additives. The fully formulated additive package was blended at a 6.5 wt.% use level in the base stock at Timken. The additive formulation being evaluated could be used in popular axle lubricants having a GL5 API service level. Commercially, this S-P additive formulation has been required for scuffing protection of hypoid gears in automotive drive axles. Nominal lubricant physical properties are given in Table 3-1. Each four-bearing set was tested continuously for seven days at 1800 rpm with 33.3 kN radial loading (151% of the 1986 catalog load rating). The estimated cone-roller maximum contact pressure was ~2.2 GPa. The bearing test conditions were relevant to application conditions in the field. The dimensionless film thickness parameter Λ, the ratio of lubricant film thickness to initial composite surface roughness, was used to characterize the extent of local boundary

lubrication in the two tests. The lubricant film thickness was controlled by setting the inlet oil temperature at either 60°C or 121°C, corresponding to a calculated $\Lambda \sim 1.1$ and $\Lambda \sim 0.3$, respectively. The lubricant was not drained and refilled between the two tests.

Table 3-1. Physical properties for untested mineral oil with sulfur- and phosphorus-containing gear oil additives (nominal values).

Property	Value
Specific gravity ($H_2O = 1$)	0.90
Viscosity at 40°C	54.35 cSt
Viscosity at 100°C	7.78 cSt
Viscosity index	108
Acid number (mg KOH/g)	0.87

XPS analytical procedures, FIB specimen preparation, and TEM techniques were identical to those discussed in Chapter 2. FIB milling with a 30 kV Ga+ ion beam was used to etch away material at a grazing incidence, producing an electron-transparent window < 100 nm thick. Such site-specific thinning enabled TEM evaluation of intact surface layers on the nanometer scale. In addition, EDS elemental image mapping was performed with an FEI-Philips CM200 field emission gun TEM / scanning TEM (STEM) equipped with an EmiSpec digital acquisition system for spectrum imaging (high resolution EDS maps). The EDS detector on the CM200 was an Oxford Pentafet ATW2. Crystal structures and d-spacings for compounds from a powder x-ray diffraction database were used to index electron diffraction patterns.

3.3   RESULTS

3.3.1   Lubricant Evaluation

Lubricant analyses were performed on three samples: unused mineral oil with S-P additives and mineral oil with S-P additives from the 60°C ($\Lambda \sim 1.1$) and 121°C ($\Lambda \sim 0.3$) bearing tests.   The water content was lower than 0.1 wt.% for every sample.   The lubricant viscosity, as measured at 40°C and 100°C, increased slightly with each increase in test temperature.   X-ray fluorescence spectroscopy revealed a depletion of sulfur and phosphorus in the lubricant as a result of increasing bearing test temperature as shown in Figure 3.1.   Titration measurements indicated that the lubricant total acid number (TAN) decreased as the bearing test temperature increased.   The oil TAN was 0.87 mg KOH/g before testing, 0.84 mg KOH/g after the 60°C bearing test and 0.78 mg KOH/g after the 121°C bearing test.   There were no detectable differences in lubricant oxidation between the unused oil and the 60°C bearing test oil using Fourier transform infrared spectrometry (FTIR), similar to the mineral oil case from Chapter 2.   The oil from the $\Lambda \sim 0.3$ bearing test (121°C) contained oxidized species as evidenced by an extension of the infrared spectrum peaks around 1715 cm^{-1} that suggests the presence of carbonyls (e.g., ketones, aldehydes, and carboxylic acids) [25].
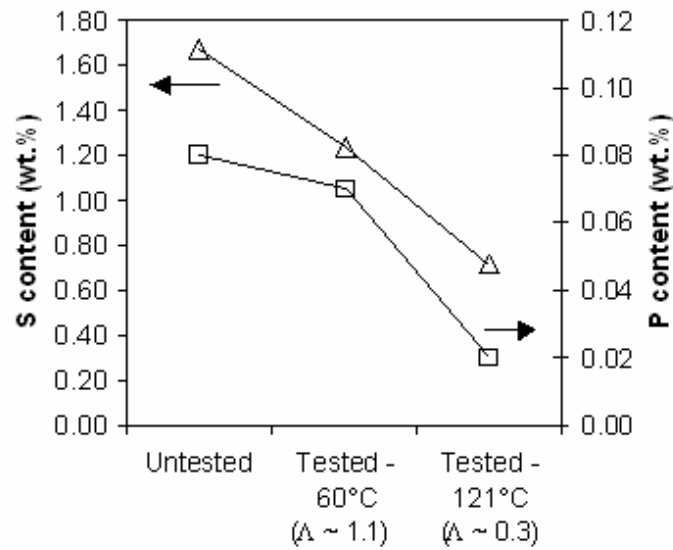
Figure 3.1. Sulfur (Δ) and phosphorus (□) content in the lubricant samples as measured by x-ray fluorescence spectroscopy.

3.3.2   Cone Surfaces

Surface profilometry measurements were collected to survey the root-mean-square roughness (R_q) of cone and roller surfaces before and after testing. A few measurements on representative parts suggested that the cone, roller, and cup load zone R_q values decreased slightly as a result of testing (change of ~0.01-0.03 μm). The cone raceways exhibited normal wear, showing no apparent discoloration after testing. No macroscopic evidence of cone raceway surface damage by micropitting, abrasive wear, or adhesive wear was detected by visual inspection after testing.

XPS chemical depth profiles verified the presence of the tungsten (W) thin film coating that was deposited on the Λ ~ 0.3 and 1.1 cone raceways after the bearing tests. The W film protected the surface layers from damage during subsequent handing and sample preparation. Iron (Fe), oxygen (O), phosphorus (P), carbon (C) and very low

levels of sulfur (S) were detected in a surface layer (antiwear film) immediately below the W film. The antiwear surface layer thickness was estimated to be ~30-40 nm thick from XPS depth profiles for both samples. The $\Lambda \sim 0.3$ surface layer contained higher overall levels of P and S than the $\Lambda \sim 1.1$ layer. This is consistent with the lubricant analyses from Figure 3.1, which suggested a net transfer of P and S species from the lubricant to component surfaces with increasing temperature. A summary of the XPS peak positions is shown in Table 3-2. Interpretations of each element's chemical configuration were made based on peak positions [26]. The P2p peak for both samples was generally consistent with phosphate/phosphite configurations. The depth profiles revealed an O/P at.% ratio of ~3-5, suggesting that the oxygen level was sufficient for phosphate formation with excess available for iron oxide formation. Significant sulfur content was found in the $\Lambda \sim 0.3$ sample only and was generally consistent with a sulfide configuration. The Fe2p peak spanned ~707-711 eV close to the surface, suggesting mixed Fe and Fe$_x$O$_y$, with the 711 eV peak decrease suggesting a higher percentage of Fe metal as subsurface depth increased.

Table 3-2. X-ray photoelectron spectroscopy measured peak positions and chemical configuration interpretations for antiwear film depth profiles.

Λ	Fe2p	O1s	P2p	S2p	C1s
1.1	707-711 eV	531.0 eV	133.1 eV	-	283.7eV
0.3	707-711 eV	531.6 eV	133.5 eV	162.7 eV	284.4 eV
Possible Chemical Configurations	Fe (707 eV), Fe$_x$O$_y$ (711 eV)	Metal Oxide, Phosphate	Phosphates, Phosphites	Sulfides	Carbon, Hydrocarbon

3.3.3 TEM of a Cone Tested at Λ ~ 1.1

The cone tested at Λ ~ 1.1 had a subsurface grain morphology (depth > 500 nm) that was similar in appearance to the untested cone from Chapter 2. In addition, the TEM image in Figure 3.2 shows that the near-surface material had microstructural distortion in a direction parallel to the cone surface (circumferential direction with respect to cone geometry). The primary difference between the cones tested at Λ ~ 1.1 with and without S-P additives was the nature of the thin surface layer. The TEM image in Figure 3.3 shows a higher magnification view of the surface layer for the Λ ~ 1.1 cone tested with S-P additives. In the TEM micrographs, the surface layer has a bright appearance, suggesting it is more electron transparent due to a lower density and/or large amorphous component. The ~20-50 nm thick surface layer was the antiwear film that was deposited during bearing testing due to additive action. The thickness of the antiwear surface layer was consistent with the estimate from XPS depth profiling. The dark layer on top of the bright surface layer was the W film deposited to protect the surface during specimen preparation. The antiwear surface layer was adherent and continuous across the surface of the sample. The near-surface grains of the cone shown in Figure 3.3 appeared to have a near-equiaxed shape in the cross-sectional orientation studied. Selected area electron diffraction (SAD) patterns indicated that the grains had a crystal structure consistent with ferrite (body-centered cubic iron). The interface between the antiwear surface layer and the near-surface material appeared to be abrupt and non-diffuse. Figure 3.4 shows a higher magnification image of the antiwear surface layer with inset diffraction patterns collected from the antiwear layer. The gray contrast within the antiwear surface layer image was indicative of local crystallinity (diffraction contrast). Irregular contrast

71

throughout the antiwear surface layer suggested a heterogeneous film structure throughout its volume with both amorphous and crystalline regions.
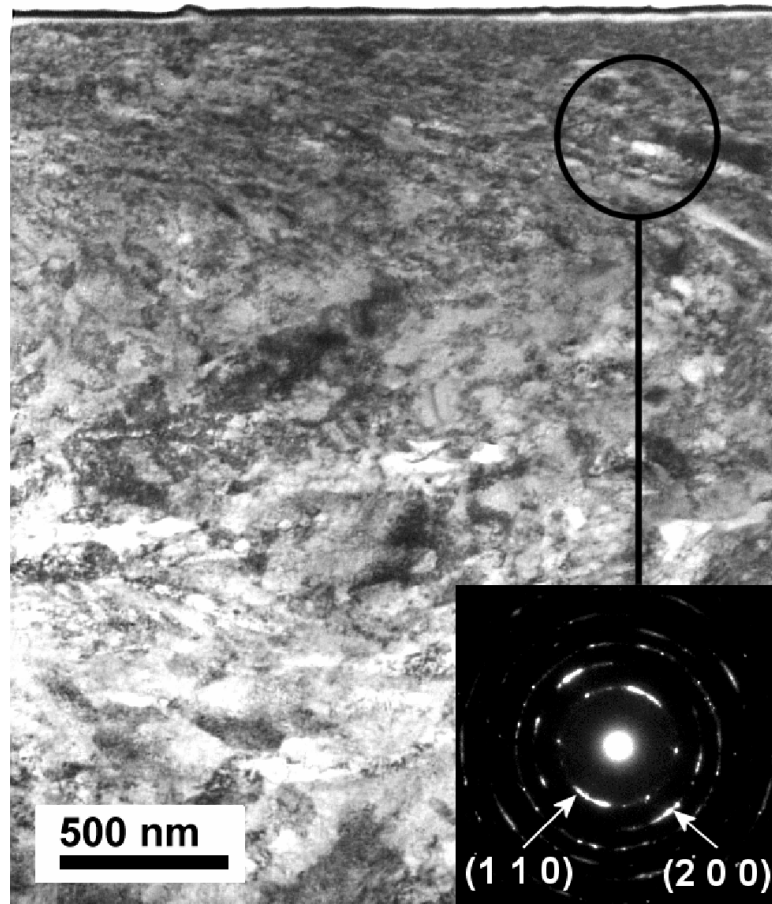
Figure 3.2. Cross-sectional TEM image from a cone tested at $\Lambda \sim 1.1$. The dark surface layer is the protective W film, below which is the antiwear surface layer with a bright appearance. Inset is a SAD pattern consistent with ferrite that was collected from near-surface material.
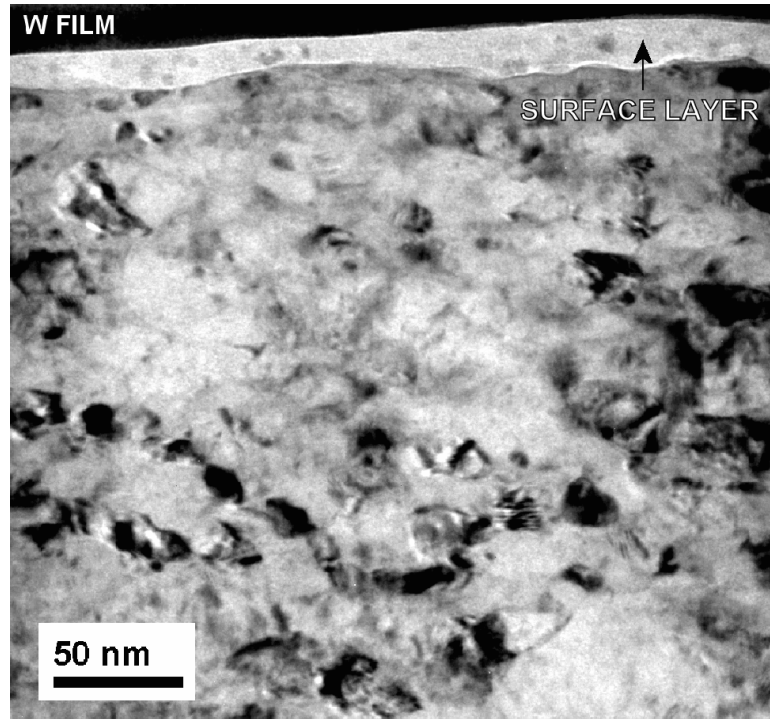
Figure 3.3. Higher magnification cross-sectional TEM image of the near-surface material and surface layer from the cone that was tested at Λ ~ 1.1.

Convergent beam electron diffraction (CBED) patterns collected from very small areas were somewhat difficult to produce under prolonged beam exposure. Crystalline areas became amorphous as evidenced by electron diffraction patterns becoming diffuse if the beam was held on the surface layer for extended durations. The two diffraction patterns shown inset in Figure 3.4 were taken using short beam exposure times (< ~30 s) and show crystalline areas within the surface layer. Similar diffraction patterns from amorphous regions in the surface layer showed diffuse rings rather than spots. The CBED pattern shown in Figure 3.4(c) corresponded to wustite ($Fe_{1-x}O$), which has a face centered cubic lattice with the Fm-3m space group. The predominant hexagonal spot pattern of {220} reflections (d-spacing of 0.15nm) indicated a [$\bar{1}11$] zone axis orientation on a single crystal. Less-discernable spots consistent with {200} reflections for $Fe_{1-x}O$

(d-spacing of 0.21nm) were also labeled on the CBED pattern. The {200} reflections should not be apparent in a single crystal diffraction pattern with a ⟨111⟩ beam direction, so it is likely that the CBED pattern in Figure 3.4(c) contains contributions from multiple $Fe_{1-x}O$ crystals in different orientations. The SAD pattern in Figure 3.4(b) is labeled with measured d-spacings. Although positive identification was not possible, the spacings appeared to be consistent with mixed iron oxides such as $Fe_{1-x}O$, Fe_2O_3 or Fe_3O_4 (Fe_xO_y). Many possible phosphate and sulfide crystals were also considered in the diffraction analyses, but there were no matches for the indexed diffraction patterns. The inability to positively identify crystalline phosphate and sulfide phases does not necessarily exclude their presence in the antiwear surface layers.
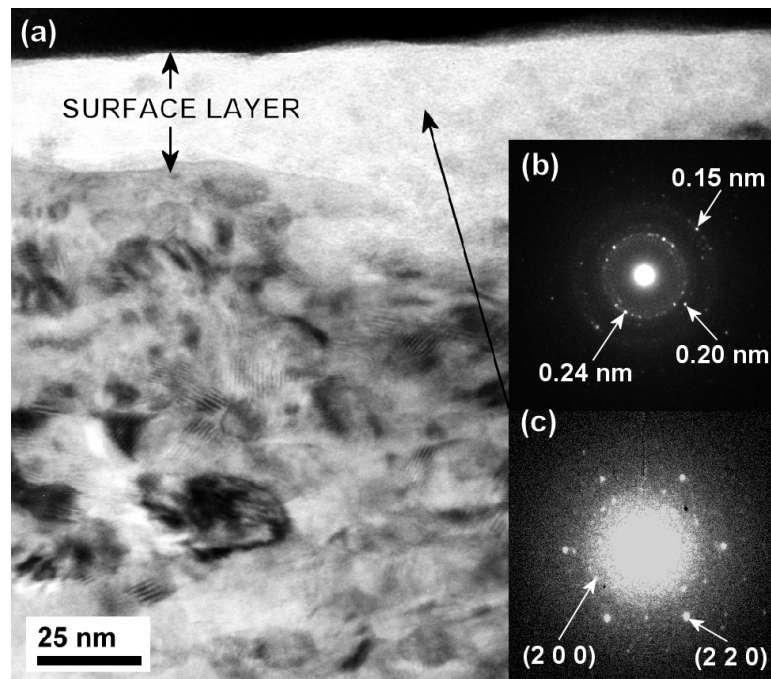
Figure 3.4. (a) High-magnification cross-sectional TEM image of the antiwear surface layer from the cone tested at Λ ~ 1.1. Both electron diffraction patterns are from the antiwear surface layer. The measured d-spacings indicate the likely presence of both (b) mixed iron oxides and (c) wustite ($Fe_{1-x}O$).

EDS spectra from the tested cone with $\Lambda \sim 1.1$ are shown in Figure 3.5. Fe, chromium (Cr), and manganese (Mn) were present in the subsurface material as expected for the steel type. Significant amounts of P, O and Fe were detected in the antiwear surface layer. No P or O was detected in the subsurface material. These results were consistent with the XPS characterization of a primarily phosphate-type antiwear surface layer containing Fe and mixed Fe_xO_y. No significant amounts of S, C, or calcium (Ca) were detected in the surface layer using EDS. W and gallium (Ga) observed in the antiwear surface layer were attributed to some implantation during FIB sample preparation with Ga+ ions and the presence of the W film.
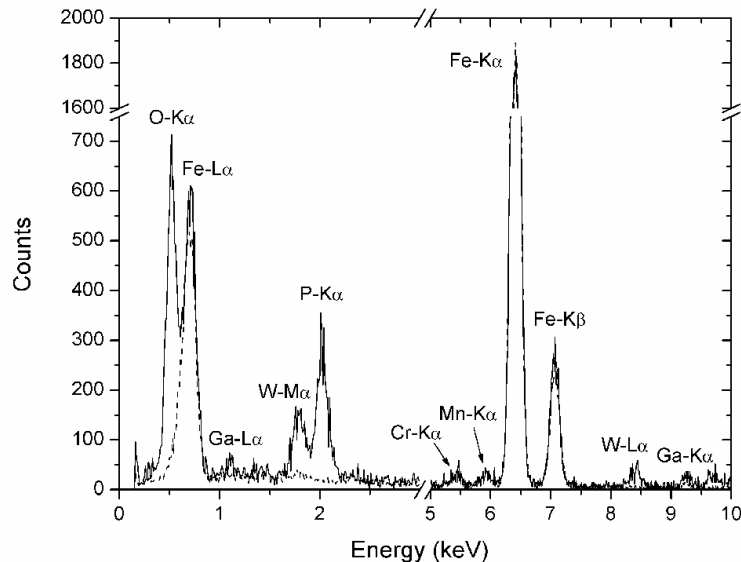
Figure 3.5. EDS spectra from the tested cone with $\Lambda \sim 1.1$. The solid line is from the antiwear surface layer, whereas the dashed line is from subsurface bulk material (normalized with respect to the Fe-K_α peak).

3.3.4 TEM of a Cone Tested at $\Lambda \sim 0.3$

Figure 3.6 shows a cross-sectional TEM image of the near-surface material from the tested cone with $\Lambda \sim 0.3$. A continuous surface layer covered the surface of the sample, similar to that observed on the $\Lambda \sim 1.1$ sample. The antiwear surface layer thickness ranged from ~30 to 100 nm, two times thicker than the layer from the $\Lambda \sim 1.1$ sample in places. Figure 3.7 shows a high magnification TEM image and diffraction patterns from the near-surface region of the cone tested at $\Lambda \sim 0.3$. The surface layer was mostly amorphous in accordance with the cone tested at $\Lambda \sim 1.1$. The CBED diffraction pattern shown in Figure 3.7(b) was from a crystalline region within the antiwear surface layer. Similar to the SAD diffraction pattern shown in Figure 3.4(b), the indexed diffraction pattern was most consistent with mixed iron oxides (Fe_xO_y). The indexed SAD diffraction pattern in Figure 3.7(c) from the near-surface material was consistent with ferrite. The near-surface iron grains appeared to be more stratified and elongated than those from the $\Lambda \sim 1.1$ sample shown in Figure 3.3. A sharp interface consistently separated the antiwear surface layer and base steel. On a nanometer scale, the antiwear surface layer filled in the valleys between steel asperities, thus creating a smoother surface (Figure 3.7).
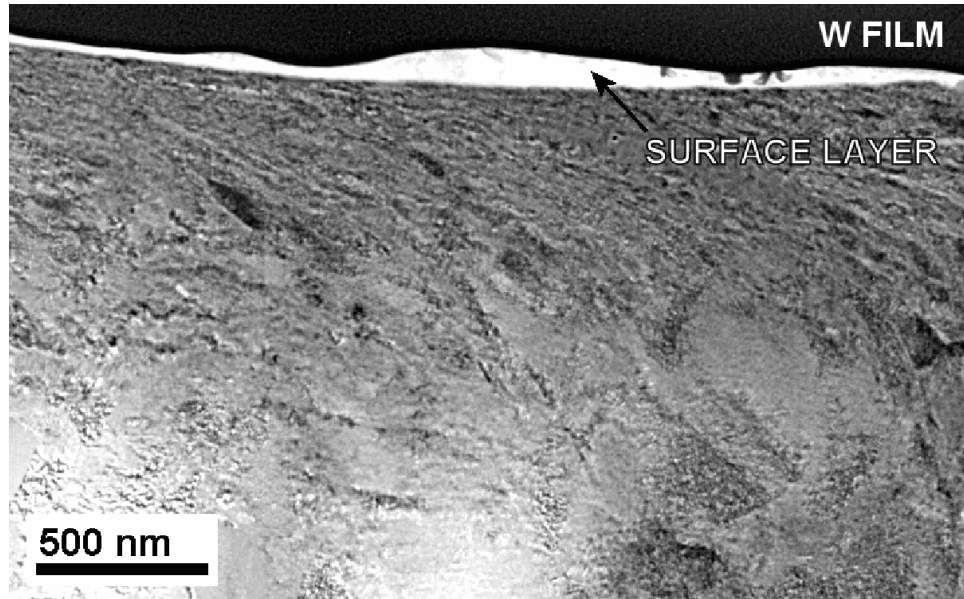
Figure 3.6. Cross-sectional TEM image from a cone tested at $\Lambda \sim 0.3$. The surface layer was coated with a protective W film.
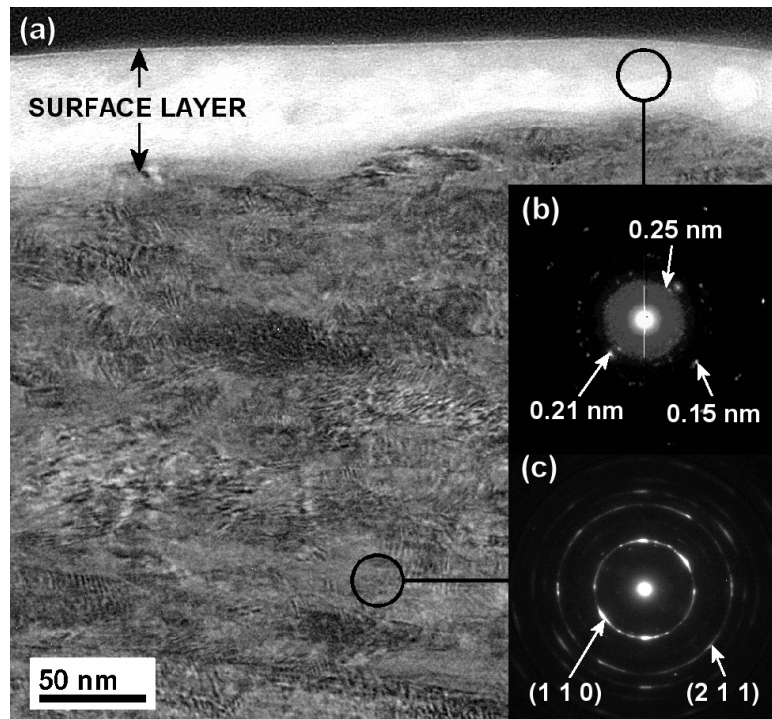
Figure 3.7. (a) High-magnification cross-sectional TEM image of the antiwear surface layer from the cone tested at $\Lambda \sim 0.3$. (b) The surface layer CBED pattern suggests mixed iron oxides. (c) The subsurface SAD pattern is consistent with ferrite.

Localized crystalline regions within the antiwear surface layer were identifiable in part due to dark image contrast. EDS was used to determine compositional differences between crystalline and amorphous regions in the layer. Figure 3.8 shows a high-magnification TEM image from the $\Lambda \sim 0.3$ surface layer with annotations showing the location of EDS measurements. Figure 3.9 shows the spectra corresponding to spots A and B from dark and bright regions in Figure 3.8, respectively. Both spots had high Fe and O levels; however, the dark areas (spot A) had characteristically high P and Ca levels, whereas the bright area (spot B) had high S and C levels. Figure 3.10 shows spectra from the interfacial region between the surface layer and the steel surface (spot C) and the near-surface material ~10 nm below the interface (spot D). The interfacial region contrast appears dark in the TEM image (Figure 3.8), and the EDS spectrum correspondingly indicates high Fe, O and P levels. Low levels of S and C were also present, but Ca was not detected. Even at extremely shallow depths into the near-surface material (~10 nm), the near-surface material had the typical expected composition for the base steel (spot D). No evidence of additive element diffusion into the near-surface material was detected.
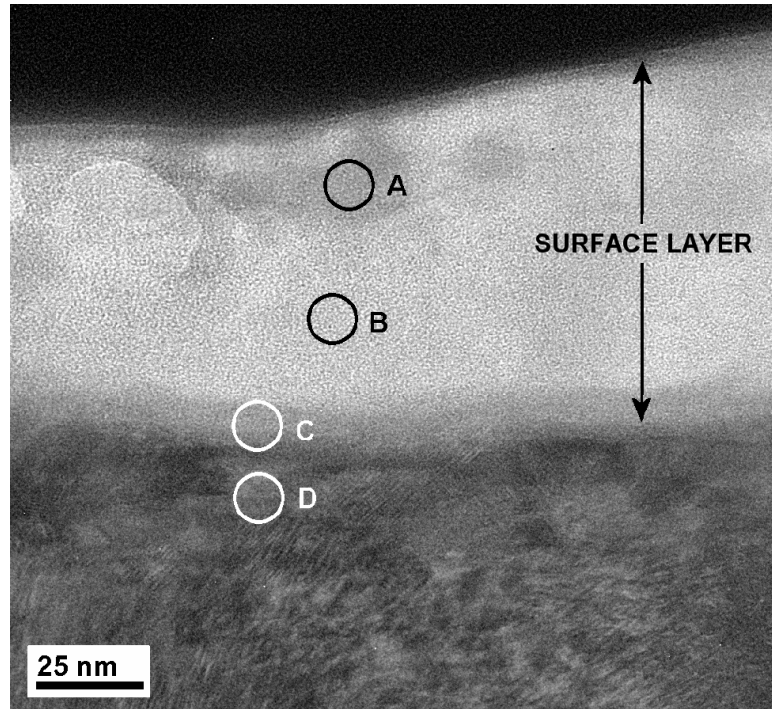
Figure 3.8. High-magnification cross-sectional TEM image of the surface film from a cone tested at $\Lambda \sim 0.3$. The annotations A-D indicate the spots corresponding to the EDS spectra shown in Figures 3.9 and 3.10.
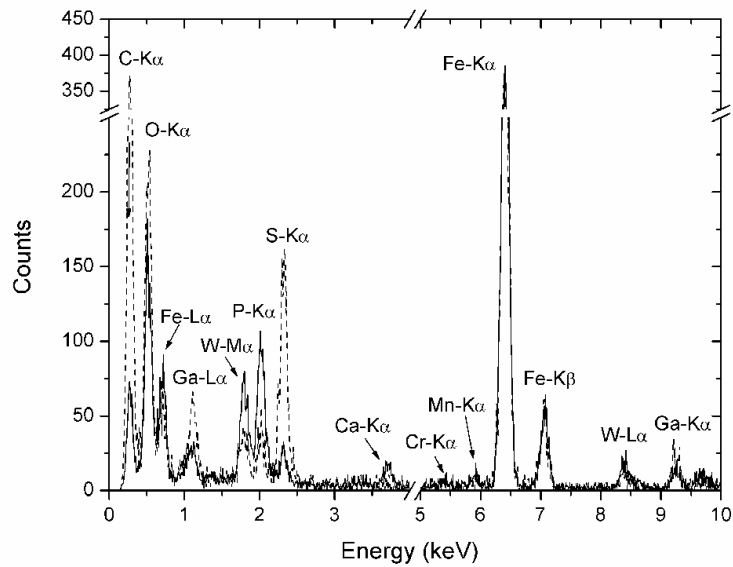
Figure 3.9. EDS spectra for spots A (solid) and B (dashed) within the antiwear surface layer as labeled in Figure 3.8.
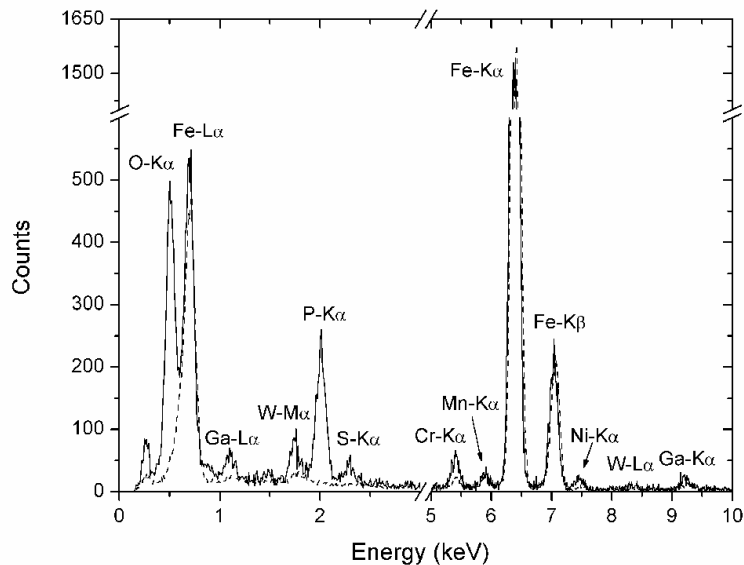
Figure 3.10. EDS spectra for spots C (solid) and D (dashed) within the surface layer/base material interfacial region as labeled in Figure 3.8.

EDS elemental image mapping in a STEM was used to further show the segregation tendencies of S and P in the antiwear surface layer from the cone tested at $\Lambda \sim 0.3$. In contrast with sputter depth profiling (e.g., XPS, Auger electron spectroscopy), this technique was used to identify and map the location of elemental species with nanometer-scale spatial resolution (~1.2nm). Figure 3.11 shows a dark-field STEM image from the $\Lambda \sim 0.3$ antiwear film. In dark-field images, the contrast is reversed as compared to the bright field images that have been presented thus far. The accompanying elemental maps correspond to the analysis area (boxed) shown in the image. Bright intensity in the elemental maps indicates the presence of the element in that analysis spot. The maps clearly show that Fe, P, O and Ca were associated with each other (crystalline regions); however, there were also small regions consisting of mostly Fe or Fe_xO_y. Although low

in total content, the highest S levels were found in amorphous regions close to the interface between the surface layer and base steel.
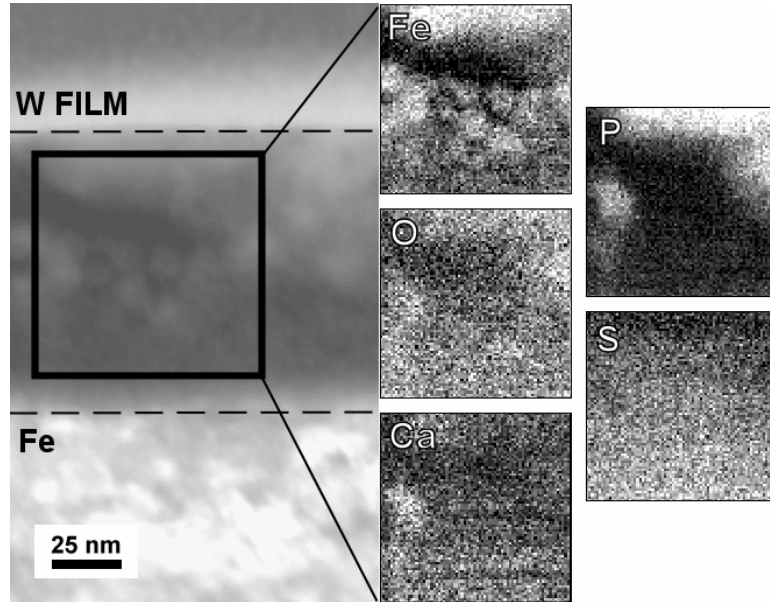
Figure 3.11. Cross-sectional EDS elemental image maps from the antiwear surface layer in a cone tested at $\Lambda \sim 0.3$. Dark-field STEM imaging was used such that less-dense or amorphous regions appear dark whereas crystalline regions appear bright. Brightness in the elemental maps indicates the presence of the labeled element in that analysis spot.

3.4   DISCUSSION

The near-surface material structure for cones tested in base mineral oil (Chapter 2) and mineral oil with S-P additives were similarly affected by the degree of asperity-asperity contact (Λ). The near-surface ferrite grains appeared to have a more equiaxed shape in the cones tested at $\Lambda \sim 1.1$ relative to the grains in the cones tested at $\Lambda \sim 0.3$. This is attributed to increased local boundary lubrication at the $\Lambda \sim 0.3$ condition that imparted higher strain deformation to the near-surface material than the $\Lambda \sim 1.1$ condition. Additional discussions about near-surface material responses to cyclic

loading, as well as the "ratcheting layer" concept, can be found in Chou and Lin [14] or Bower and Johnson [27]. Near-surface material micro-cracks were observed in the cone tested at $\Lambda \sim 0.3$ for the case of no additives (Chapter 2). No cracks were found for the cone tested at $\Lambda \sim 0.3$ with S-P additives under identical lubrication conditions. This suggests that the previously observed cracking was likely due to oxidative attack or some other condition that is remedied by the use of S-P lubricant additives (e.g., high local traction forces).

There were many similarities between the antiwear films from cones tested at $\Lambda \sim 1.1$ and 0.3 with S-P additives. Both films contained Fe, P, and O as iron oxides and phosphates as deduced by XPS and EDS. Both films had a sharp interface (thickness < ~10 nm) between the antiwear surface layer and base steel. The elements in the antiwear film did not appear to diffuse into the near-surface material or attack grain boundaries. The antiwear surface layers did not have a stratified structure with multiple distinct layers. The layers were mostly amorphous with local crystalline regions. The crystalline regions were unstable under prolonged exposure to a focused electron beam in both samples. The crystalline regions appeared to be located somewhat randomly throughout the film volume. The primary difference between the surface layers as a function of Λ was the composition. The antiwear surface layer on the cone tested at $\Lambda \sim 0.3$ appeared to contain higher levels of S, P, Ca, and C than the $\Lambda \sim 1.1$ case. This observation is attributed to a higher degree of local boundary lubrication severity resulting in increased additive action during testing at $\Lambda \sim 0.3$.

The exact antiwear film formation mechanism was not established during this S-P additive formulation study. However, similarities exist between the films observed in

this study and features of popular ZDDP film deposition schematic models. Martin [19] proposed that long-chain zinc polyphosphate films deposit on iron oxide surfaces due to thermal processes in the mild wear regime. As more severe abrasive wear occurs, an antiwear surface layer (tribofilm) containing mixed phosphate glasses begins to accumulate on the surface. The long-chain polyphosphate thermal film continues to deposit on the tribofilm upon a return to mild wear conditions. If the tribofilms are sheared away completely during asperity-asperity contact in local boundary lubrication, nascent surfaces are exposed that react with sulfides in the oil environment to produce metal sulfides. The metal sulfides may be sheared away during subsequent wear, leaving residual sulfides incorporated in the antiwear film. Gellman and Spencer [15] suggested a schematic ZDDP antiwear film structure consisting of a base iron oxide/sulfide layer, a short-chain phosphate interlayer, and a long-chain Zn, Fe polyphosphate glass layer. The observations in the present study from gear oil S-P additive antiwear films complement the general principles of the ZDDP models quite well. At the $\Lambda \sim 1.1$ condition, a mostly iron oxide/phosphate film was observed. Apparently the asperity-asperity contact events were not severe enough on average to result in significant sulfide reaction and incorporation in the regions of the films. At the more severe $\Lambda \sim 0.3$ condition, the iron oxide/phosphate base film was present in addition to significant sulfide, carbon, and calcium levels. Regions with high levels of Fe, O, P, and Ca seemed to be distinct from those with high Fe, O, S, and C levels. Although no discrete layering was observed, the EDS elemental data suggested that the sulfur levels in the $\Lambda \sim 0.3$ films were highest in amorphous regions close to the substrate (Figure 3.11). No crystalline FeS precipitates

were found in the antiwear films, but, following the reasoning of Varlot et al. [20], it is likely that more severe wear conditions would be necessary for their formation.

In the more severe of the two conditions tested, $\Lambda \sim 0.3$, sulfide species were present in the antiwear surface layer. This suggests that contact conditions were conducive to action by the S-containing EP additive component of the formulation, an action that is desirable in gears to prevent adhesive wear. However, the results of this study do not explain how the use of S-P additives reduced rolling element bearing life in previous fatigue tests [4,5,6]. No evidence of corrosive attack, micropitting, or micro-cracking due to grain boundary attack was observed in the samples studied. Wan et al. [4] suggested that oxidized species in the oil with S-P additives could have caused corrosive damage during his tests. Likewise, the oil used in the current $\Lambda \sim 0.3$ tests with and without additives was found to be oxidized (containing carbonyls) using FTIR spectroscopy. However, unlike the case with base mineral oil (Chapter 2), the presence of the antiwear surface layer in these non-fatigue bearing tests was sufficient to prevent damage due to surface attack by oxidized oil species or byproducts. Therefore, it is speculated that previously observed reductions in bearing life may be attributed: 1) to corrosive attack under different tribological conditions or fatigue test durations or, 2) to a phenomenon related to contact mechanics and/or traction in the presence of low friction antiwear additive films. Although it is not possible to generalize the present antiwear surface layer characterization results to every application, a method for obtaining them has been demonstrated along with confirmations and contrasts to existing schematic models for S-P additive film structure.

3.5   CONCLUSIONS

- FIB sample preparation and TEM techniques were used to analyze cross-sectional samples of antiwear films on steel tapered roller bearing cone surfaces tested in mineral oil with sulfur- and phosphorus-containing gear oil additives (S-P additives).

- Continuous and adherent antiwear surface layers (20-100 nm thick) were found on the cone surfaces after bearing testing at $\Lambda \sim 1.1$ and 0.3. A sharp interface < ~10 nm thick separated the antiwear surface layer and base steel. No evidence of S or P diffusion into the steel near-surface material was found.

- Irregular image contrast and electron diffraction indicated that the $\Lambda \sim 1.1$ and 0.3 antiwear surface layers had a heterogeneous structure consisting of local crystalline and amorphous regions.

- The antiwear surface layers from cones tested at $\Lambda \sim 1.1$ and 0.3 both contained Fe, O, and P in iron oxide and phosphate/phosphite configurations as deduced by XPS and EDS.

- Crystalline wustite ($Fe_{1-x}O$) was identified in the antiwear surface layer from the cone tested at $\Lambda \sim 1.1$ using CBED. Measured planar spacings from other crystalline regions within the $\Lambda \sim 1.1$ and 0.3 surface layers were somewhat consistent with various mixed iron oxides.

- In the antiwear surface layers from the cone tested at $\Lambda \sim 0.3$, EDS spectra and elemental image mapping suggested that elements tended to segregate into three types of regions:
  - Fe, O, P, and Ca (crystalline)

- o Fe, O (crystalline)

- o Fe, O, S, and C (amorphous)

- Near-surface ferrite grains from the cones tested at $\Lambda \sim 1.1$ appeared to be more equiaxed in the dimensions studied than those from the cones tested at $\Lambda \sim 0.3$, regardless of the presence of S-P additives in the lubricant.

- Contrary to the results for base mineral oil tests (Chapter 2), no microcracks were observed in the near-surface material of the cone tested at $\Lambda \sim 0.3$ with S-P additives.

3.6 REFERENCES

1. S. Haizuka, R. Nemoto, and C. Naruse: Study on limiting load for scuffing and specific wear of spur gears (effects of lubricating oil and tooth form). *JSME Int. J. – Ser. C* **38**, 149 (1995).

2. H. S. Hong, M. E. Huston, B. M. O'Connor, and N. M. Stadnyk: Evaluation of surface fatigue performance of gear oils. *Lubri. Sci.* **10**, 365 (1998).

3. X. Wu: The effect of S-P gear oil on load capacity of carburized gears, in *Proc. of 4th World Congress on Gearing and Power Transmission.* (Paris, France, MCI, 1999).

4. G. T. Y. Wan, E. V. Amerongen, and H. Lankamp: Effect of extreme-pressure additives on fatigue life of rolling bearings. *J. Phys. D: Appl. Phys.* **25**, A147 (1992).

5. A. A. Torrance, J. E. Morgan, and G. T. Y. Wan: An additive's influence on the pitting and wear of ball bearing steel. *Wear* **192**, 66 (1996).

6. H. P. Nixon and H. Zantopulos: Lubricant additives, friend or foe what the equipment designer needs to know. *Lubr. Eng.* 815 (Oct. 1995).

7. F. G. Rounds: Some effects of additives on rolling contact fatigue. *ASLE Trans.* **10**, 243 (1967).

8. F. G. Rounds: Influence of steel composition on additive performance. *ASLE Trans.* **15**, 54 (1972).

9. Y. Wang, J. E. Fernandez, and D. G. Cuervo: Rolling contact fatigue lives of steel AISI 52100 balls with eight mineral and synthetic lubricants. *Wear* **196**, 110 (1996).

10. K. Komvopoulos, V. Chiaro, B. Pakter, E. S. Yamaguchi, and P. R. Ryason: Antiwear tribofilm formation on steel surfaces lubricated with gear oil containing borate, phosphorus, and sulfur additives. *Tribol. Trans.* **45**, 568 (2002).

11. M. R. Phillips and T. F. J. Quinn: The effect of surface roughness and lubricant film thickness on the contact fatigue life of steel surfaces lubricated with a sulfur-phosphorus type of extreme pressure additive. *Wear* **51**, 11 (1978).

12. S. Shirahama, M. Miyajima, and A. Okamura: Influence of phosphorus additives on rolling fatigue. *Jpn. J. Tribol.* **46**, 193 (2001).

13. S. Shirahama and J. Nakamura: Influence of sulfur-type additives on rolling fatigue. *Jpn. J. Tribol.* **46**, 205 (2001).

14. C. C. Chou and J. F. Lin: A new approach to the effect of EP additive and surface roughness on the pitting fatigue of a line-contact system. *ASME J. Tribol.* **124**, 245 (2002).

15. A. J. Gellman and N. D. Spencer: Surface chemistry in tribology. *Proc. I. Mech. E. Ser. J.* **216**, 443 (2002).

16. Z. Yin, M. Kasrai, M. Fuller, G. M. Bancroft, K. Fyfe, and K. H. Tan: Application of soft x-ray absorption spectroscopy in chemical characterization of antiwear films generated by ZDDP Part I: the effects of physical parameters. *Wear* **202**, 172 (1997).

17. Z. Yin, M. Kasrai, G. M. Bancroft, K. Fyfe, M. L. Colaianni, and K. H. Tan: Application of soft x-ray absorption spectroscopy in chemical characterization of antiwear films generated by ZDDP Part II: the effect of detergents and dispersants. *Wear* **202**, 192 (1997).

18. O. L. Warren, J. F. Graham, P. R. Norton, J. E. Houston, and T. A. Michalske: Nanomechanical properties of films derived from zinc dialkyldithiophoshpate. *Tribol. Lett.* **4**, 189 (1998).

19. J. M. Martin: Antiwear mechanisms of zinc dithiophosphate: a chemical hardness approach. *Tribol. Lett.* **6**, 1 (1999).

20. K. Varlot, M. Kasrai, J. M. Martin, B. Vacher, G. M. Bancroft, E. S. Yamaguchi, and P. R. Ryason: Antiwear film formation of neutral and basic ZDDP: influence of the reaction temperature and of the concentration. *Tribol. Lett.* **8**, 9 (2000).

21. J. M. Martin, C. Grossiord, T. L. Mogne, S. Bec, and A. Tonck: The two-layer structure of Zndtp tribofilms Part I: AES, XPS and XANES analysis. *Tribol. Int.* **34**, 523 (2001).

22. M. Kasrai, M. S. Fuller, G. M. Bancroft, E. S. Yamaguchi, and P. R. Ryason: X-ray absorption study of the effect of calcium sulfonate on antiwear film formation generated from neutral and basic ZDDPs: Part 1 – phosphorus species. *Tribol. Trans.* **46**, 534 (2003).

23. M. Kasrai, M. S. Fuller, G. M. Bancroft, E. S. Yamaguchi, and P. R. Ryason: X-ray absorption study of the effect of calcium sulfonate on antiwear film formation generated from neutral and basic ZDDPs: Part 2 – sulfur species. *Tribol. Trans.* **46**, 543 (2003).

24. G. C. Smith, A. B. Hopwood, and K. J. Titchener: Microcharacterization of heavy-duty diesel engine piston deposits. *Surf. Interf. Anal.* **33**, 259 (2002).

25. D. R. Lide, ed.: *CRC Handbook of Chemistry and Physics*, 81st ed. (CRC Press, Boca Raton, FL, 2000).

26. NIST X-ray Photoelectron Spectroscopy Database, NIST Standard Reference Database 20, Version 3.4 (Web Version), 2003.

27. A. F. Bower and K. L. Johnson: The influence of strain hardening on cumulative plastic deformation in rolling and sliding line contact. *J. Mech. Phys. Solids* **37**, 471 (1989).

CHAPTER 4

TaC/a-C:H COMPOSITION AND STRUCTURE[*]

4.1 INTRODUCTION

Nanocomposite metal carbide/amorphous hydrocarbon (MC/a-C:H) thin films deposited by reactive sputtering of metal or metal carbide targets are being used increasingly as tribological coatings on precision steel components [1,2,3]. This class of materials emerged in the 1980's [4,5,6,7,8,9] as a coating that imparted low friction and high wear resistance to surfaces. X-ray diffraction and x-ray photoelectron spectroscopy were originally utilized to infer the nanocomposite structure of these materials [9,10,11,12,13]. Transmission electron microscopy further confirmed the nanocomposite structure in the 1990's [14,15,16,17,18]. The nanocomposite film structure offers the surface free energy and elasticity of a polymer (a-C:H matrix) with the hardness and wear resistance of a carbide ceramic (MC nano-crystals). This combination of properties makes MC/a-C:H films a key surface engineering option.

Many MC/a-C:H composition and structure studies referenced throughout this manuscript have emphasized the impact of hydrocarbon gas flow rate and applied bias voltage deposition parameters on film properties. However, the studies relied mostly on observations from one-factor-at-a-time experiments. Only one other published study to the author's knowledge utilized statistical multi-factor designed experiments to study this material system. Villiger et al. [19] studied the effects of the C_2H_2 flow rate (via an optical emission monitor setting), applied bias voltage, Ar flow rate, and N_2 flow rate on

the properties of the TiC/a-C:H system using fractional factorial designed experiments. Although useful for some applications, a broad utility of the results was somewhat limited by the narrow applied bias voltage range of -20 to -60 V.

TaC is a Group V interstitial carbide with exceptionally high thermal stability and hardness. TaC/a-C:H films were among the first to be demonstrated for use in tribological applications [4,5,9,10,12,20,21]. These works highlighted the low friction coefficient, high wear resistance, and high hardness that are achievable with TaC/a-C:H films. This Chapter demonstrates a statistical design of experiments approach to evaluate composition and structure trends in TaC/a-C:H films as a function of acetylene flow rate (Q_{C2H2}), applied d.c. bias voltage (V_b), and substrate rotation rate (ω_{Rot}). These process parameters were chosen because they have a direct influence on film properties and are key controls in commercial deposition systems. The statistical design of experiments made possible the identification of first order film structure and composition dependencies on these factors, as well as interaction effects between the factors. An empirical understanding of process-property relationships led to an interpretation of the results using hypothesized film growth mechanisms.

4.2   EXPERIMENTAL

4.2.1   Film Deposition

4.2.1.1   System Design

Depositions were performed in a custom-built, closed-field unbalanced magnetron sputtering system with a base pressure less than 6 x 10^{-3} Pa. The chamber had a cubic geometry with magnetron cathodes positioned in the center of the four sidewalls. Ta-

metal targets were installed in opposing cathode positions as shown in the top view schematic (Figure 4.1). Three permanent magnets were positioned behind each of the four cathode positions with alternating polarity to produce a closed-field configuration [22,23]. Electromagnetic field coils were positioned behind the cathodes to produce unbalanced magnetic fields in front of the targets, thus giving a closed-field unbalanced magnetron sputtering process. Shutters covered the two unused cathodes. A substrate carousel in the center of the chamber was used to rotate the substrates in front of the magnetrons. Si wafer substrates ($\langle 001 \rangle$) were mounted parallel to and about 24 cm from the target faces. Direct current (d.c.) power supplies powered the cathodes and substrate carousel. A constant 30 sccm argon flow rate was used during depositions with various acetylene (C_2H_2) flow rates according to the experimental design. The gases were introduced into the chamber through "showerhead" frames around each of the four target positions. This ensured a uniform, blended Ar/C_2H_2 feed gas. A diffusion pump was used to maintain processing pressures of 0.1–0.3 Pa. The substrates were not intentionally heated, and the maximum substrate temperature during depositions was ~130-150°C as measured with surface contact thermometers mounted to the substrate bracket. The calculated mean free path for Ar atoms in the chamber was 2-6 cm, assuming a neutral Ar gas environment, temperature ~25°C, and pressure 0.1-0.3 Pa. The mean free path for hyperthermal species such as electrons or ions would be higher than the above estimate due to a reduction in collision cross section at higher kinetic energies. The process sequences, power supply, gas flow, and substrate carousel motion were controlled by Allen Bradley PLC modules to help ensure processing accuracy and repeatability.
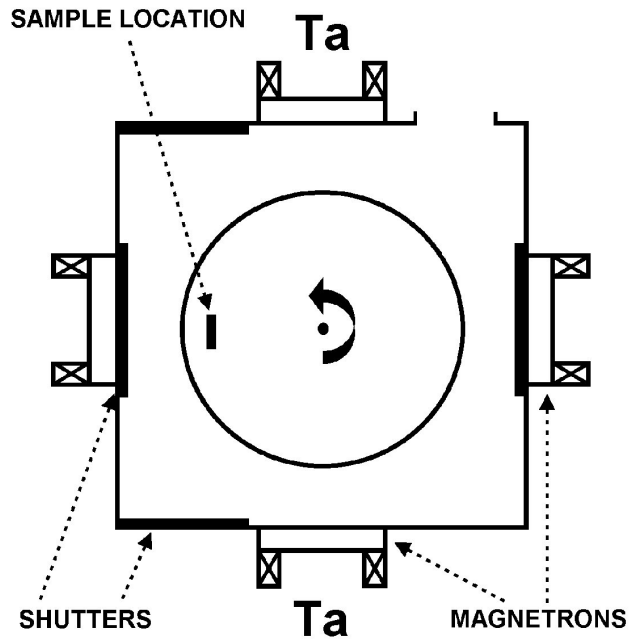
Figure 4.1. Top-view schematic of the magnetron sputtering chamber configuration.

4.2.1.2   Film Architecture

A multi-step procedure was used for film deposition. The substrates were first treated by Ar ion bombardment with an applied d.c. bias of -500 V for 20 min to remove adsorbed contaminants so each experiment began with a reproducible surface. A thin layer of Ta metal was then sputtered onto the substrates for 20 minutes to enhance film adhesion. The Ta deposition rate increased almost linearly with increasing Ta-target d.c. power level. A 3.1 W/cm^2 target power density resulted in a 1.5 μm/hr sputter rate of Ta in Ar plasma. After Ta interlayer deposition, the flow rate of C_2H_2 gas was ramped from zero to the desired level in 15 minutes at a constant Ar flow rate producing a compositional gradient layer.

The TaC/a-C:H top layer was deposited by reactive d.c. magnetron sputtering of Ta targets in the Ar/C_2H_2 plasma at a constant target power density level of 3.1 W/cm^2. The top layer deposition duration was 60 min for each experiment. The addition of C_2H_2 to the sputtering environment affected the Ta target surface condition via adsorption of carbon species on the target. As the C_2H_2 flow rate increased, the target voltage increased (and therefore the current decreased) at a constant power level. The sputter yield of Ta-metal decreased with increasing levels of adsorbed carbon on the target surface due to the sputtering of adsorbed C species [24,25]. The onset of reactive sputtering was identifiable by a sharp increase in voltage. In other experiments, voltage hysteresis was observed as expected [25] upon reducing the C_2H_2 flow rate. The onset of reactive sputtering occurred at lower C_2H_2 flow rates for the 3.1 W/cm^2 target power density level (17 sccm) as compared to the 4.1 W/cm^2 level (23 sccm), for example.

4.2.1.3   Design of Experiments

The following three reactive sputtering process conditions were evaluated as experimental factors: C_2H_2 flow rate (Q_{C2H2}), applied d.c. bias voltage to the substrate (V_b), and substrate carousel rotation rate (ω_{Rot}). The process conditions corresponding to each factor level are listed in Table 4-1. Since each deposition system is unique, the parameter setpoints may not be broadly applicable. However, the range of the factor settings provides insight into the sensitivity of the film growth process. A set of twelve films was deposited according to a 2^3 factorial design, including two "center point" replicate films deposited under identical conditions. In addition, one film at the high and one at the low Q_{C2H2} levels with center V_b and ω_{Rot} levels were deposited. The high and low factor levels in Table 4-1 were selected to vary symmetrically around a desirable

center point, which had an unlubricated sliding friction coefficient of < 0.10 against steel. The measured system pressure did not change appreciably across the tested range of Q_{C2H2}. As discussed later in Section 4.4.2.2, the bombarding ion energy at the substrate is believed to vary linearly with V_b due to the low processing pressure (i.e., collisionless sheath assumption supported by the long mean free path as discussed previously).

Table 4-1. Factor level settings.

Factor	Level		
	-	0	+
Applied d.c. bias voltage (V_b)	-150 V	-100 V	-50 V
Substrate carousel rotation rate (ω_{rot})	2.0 rpm	2.5 rpm	3.0 rpm
Acetylene feed gas flow rate (Q_{C2H2})	45 sccm	55 sccm	65 sccm

Film composition and structure data were collected for each treatment and analyzed using multiple linear regression techniques [26] with SAS JMP statistics software. The models were constructed using Q_{C2H2}, V_b, and ω_{Rot} as the independent variables. The full factorial experimental design permitted an evaluation of potential first-order terms (e.g., coef.*Q_{C2H2}) and second-order interactions (i.e., coef.*Q_{C2H2}*V_b) only. The lowest order model with a 95% or higher confidence level on each term via individual t-tests was calculated. Each overall model was significant at a 99% confidence level according to analysis of variance calculations. An R^2_{adj} statistic (similar to R^2 but normalized by the model degrees of freedom) was used to further evaluate how well the model fit the data. Additional details about the statistical analyses can be found in the work of Montgomery [26].

4.2.2 Chemical Composition

X-ray photoelectron spectroscopy (XPS) was conducted with a PHI 5600 ESCA system using an Al K_α monochromatic x-ray source and equipped with a PHI 04-303 sputter gun. The films behaved like conductors during XPS analysis, and the binding energy scale was set using surface tantalum oxide species as an energy reference (Ta$4f_{7/2}$ ~ 26.0 eV) before sputter cleaning. Surface charging was not a noticeable problem. Sputter depth profiling was conducted for 180s to remove surface contamination and to evaluate the composition throughout the film. The sputter rate was 5.7 nm/min as calculated using a Ta_2O_5 calibration standard. Contaminants were removed during the first 40 s of sputtering, and the Ta, C, and O composition profiles remained at nearly constant levels for the remainder of the depth profile. The average Ta, C, and O at.% levels were calculated from the data collected during the final 140 s of depth profiling (~13 nm of depth). The output of this approach was an average composition for each lamellar film rather than an exact bulk composition as might be expected for a homogeneous material. The results were intended to show relative average composition differences between the samples. Normalized Ta/C and O/C atomic ratios were reported because the XPS composition data neglected hydrogen content. Physical Electronics Multipak v6.1a software was used for peak fitting. Gauss-Lorentz peaks were fit to the C1s, Ta4f, and O1s peaks after Shirley integrated background subtraction to estimate peak positions.

The hydrogen concentration in the films was measured using elastic recoil detection analysis (ERDA). A 4 MeV beam of alpha particles was used to dislodge hydrogen atoms in the top ~1 μm of film depth, which were then filtered using Al foil and detected.

The technique was calibrated using mica and carbon tape standards, and the measurement error was estimated to be ±5%.

4.2.3 Structure Characterization

An Amray scanning electron microscope (SEM) was used to measure the film thickness in cross-section at the cleaved edge of the film-coated Si wafers. Energy dispersive spectroscopy was used to measure the film Ar concentration in the same SEM.

Grazing incidence low-angle x-ray diffraction was performed on the TaC/a-C:H layers using a PANalytical X'Pert Pro instrument with a Cu K_α x-ray source. The scans were conducted over a 15-85° 2θ angle range, with a step size of 0.02° and a dwell (counting) time of 1 s at each step. A grazing angle arrangement was used, with the angle of the beam to the substrate held fixed at 0.6° (omega). High angle scans were performed as a contrast to the low-angle configuration. While Si substrate and Ta metal interlayer peaks were observed in the high angle scans, the grazing angle scans revealed only TaC peaks consistent with the TaC/a-C:H layer structure. A 10-point fast Fourier transform (FFT) smoothing operation was performed on the spectra, followed by a linear baseline subtraction. The broad TaC peaks in the spectra were curve fit using Lorentzian peaks, and the Scherrer equation was used to calculate the average TaC grain size based on the (111) peaks. Although there was overlap with the (200) peaks, the (111) peaks were the most intense and gave the most repeatable curve-fitting results. The average crystallite size estimates represent the lower limit, since instrument and stress peak broadening were neglected.

Micro-Raman spectroscopy was performed in the backscattering configuration to evaluate the a-C:H structure in the TaC/a-C:H films. Scattering signals were collected at room temperature from a Jobin-Yvon Horiba LabRam Micro-Raman instrument with a 20 mW HeNe laser (632.8 nm wavelength). Density filters were used to attenuate the incident beam such that spectra were obtained with either 0.2 mW or 2 mW of incident laser power with the laser beam focused to a spot several micrometers in size. Beam damage was not apparent on the film surface or in the spectra at the 0.2 mW power level. All spectra at each power level were acquired under steady state conditions with exactly the same acquisition settings to facilitate the comparison of peak intensities on a relative basis as a measure of scattering signal strength. Raw Raman spectra in the energy range of 900-1800 cm^{-1} were fitted with a linear background and two Gaussian peaks. Fits with Breit-Wigner-Fano and Lorentzian lineshapes, which are sometimes utilized for nanocrystalline graphite, a-C, and ta-C spectra [27], did not represent the data as well as two Gaussians for the TaC/a-C:H films.

Film structure imaging and electron diffraction were performed with a Hitachi HF2000 FEG transmission electron microscope (TEM) using a 200 kV electron beam. Cross-sectional film samples were prepared using focused ion beam milling with Ga^+ ions in a Hitachi FB-2000 FIB system. The "lift-out" method with a micro-sampling apparatus was used to prepare the samples. A tungsten film was deposited on each film surface for protection during ion milling. Line trace x-ray energy dispersive spectroscopy was performed in a Philips CM-200 FEG TEM (200 kV) equipped with EMI-Spec post-specimen scan coils and an Oxford Pentafet ATW2 energy dispersive spectrometer with a Moxtek ultrathin polymer detector window.

4.3   RESULTS

The experimental composition and structure results for the TaC/a-C:H films are listed

in Table 4-2. The films labeled *B* and *J* were replicates to confirm the repeatability of the

deposition process and to improve the confidence level of the statistical data analyses.

Multiple regression models for certain observations are shown in Table 4-3. Linear fits

were used to identify the response direction of change (i.e., the trends) with respect to the

deposition process parameter settings.   The coefficient estimate for each significant

model term indicated the magnitude and direction of the effect for that factor on the

response model. Increasing a parameter setting with a positive coefficient corresponded

to an increase in the response value, whereas a negative coefficient indicated an expected

decrease in the response.   Although the substrate rotation rate was not a statistically

significant factor for the models in Table 4-3, it had an impact on film structure as

revealed in TEM observations discussed later.

Table 4-2. TaC/a-C:H film identification and results.

Film ID	Q_{C2H2} (sccm)	V_b (V)	ω_{Rot} (rpm)	Ta/C Atomic Ratio	O/C Atomic Ratio	Hydrogen level (at.%)	Film Thickness (μm)	TaC Crystallite Size** (nm)	ID/IG Ht. Ratio	G Position (cm-1)	G Width (cm^{-1})	Deposit Thickness per Revolution (nm)
A	45	-100	2.5	0.65	0.07	14	1.9	2.5	1.3	1534	152	8
B*	55	-100	2.5	0.26	0.02	27	2.4	1.9	1.1	1533	165	-
C	65	-100	2.5	0.16	0.03	38	2.7	1.6	1.0	1531	179	12
D	45	-150	3.0	0.51	0.03	17	1.8	2.5	1.3	1538	164	7
E	65	-150	2.0	0.16	0.02	28	2.5	1.6	0.9	1530	179	-
F	45	-150	2.0	0.52	0.03	22	1.8	2.5	1.3	1538	151	11
G	65	-50	2.0	0.17	0.07	37	2.8	1.6	0.9	1532	173	-
H	45	-50	2.0	0.51	0.05	17	2.1	2.3	1.5	1544	139	11
I	65	-50	3.0	0.17	0.04	45	2.6	1.4	1.0	1531	168	-
J*	55	-100	2.5	0.29	0.03	26	2.2	1.8	1.1	1531	177	10
K	65	-150	3.0	0.15	0.02	26	2.4	1.6	1.1	1532	181	-
L	45	-50	3.0	0.43	0.08	24	2.0	2.2	1.7	1547	146	-
Measurement Error Estimate →				± 0.03	± 0.02	± 5%	± 0.1 μm					± 1 nm
Measurement Technique →				XPS	XPS	ERDA	SEM	XRD	Raman	Raman	Raman	TEM

* Films B and J are replicates
** Results represent the lower limit of average size, since instrument and strain broadening were neglected.

Table 4-3. Multiple linear regression models for observations. Non-significant terms were left blank in the table. The t-test p-value is listed below each term coefficient in parentheses.

Model Terms →	Intercept	$\left(\dfrac{Q_{C2H2}-55}{10}\right)$	$\left(\dfrac{V_b-(-100)}{50}\right)$	$\left(\dfrac{Q_{C2H2}-55}{10}\right)\left(\dfrac{V_b-(-100)}{50}\right)$	Whole Model $R^2_{Adj.}$
Ta/C Atomic Ratio	0.332	-0.180 (<0.0001)	-	-	0.90
Hydrogen (at.%)	26.617	7.909 (0.0001)	3.874 (0.0144)	3.321 (0.0285)	0.85
Film Thickness (μm)	2.252	0.333 (<0.0001)	0.130 (0.0022)	-	0.94
I_D/I_G Ht. Ratio	1.183	-0.227 (<0.0001)	-	-	0.78
$G_{position}$ (cm^{-1})	1535.092	-4.540 (0.0032)	-	-	0.56
G_{width} (cm^{-1})	164.446	12.856 (<0.0001)	-6.085 (0.0194)	-	0.82
Argon (at.%)	0.326	-	-0.008 (<0.0001)	-	0.78

The deposition process factors were abbreviated as follows: C_2H_2 flow rate (Q_{C2H2}), applied d.c. bias voltage (V_b), and substrate carousel rotation rate (ω_{Rot}). Since V_b was cathodic, the numerical bias values were negative. The regression models were calculated using the range −150 V to −50 V, so a higher $|V_b|$ value was increasingly negative in the models and plots.

An advantage of factorial designed experiments is that statistically significant response trends can be revealed with a minimum number of experiments. This is mathematically possible by adjusting multiple parameter settings within each experiment rather than testing one at a time. However, it can be misleading to interpret data from factorial experiments on two-dimensional plots without understanding that some data scatter may be due to changes in variables other than the one specified on the independent axis. To retain the visual simplicity of two-dimensional trend plots and to remind the reader of the factorial experimental design, each datum is labeled with a code

that identifies the test film in Table 4-2. The deposition conditions for each test film may then be referenced and compared accordingly.

4.3.1   Chemical Composition

The film Ta/C atomic ratio level depended only on Q_{C2H2} (Figure 4.2) within the studied parameter space. As Q_{C2H2} increased, the Ta/C atomic ratio decreased. The chemical coordination of carbon in the films was indicated by binding energy shifts in the C1s peak contributions from x-ray photoelectron spectra. Figure 4.3(a) shows these shifts as a function of Q_{C2H2} in a stack plot of C1s peaks. The peak at 282.6 eV was consistent with carbon in the TaC_x configuration [28]. The remainder of the carbon peak at higher binding energies, centered at ~284-285 eV, was consistent with a variety of carbon-carbon bonding configurations [29]. The higher binding energy tail of the C1s peak usually attributed to carbon-oxygen bonding configurations was not substantial for the TaC/a-C:H samples. Figure 4.3(b) shows that the carbide portion of the C1s peak area correlated only with Q_{C2H2}, much like the Ta/C ratio shown in Figure 4.2. This suggested that the majority of Ta in the films was bonded to carbon in a TaC_x configuration.
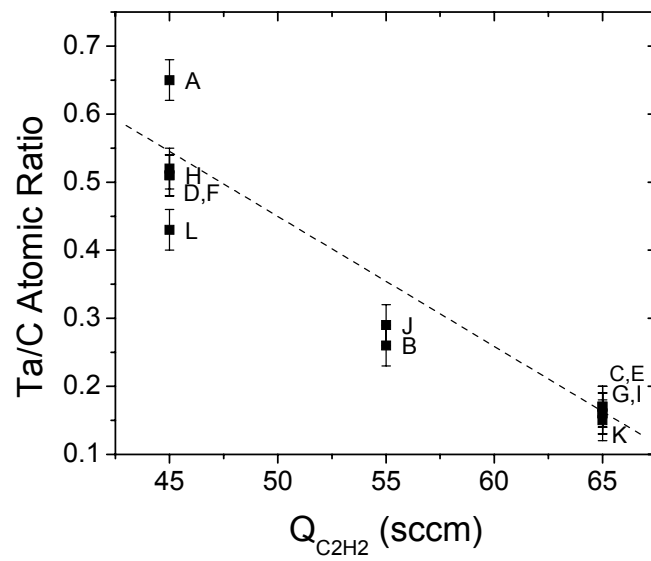
Figure 4.2. Ta/C atomic ratio from x-ray photoelectron spectroscopy as a function of Q_{C2H2}. Labels indicate the film ID for each data point.
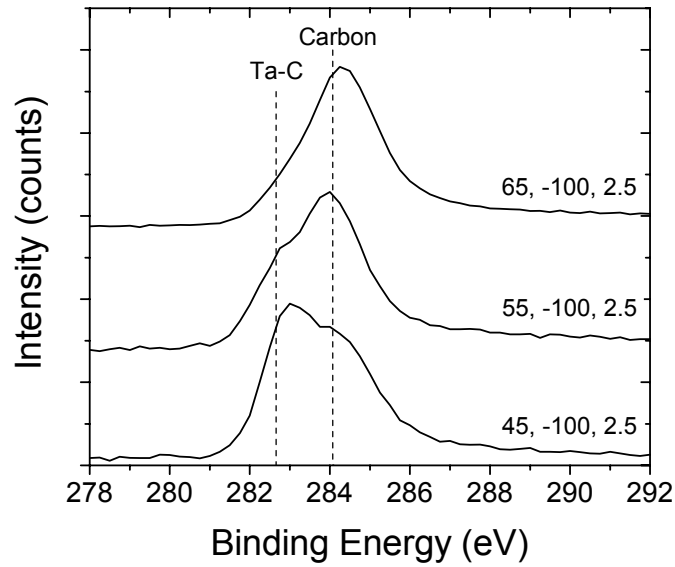
(a)
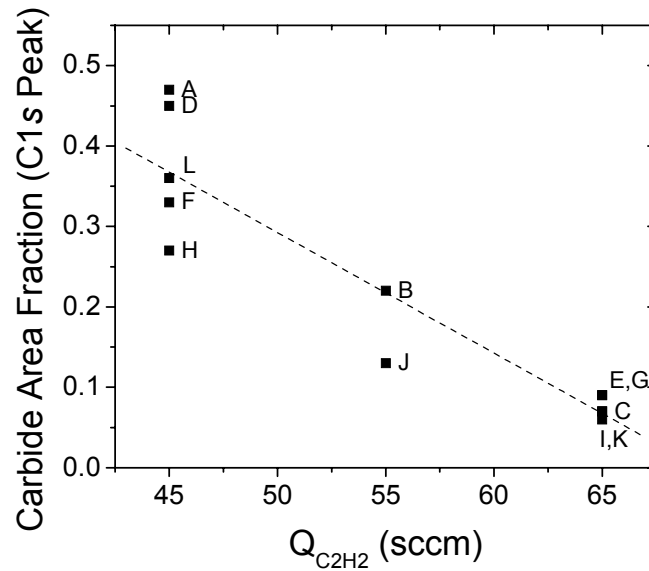
(b)

Figure 4.3. The C1s peak shape from x-ray photoelectron spectroscopy indicated the relative amount of TaC in the films. (a) Stack plot showing the contribution of TaC to the total C1s peak with increasing Q_{C2H2}. The peaks are labeled by the experimental factor levels in the following order: Q_{C2H2} (sccm), V_b (V), and ω_{Rot} (rpm). (b) Fraction of the C1s peak area attributed to the carbide peak for the TaC/a-C:H films.

The Ta4$f_{7/2}$ peak positions did not vary statistically with the deposition parameters. They were normally distributed with a mean of 23.25 eV and a range of 0.33 eV, which was consistent with TaC$_x$ [30]. Since the variation in Ta4$f_{7/2}$ peak positions did not vary systematically with deposition parameters, it is unlikely that the stoichiometry of the TaC phases varied significantly within the studied parameter space. No Ta4$f_{7/2}$ peak intensity was found around 21-22 eV, indicating a lack of metallic tantalum in the films. The film oxygen concentration did not exceed 6 at.% in these films. There was no convincing statistical correlation between the O/C atomic ratio and deposition factors.

The hydrogen concentration in the films increased with increasing Q_{C2H2}, as shown in Figure 4.4(a). Additional, less significant statistical relationships were found between hydrogen concentration and two other factors: V_b and the $Q_{C2H2}*V_b$ interaction (Table 4-3). As $|V_b|$ decreased, the film hydrogen concentration increased. The significant $Q_{C2H2}*V_b$ interaction factor indicated that the sensitivity of the effect of V_b on hydrogen level varied as a function of Q_{C2H2} and vice versa. This is illustrated in Figure 4.4(b), where the independent axis is V_b and the symbols denote various Q_{C2H2} levels. Hydrogen concentration in the films was more influenced by V_b at $Q_{C2H2} = 65$ sccm (higher positive slope) as compared to $Q_{C2H2} = 45$ sccm (lower positive slope).

Because ERDA probed the top ~1 μm of film depth, it was not possible to identify the exact location of hydrogen within the film structure. It was incorporated probably as part of the a-C:H matrix. If the Ta in the films was completely bound with C, and there was no H in the TaC, then the H level in the a-C:H matrix would be ~30-55 at.%. These hydrogen levels are within the allowable range for a random hydrocarbon network [31].
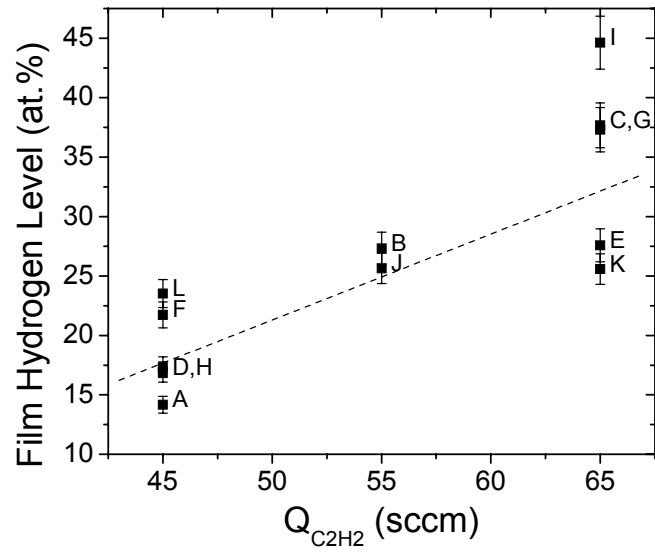
(a)
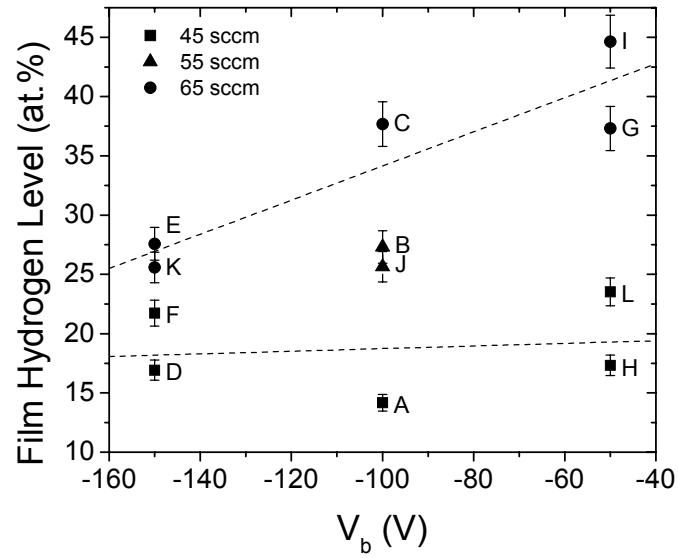
(b)

Figure 4.4. Hydrogen concentration as a function of (a) Q_{C2H2} and (b) V_b as measured with elastic recoil detection analysis. The error bars represent a ±5% error estimate per measurement.

4.3.2 Film Structure

The film thickness increased with increasing Q_{C2H2} as shown in Figure 4.5. It increased as $|V_b|$ decreased as a secondary correlation. Film thickness was not affected by ω_{Rot} statistically.
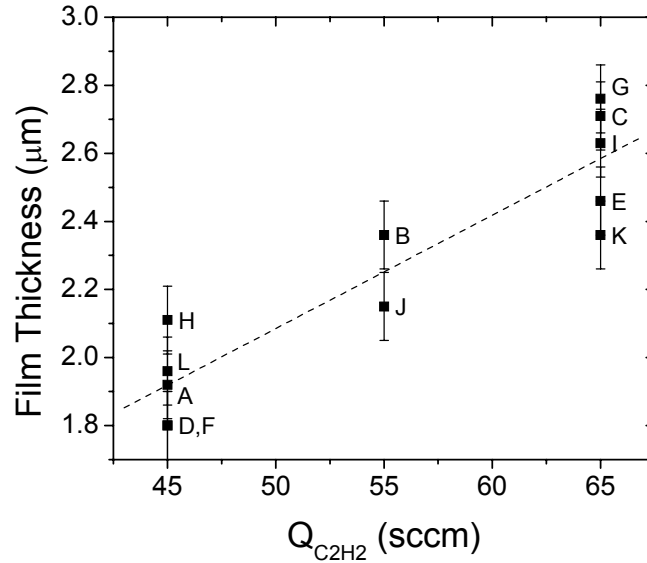
Figure 4.5. Film thickness as a function of Q_{C2H2}. The error bars represent a ±0.1 μm error estimate per measurement.

4.3.2.1 X-ray Diffraction

X-ray diffraction (XRD) spectra confirmed that the films contained TaC crystallites. Stacked spectra as a function of Q_{C2H2} are shown in Figure 4.6(a). Weak peak intensities at high 2θ made it impossible to precisely calculate lattice parameters, but calculations from the lower order peaks were consistent with expected values for TaC with the B1 (NaCl) structure type. No graphite or Ta_2C reflections were observed. The peaks became broader and less intense as Q_{C2H2} increased. Figure 4.6(b) shows that the average crystallite size as calculated using the Scherrer equation [32] decreased with increasing

Q_{C2H2}. The crystallite size also appears to have increased with increasing $|V_b|$. However, it should be noted that the peak fitting error increases for increasingly broad peaks such as those observed in this study. In addition, the ~1.5-2.5 nm crystallite size range is approaching the limit of applicability for the Scherrer equation. For these reasons, the regression model for the XRD data has limited utility and is not included in Table 4-3. On the other hand, the relative trend with respect to Q_{C2H2} appeared to be significant. Contributions to peak widths due to instrument or strain broadening were not taken into account, so the calculated crystallite sizes represent the lower limits. No correlation of crystallite size with ω_{Rot} was observed.
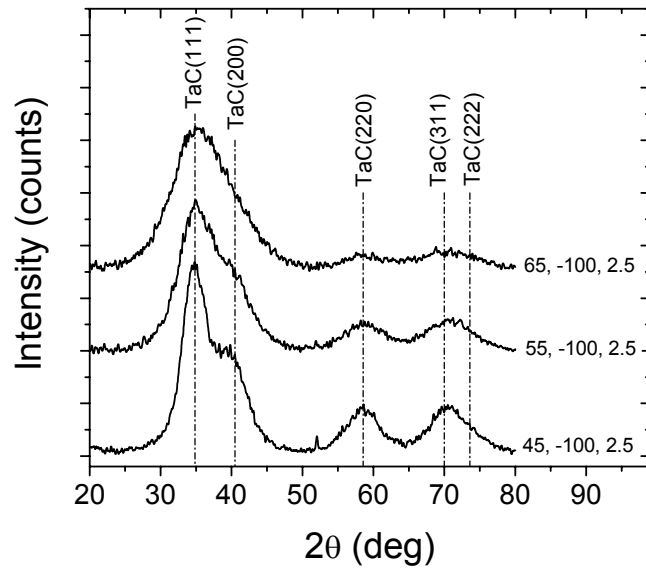
(a)
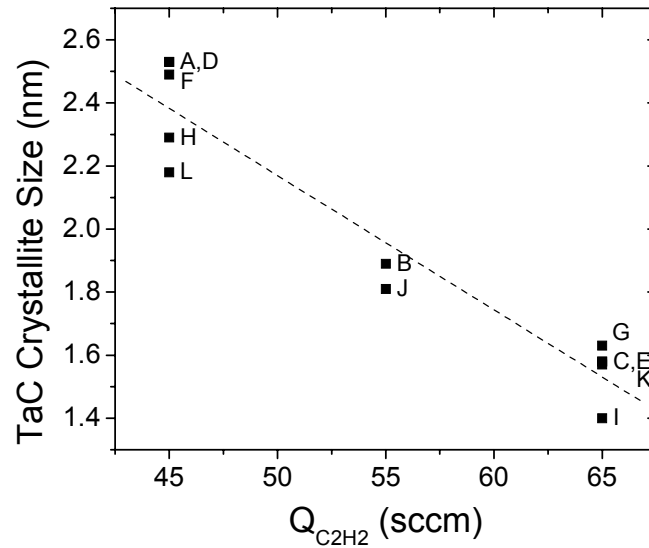
(b)

Figure 4.6. Grazing angle x-ray diffraction spectra indicated B1-TaC crystallites in the films. (a) Stacked spectra showing the effect of increasing Q_{C2H2} on the dilution of TaC crystallites. The spectra are labeled by the experimental factor levels in the following order: Q_{C2H2} (sccm), V_b (V), and ω_{Rot} (rpm). (b) Relationship between the calculated average crystallite size and Q_{C2H2}.

4.3.2.2   Raman Spectroscopy

Raman spectroscopy was used to characterize the structure of non-carbidic film volume. Perfect TaC crystals do not have a first-order Raman scattering signal because of their B1 (NaCl) crystal structure type [16,33]. Raman spectra for the films indicated one broad peak between 1000 and 1800 cm^{-1}, characteristic of disordered carbon [27]. The G peak between 1500 and 1600 cm^{-1} resulted from the stretching vibration of pairs of Csp^2 sites, and the D peak between 1300 and 1400 cm^{-1} was attributed to a breathing mode of Csp^2 sites in rings [34]. Although Raman scattering does not detect C-H bonds directly, linked Csp^2 content within the a-C:H phase can be evaluated by fitting G and D peaks to the broad peak in the 1000-1800 cm^{-1} region of the spectrum [34,35].

The I_D/I_G peak height ratio and D peak position increased linearly with increasing G position for the TaC/a-C:H films, consistent with the results of Tamor [35] for a-C:H films. At a constant laser power level (0.2 mW), the total a-C:H peak area increased with increasing Q_{C2H2}, suggesting therefore a higher volume fraction of a-C:H matrix. Figure 4.7(a) shows fitted Raman spectra for increasing Q_{C2H2} at 0.2 mW laser power. The use of filters to reduce the beam power from 20 to 0.2 mW was necessary to prevent damage of the films with high hydrogen content. However, the signal to noise ratio was not adequate for confident peak fitting results for those films with high Ta/C at that low laser power. Therefore, additional spectra were collected for the films deposited at $Q_{C2H2} = 45$ sccm with 2 mW laser power to enable accurate peak fitting. No beam damage under this condition was detected on the film visually or in the spectra for these measurements. When the peak fitting results from spectra collected at 0.2 mW (low Ta/C films) and 2 mW (high Ta/C films) were combined, the I_D/I_G peak height ratio decreased statistically

with increasing Q_{C2H2} (Figure 4.7(b)). This was consistent with an increased Tauc gap and an increase in Csp^3 sites in the film, most likely those bonded to hydrogen rather than tetrahedrally bonded Csp^3-Csp^3 diamond-like content [35]. The same interpretation was appropriate for the G peak position decrease with increasing Q_{C2H2}. An increase in G peak width correlates with bond angle disorder at Csp^2 sites [34,35]. The G peak width increased with increasing Q_{C2H2} and $|V_b|$ as indicated in Table 4-3 for the TaC/a-C:H films. It should be noted that prior to the application of the linear baseline correction to the spectra in Figure 4.7(a), films with the highest hydrogen concentrations had strong baseline intensity contributions from photoluminescence. This correlation has practical significance; for example, Adamopoulos et al. [36] used the Raman photoluminescence background as a non-destructive analytical method to estimate hydrogen concentration.
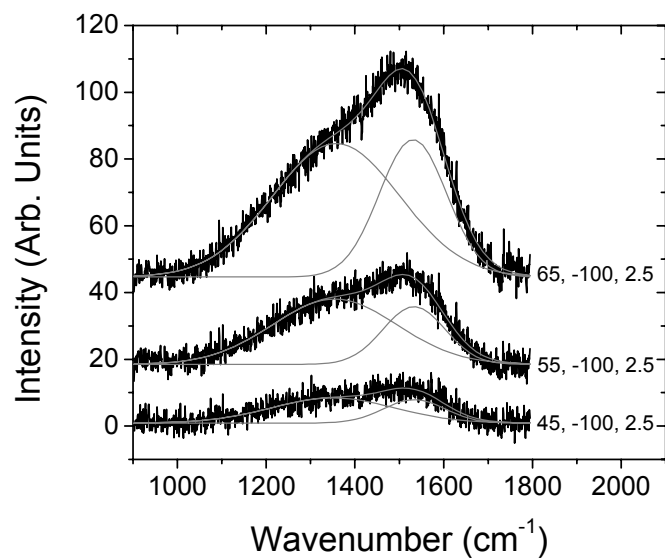
(a)
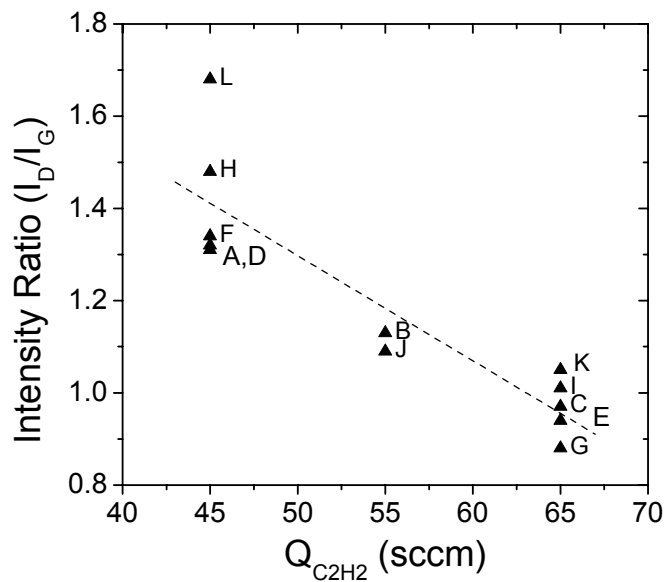
(b)

Figure 4.7. (a) Raman spectra for the films with fitted D and G peaks for increasing Q_{C2H2} (0.2 mW scans). The spectra are labeled by the experimental factor levels in the following order: Q_{C2H2} (sccm), V_b (V), and ω_{Rot} (rpm). (b) Correlation of I_D/I_G peak height ratio with Q_{C2H2}.

4.3.2.3   Transmission Electron Microscopy (TEM)

The cross-sectional structure of the films was examined through TEM. Data for the set of films selected for observation are listed in the final column of Table 4-2. The Ta-metal interlayer thickness in each sample was ~500 nm. The TaC/a-C:H total film thickness varied for each sample, with the relative differences apparent in Figure 4.5. The TaC/a-C:H top layer in each sample was homogeneous and dense on the micrometer scale (Figure 4.8). Selected area electron diffraction patterns from the top layer indicated face-centered cubic TaC, as expected from the XPS and XRD results. Diffraction rings with uniform intensity indicated randomly dispersed crystallites, and no crystallographic texture was observed in the cross-sectional orientation.
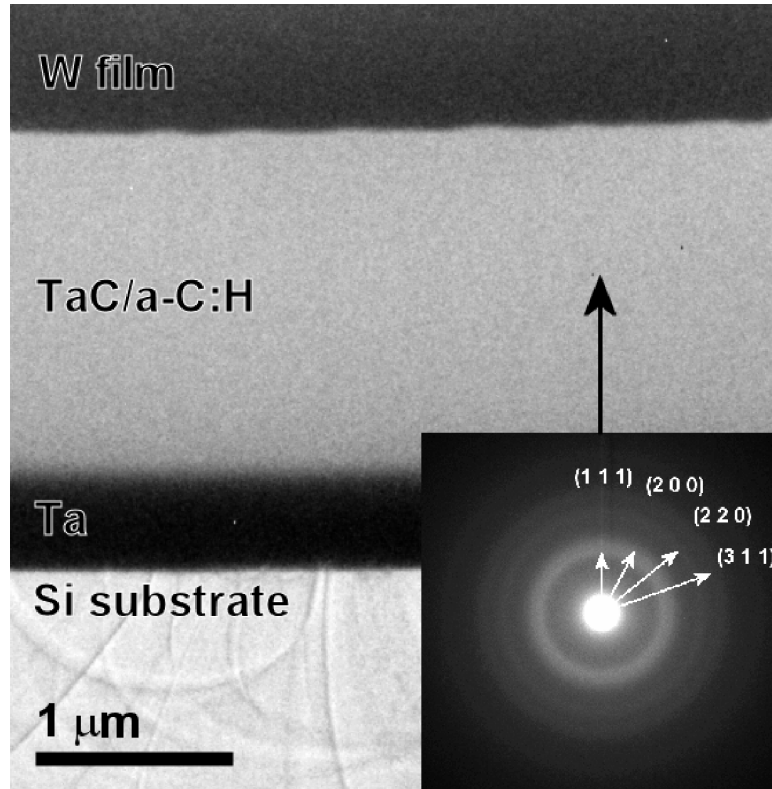
Figure 4.8. Cross-sectional TEM micrograph of the film with Q_{C2H2} = 55 sccm, V_b = -100 V, and ω_{Rot} = 2.5 rpm. A selected area diffraction pattern from the TaC/a-C:H layer is inset with B1-TaC indices for the indicated rings.

Heterogeneity in the film nanostructure was observed at higher magnification. Figure 4.9(a) contains a higher magnification cross-sectional view of the film deposited with Q_{C2H2} = 55 sccm, V_b = -100 V, and ω_{Rot} = 2.5 rpm. The structure was dense columnar with thin column boundaries and no significant inter-columnar voids. A lamellar structure with alternating dark and bright layers was observed in each film on the nanometer scale. The layers were mostly intact across columns but were discontinuous at the columnar boundaries. The layer contrast did not vary with specimen tilting and thus was attributed to Ta Z-contrast. Linear spatial profiling with x-ray energy dispersive spectroscopy (XEDS) further confirmed that the dark layers have a slightly higher Ta content than the bright layers. Figure 4.9(b) contains a scanning transmission electron

microscope image showing the line scan location and inset XEDS Ta peak intensity profile as a function of position along the line. Local maxima in Ta intensity corresponded with the position of dark layers. The C concentration results from the line scan were not quantifiable due to uncertainty about the extent of C K_α x-ray absorption in the detector window under the collection conditions. Qualitatively, differences in electron transparency suggested that the dark and bright layers had different densities. The high-resolution TEM micrograph shown in Figure 4.10 indicated that TaC crystallites were present throughout the dark and bright layers. Examination of the TaC crystallite–a-C:H matrix interface was not easily accomplished with FIB samples, which are typically thicker than conventionally ion milled specimens. Therefore, there was substantial overlap in lattice fringes through the thickness of the area. The TaC crystallite size range appeared to be consistent with the XRD Scherrer calculations, with a few observations of crystallite sizes up to 5 nm. The layer thickness ranged from ~2–3 nm for the samples studied.
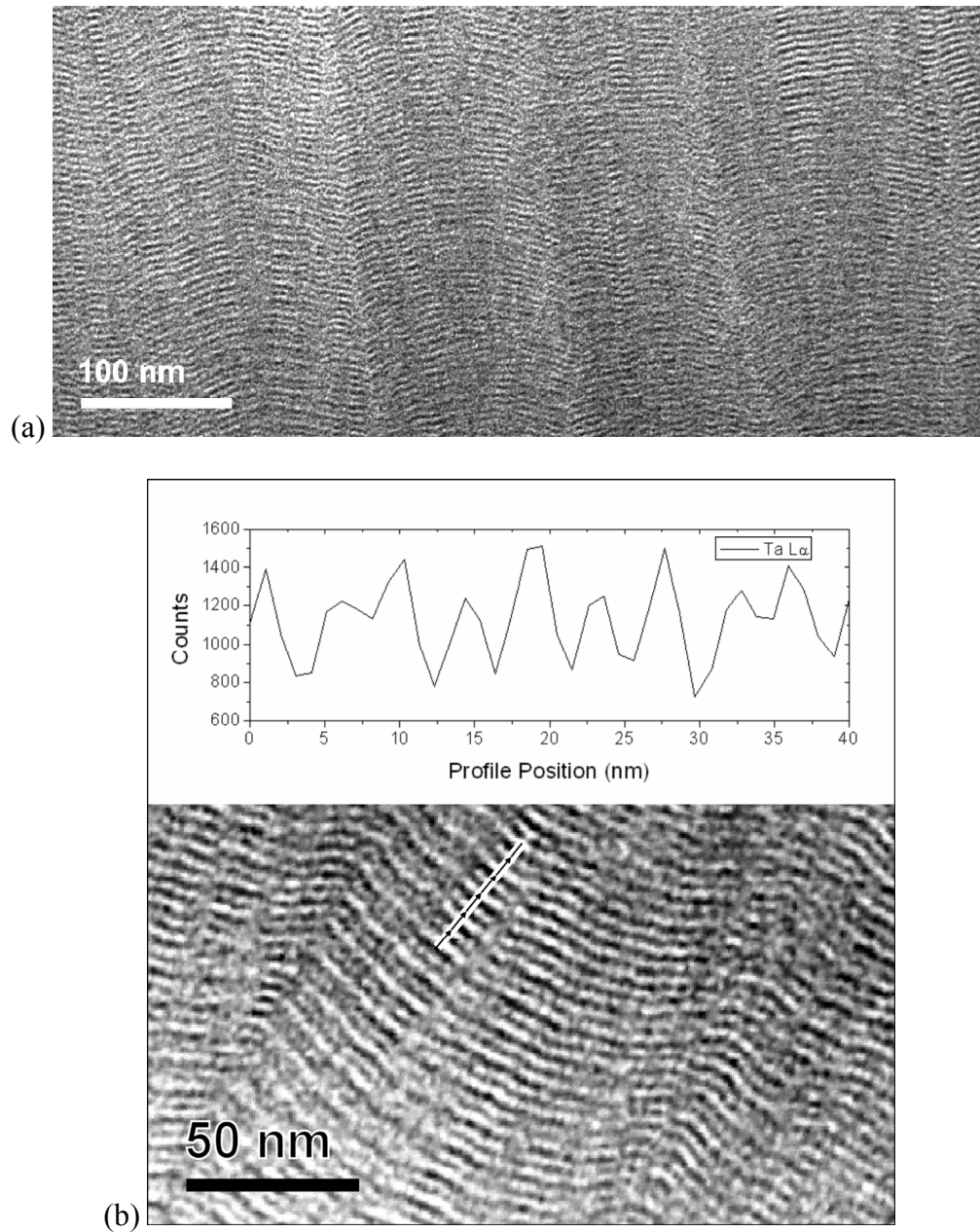
Figure 4.9. (a) Cross-sectional TEM image of the film with Q_{C2H2} = 55 sccm, V_b = -100 V, and ω_{Rot} = 2.5 rpm showing columnar and lamellar structure. (b) STEM image from the same film showing the XEDS line scan location. Inset is a plot of the XEDS data for the Ta L_α peak intensity as a function of position along the line profile.
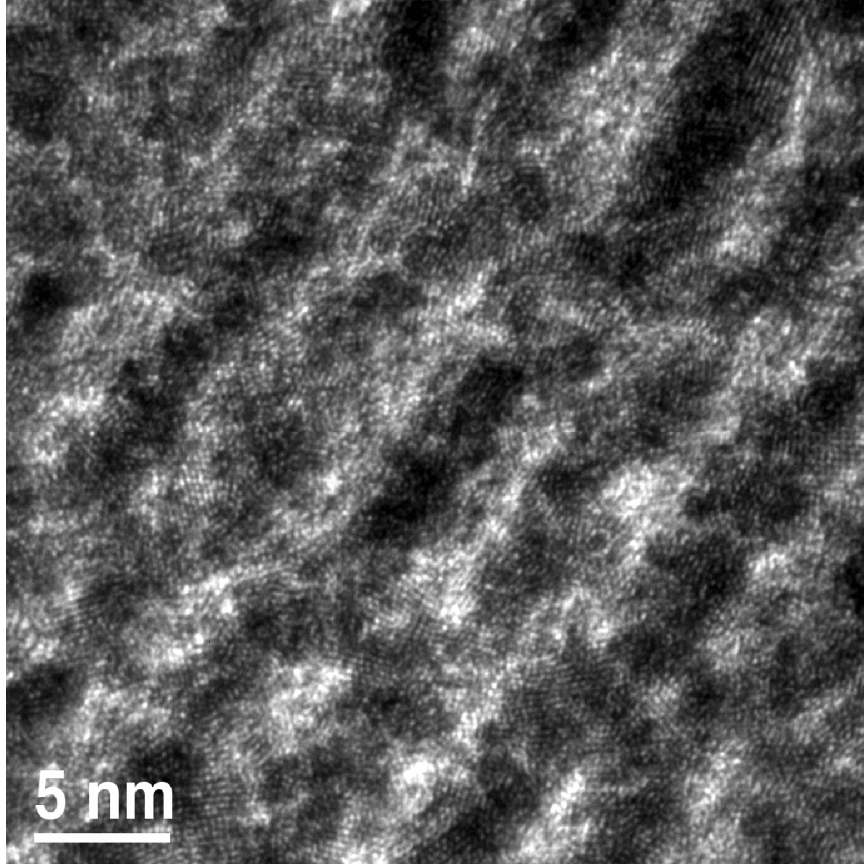
Figure 4.10. High resolution TEM image of the cross-sectional lamellar film structure for the film with Q_{C2H2} = 55 sccm, V_b = -100 V, and ω_{Rot} = 2.5 rpm.

The layer periodicity varied as a function of deposition parameters. The difference in layer periodicity is shown at equal magnification in Figure 4.11 for films deposited at ω_{Rot} = 2 and 3 rpm. If one Ta-rich dark layer resulted for each pass in front of a magnetron, then one complete rotation period corresponds to four alternating dark and bright layers. Measured deposit thickness per carousel revolution are listed in Table 4-2 and illustrated in Figure 4.11. The process parameter ω_{Rot} did not affect total film thickness statistically because differences in layer thickness were offset by differences in the total number of layers.
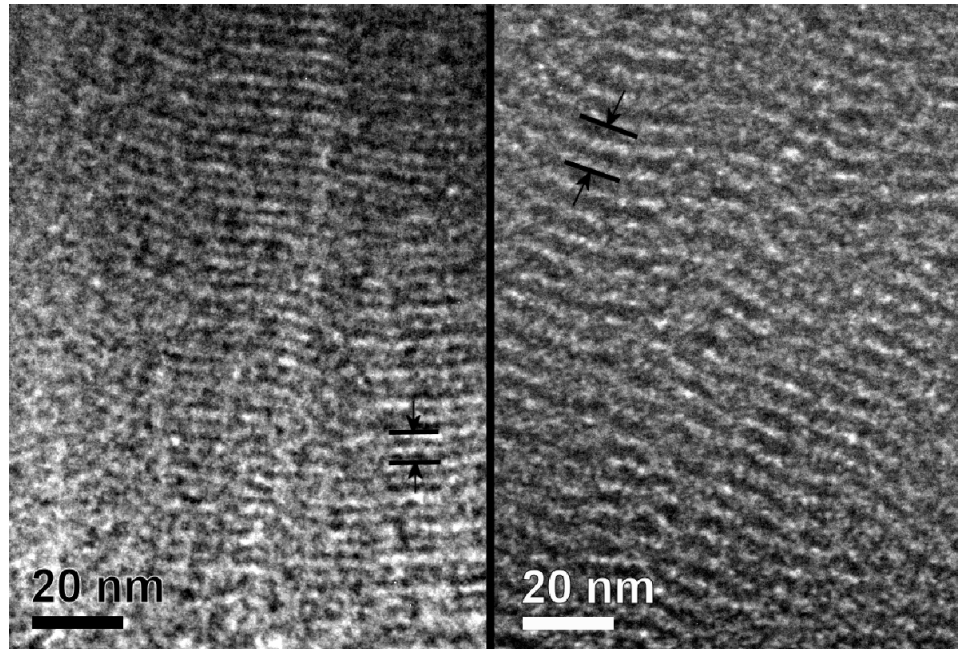
Figure 4.11. Comparison of the layer periodicity for ω_{Rot} = 3 rpm (left) versus 2 rpm (right). Both films were deposited with Q_{C2H2} = 45 sccm and V_b = -150 V. Annotations indicate the layer thickness for one period in each image (Table 4-2).

4.4   DISCUSSION

The experimental goal of this TaC/a-C:H thin film study was to identify direct trend relationships between deposition process parameters and film composition and structure. A furtherance of that effort was to interpret those trends using physical mechanisms that are applicable to reactive sputter deposition of MC/a-C:H films in general. The next section compares and contrasts the new TaC/a-C:H results with other MC/a-C:H data from the literature. The final sections discuss the results in the context of general film growth mechanisms that are characteristic of physical vapor deposition (PVD) and plasma-enhanced chemical vapor deposition (PECVD) processes.

4.4.1   Comparison of TaC/a-C:H Results with the MC/a-C:H Literature

The Ta/C atomic ratio in the TaC/a-C:H thin films increased with decreasing Q_{C2H2}, or more generally, with decreasing concentration of hydrocarbon species in the plasma

environment. Similar increases in metal/carbon (M/C) atomic ratio have been observed elsewhere for TaC/a-C:H [9,12,20] and WC/a-C:H [11,37,38,39,40] when the inlet hydrocarbon gas flow rate is decreased. The Ta/C level was not dependent on V_b statistically within the studied parameter space. With one exception [41], this insensitivity of M/C atomic ratio on V_b has been observed elsewhere for TiC/a-C:H [15,42] and WC/a-C:H [39].

The hydrogen concentration in the films increased in the TaC/a-C:H films with increasing Q_{C2H2} and decreasing $|V_b|$. The inverse correlation between hydrogen content and M/C atomic ratio has been observed in reactively sputtered MC/a-C:H films [9,11,43,44,45,46]. However, the most extensive discussions about the relationship between V_b and hydrogen level can be found in the a-C:H literature.

The total film thickness depended primarily on Q_{C2H2} and secondarily on V_b. Similar film thickness increases with increasing Q_{C2H2} have been reported for WC/a-C:H [8,40,47]. The TaC/a-C:H total film thickness was insensitive to ω_{Rot} statistically, an observation that is consistent with the results of Strondl et al. [48] for WC/a-C:H.

The XRD data for TaC/a-C:H indicated that the TaC crystallite size decreased with increasing Q_{C2H2} (Figure 4.6). Others have reported a similar relationship between decreased metal carbide crystallite size and increased flow rate of hydrocarbon gas during deposition [16,18,20,44,49]. The TaC/a-C:H data also appeared to indicate that the TaC crystallite size increased with increasing $|V_b|$. This result is not conclusive, since the uncertainty in applying the Scherrer equation to such broad XRD peaks overwhelms the statistical confidence in the regression analysis. The literature is somewhat contradictory on this topic. Shi and Meng [42] published high-resolution TEM images from TiC/a-C:H

117

films that suggested the TiC crystallite sizes slightly increased with increasing $|V_b|$ (i.e., ion energy). On the other hand, Zehnder et al. [50] observed a decrease in TiC crystallite size with increasing $|V_b|$ in TiC/a-C:H. It is noteworthy that Shi and Meng used d.c. substrate biasing while Zehnder et al. used rf biasing. The TaC/a-C:H films deposited with d.c. substrate biasing in the present study appear to be consistent with the Shi and Meng observations, but additional experimentation and analysis are necessary for confirmation.

Like the Ta/C atomic ratio, the Raman I_D/I_G ratio and G peak position depended only on Q_{C2H2} for the TaC/a-C:H films. Others have reported that a reduction in I_D/I_G [44] and G peak position [39] correlate with an increase in Csp^3-H content [27]. The TaC/a-C:H data were consistent with those observations, since the film hydrogen level was also primarily dependent on Q_{C2H2} (Figure 4.4(a)). On the other hand, the G width results that are associated with bond angle disorder in the Csp^2 content of the matrix [27] did depend statistically on V_b. The Raman scattering results were not dependent on ω_{Rot} as observed for WC/a-C:H films [48] deposited using similar equipment.

The nanometer-scale lamellar film structure was observed elsewhere for films deposited using reactive sputtering with substrate rotation [20,38,48]. Others have identified similar dependencies of layer periodicity on Q_{C2H2} [51] and ω_{Rot} [48] as those reported in Table 4-2 for the TaC/a-C:H films.

As shown above, some of the directional correlations between TaC/a-C:H film properties and deposition parameter settings were generally consistent with observations in the literature for MC/a-C:H films deposited using similar processes. Therefore, elements of the subsequent framework for understanding reactively sputtered TaC/a-C:H

film growth may be generally applicable to MC/a-C:H films deposited using similar processes.

4.4.2 Deposition Mechanisms

The reactive sputtering process used to deposit TaC/a-C:H films in this study included d.c. magnetron sputtering with simultaneous d.c. substrate biasing in an Ar/C_2H_2 plasma environment. It is proposed that certain aspects of film deposition can be understood in terms of growth mechanisms characteristic of both PVD and PECVD. The TaC/a-C:H experimental trends revealed that the overall film composition and structure depended mostly on two deposition factors: Q_{C2H2} and V_b. The effects of each factor on TaC/a-C:H film growth are considered within the framework of hypothesized and proven PVD and PECVD deposition mechanisms in the following sections.

4.4.2.1 Physical Vapor Deposition (PVD)

When a reactive gas such as C_2H_2 is added to the plasma environment during magnetron sputtering, hydrocarbon species adsorb onto the targets. This is evidenced by an increase in target operating voltage at a constant power level for increased Q_{C2H2}. Both Ta and adsorbed C are sputtered from the targets at steady-state. This produces a flux of mostly neutral atoms that bombard the substrates with an average kinetic energy approaching ~5 eV, which is typical for low-pressure sputtering processes [52]. Therefore, the PVD component of film growth contributes a flux of neutral, slightly hyperthermal Ta and C to the growing film surface.

Cross-sectional TEM micrographs (e.g., Figures 4.9-4.11) indicated that the substrate received a layer of sputtered Ta (and presumably C) with each pass in front of a target (dark layers), whereas the bright layers presumably represented the portion of the cycle

when the substrates were positioned away from the targets (e.g., the location of the substrate shown in Figure 4.1). Although the highest flux of Ta to the film surface occurred when the substrates faced the targets, it was possible for sputtered material to reach the substrates when they were facing away from the targets. Bewilogua et al. [38] quantified the difference in W/C atomic ratio for WC/a-C:H films deposited on substrates positioned directly facing and perpendicular to the targets. Low levels of W were found even when the substrates were facing away from the targets, suggesting that sputtered atoms reached them by scattering or other processes. This observation was confirmed for the TaC/a-C:H system in the present deposition chamber by reproducing the Bewilogua et al. experiment. The diffuse interfaces between dark and bright layers in the TaC/a-C:H films may be partly attributable to the variation in flux rate of sputtered material as a function of substrate position during carousel rotation.

The film Ta/C atomic ratio was dependent on Q_{C2H2} only for the TaC/a-C:H films. From the PVD perspective, this might have been due in part to increased adsorption of C on the Ta-target surfaces with increased Q_{C2H2}, resulting in a flux of sputtered material with a lower Ta/C ratio. Likewise, the reduction in TaC crystallite size at high Q_{C2H2} could have been the result of a more C-rich flux of sputtered material to the film surface. The sensitivity of layer periodicity to ω_{Rot} as seen in Figure 4.11 and dark-bright image contrast suggests that extensive homogeneous mixing of surface species in the direction normal to the surface did not occur during growth. Rather, the lamellar film structure suggested that the surfaces received a modulated flux of sputtered Ta and C, with a frequency that depended on ω_{Rot} and a flux amplitude that depended on the substrate location with respect to the Ta target faces. TaC crystal nucleation probably occurred by

a mechanism such as Volmer-Weber island growth [53], given the expected surface free energy dissimilarity between TaC and a-C:H. Determining the precise mechanism of TaC crystallite nucleation is a topic for further study.

4.4.2.2 Plasma-enhanced Chemical Vapor Deposition (PECVD)

The mechanisms for PECVD of a-C and a-C:H thin films were described in notable reviews by Angus [54] in 1988 and later by Robertson [34] in 2002. A key component of growth models for amorphous carbon films, such as energetic condensation [55] and subplantation [56,57,58], is energetic ion bombardment of the film surface during growth. While C atom subplantation critically influences the properties of a-C films, recent work has revealed the importance of hydrogen in the plasma discharge during a-C:H growth. Nuclear magnetic resonance spectroscopy measurements by Grill et al. [59] indicated that practically all Csp^3 sites were bound to at least one H atom in hard a-C:H films deposited by rf-PECVD of C_2H_2. Von Keudell et al. [60] proposed a two-zone model for a-C:H film growth that emphasized the role of hydrogen abstraction reactions to create dangling bonds (such as H + C-H $\rightarrow$ C- + H_2) at various depths in the growing film. The "chemistry-dominated" growth zone extends from the surface to depths of ~ 1-2 nm. In experiments with a methyl radical source, von Keudell et al. [61] found that the sticking coefficient for CH_3 radicals on an a-C:H surface increased from ~10^{-4} to ~10^{-2} by the addition of atomic hydrogen to the beam. The atomic hydrogen reacts with bound surface hydrogen to produce H_2 and dangling bond reaction sites for unsaturated C_xH_y radicals. Energetic ion bombardment also may affect the chemistry-dominated growth zone. Robertson [34] suggested that deposition with higher $|V_b|$ levels may result in lower a-C:H film hydrogen levels because heavy ions (e.g., Ar) preferentially displace H

from C-H bonds, creating dangling bonds that are available to react with C_xH_y species. The von Keudell et al. "ion-dominated" growth zone may extend to depths of up to ~10 nm, depending on growth conditions. Only hydrogen ions that are accelerated by V_b have the kinetic energy to penetrate into this subsurface zone. Hydrogen abstraction, resaturation, H_2 desorption, and dangling bond creation can occur in the ion-dominated zone, giving it a critical role in film structure development during deposition [60].

To estimate the extent of the ion-dominated growth zone for the TaC/a-C:H experimental conditions, the Transport and Range of Ions in Matter (TRIM) Monte Carlo algorithm [62] was used to conduct ion implantation simulations. The implantation depth of ions and sputter yields were simulated for two types of targets to approximate the two phases in the TaC/a-C:H composites. The first target was TaC with a density of 14.5 g/cm^3 and a 1:1 Ta:C stoichiometry. The second target was meant to approximate the a-C:H phase, with 45 at.% H and 55 at.% C and an assumed density of 1.5 g/cm^3. The assumed density for the a-C:H phase was chosen using approximations based on hydrogen level [63] and other reported results from films deposited using similar precursors and energetics [16]. If a collisionless sheath is assumed at the low processing pressures of 0.1-0.3 Pa, the maximum ion energy may be approximated as $E_i = e|V_b| + eV_p$, where E_i is the bombarding ion energy in eV, e is the quantity of charge, and V_p is the plasma potential in volts [52]. The simulated implantation depths were plotted in Figure 4.12. Assuming $V_p \sim 20$ V and the process setpoint limits of $V_b = -50$ and -150 V, the range of interest in this study is ~70 − 170 eV. As expected, the hydrogen implantation depth in the hypothetical film materials was greater than two times that for bombarding Ar or C. However, the penetration depth of C and Ar exceeds ~1.5 nm in the

a-C:H phase at the high end of the $|V_b|$ range of the experimental parameter space. This suggests that C subplantation and Ar implantation/peening were also occurring in the TaC/a-C:H depositions. Experimentally, Ar was found in the TaC/a-C:H films with XEDS, and its concentration was statistically proportional to $|V_b|$ only (Table 4-3). Since Ar is inert, the low levels in the films (< 2 at.%) were implanted during growth. This experimental result corroborated the TRIM implantation depth simulations and confirmed the sensitivity of implantation depth to V_b level during deposition.
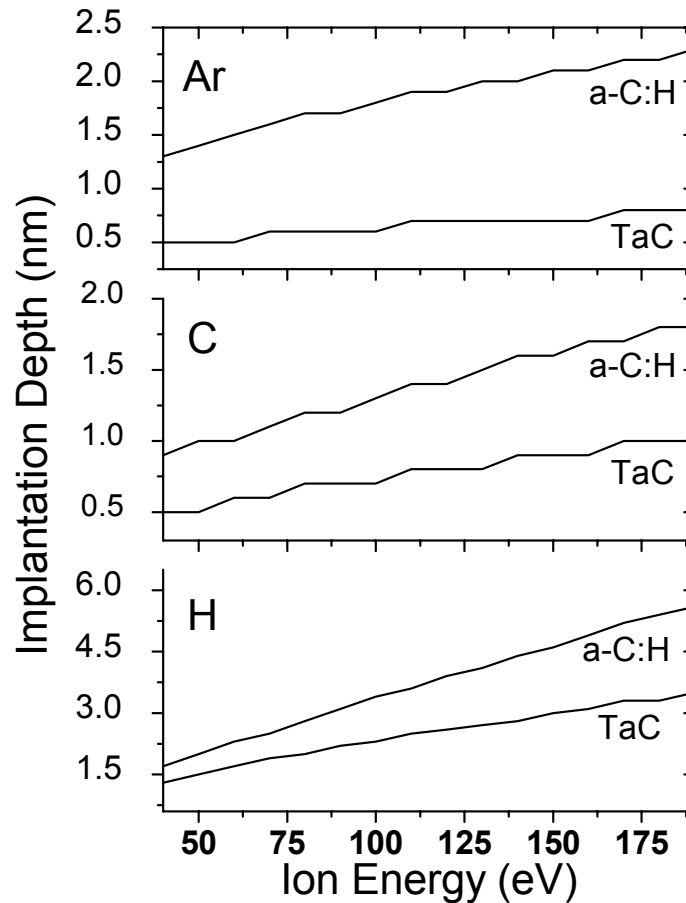
Figure 4.12. Implantation depth plots calculated with the TRIM computer algorithm. Ion bombardment was simulated for an assumed TaC surface (50 at.% Ta and 50 at.% C with density = 14.5 g/cm^3) and a-C:H surface (45 at.% H and 55 at.% C with density = 1.5 g/cm^3).

123

From the PECVD perspective, the overall Ta/C atomic ratio in the TaC/a-C:H films may have decreased with increasing Q_{C2H2} due to an increased deposition rate of a-C:H. A plasma environment enriched with hydrogen and hydrocarbon species at high Q_{C2H2} may have increased the level of activity in the chemistry-dominated growth zone at the surface. This hypothesis is supported by TEM measurements in Table 4-2, which show that the layer periodicity (thickness) increased with increasing Q_{C2H2} at constant V_b. The total film thickness likely increased with increasing Q_{C2H2} for the same reason. The statistical independence of Ta/C atomic ratio on V_b was noteworthy. TRIM-simulated sputter yields for species from TaC and a-C:H surfaces under Ar^+, C^+, and H^+ bombardment within the applicable energy ranges did not exceed ~0.25. This suggests that selective sputtering of Ta or C from the growing film surface in these experiments was minor at the V_b used. However, it is acknowledged that the confident interpretation of sputter yield results from TRIM was limited because surface damage and crystallographic effects on the surface binding energy were not simulated.

The TaC/a-C:H film hydrogen concentration dependence on Q_{C2H2} and V_b suggests the significant role of both surface and subsurface PECVD processes during growth. The correlation between film hydrogen level and Q_{C2H2} was attributed to the dependence of surface processes in the chemistry-dominated growth zone on the composition of the plasma environment. On the other hand, the inverse correlation between film hydrogen content and $|V_b|$ indicated the importance of hydrogen abstraction and H_2 desorption processes in the subsurface ion-dominated growth zone [60]. TRIM simulations based on the TaC/a-C:H experimental parameter space (Figure 4.12) suggested that the hydrogen implantation depth (i.e., depth of the ion-dominated growth zone) nearly doubled

between V_b = -50 and -150V. Hydrogen atom penetration to such depths likely required passage through both a-C:H and TaC phases because of the lamellar film structure. This fact distinguishes the composite TaC/a-C:H films from single-phase a-C:H films, but is not expected to affect the hypothesized processes in the ion-dominated growth zone. The statistically significant Q_{C2H2} * V_b interaction term (Figure 4.4(b)) was consistent with the link between V_b (depth of ion-dominated growth zone) and Q_{C2H2} (composition of both growth zones) from the von Keudell et al. model [60]. The effect of V_b on film hydrogen concentration was more pronounced in films with higher a-C:H fractions due to the increased availability of C-H sites for hydrogen abstraction, resaturation, dangling bond creation, and crosslinking reactions.

Increased ion peening [34,64] of the surface by Ar ions during growth may have also contributed to reduced hydrogen levels and produced a denser a-C:H phase at high $|V_b|$. The slight increase in Raman G peak width with increased $|V_b|$ indicates a higher degree of Csp^2 site disorder in the a-C:H phase [27], which is also consistent with a more compressed a-C:H phase at high $|V_b|$. A denser a-C:H matrix at high $|V_b|$ may explain the observation that the total film thickness slightly decreased with increasing $|V_b|$. However, the V_b effect on total film thickness was so subtle that TEM layer thickness measurements did not clearly indicate a dependence of lamellae thickness on V_b for Q_{C2H2} = 45 sccm and ω_{Rot} = 2 rpm (Table 4-2, both ~11 nm/rot).

4.5   SUMMARY AND CONCLUSIONS

Metal carbide/amorphous hydrocarbon (MC/a-C:H) thin films are being used on precision steel component surfaces as low friction, wear-resistant coatings. The purpose

of the present study was to deposit and analyze a set of TaC/a-C:H films in a statistically rigorous manner to summarize the responses of composition and structure to changes in three deposition process control variables: Q_{C2H2}, V_b, and ω_{Rot}. The key property trends within the studied parameter space can be summarized as follows:

- Film Ta/C atomic ratio increased with decreasing Q_{C2H2} only.

- Hydrogen concentration in the films increased with increasing Q_{C2H2} and decreased with increasing $|V_b|$. A statistically significant interaction term, Q_{C2H2} * V_b, indicated that the magnitude of the V_b effect on hydrogen concentration was dependent on the Q_{C2H2} level.

- Total film thickness increased with increasing Q_{C2H2} and decreased with increasing $|V_b|$.

- TaC crystallite size increased with decreasing Q_{C2H2}. Measurement precision limitations prevented conclusive determination of the V_b effect on crystallite size.

- Peak fits to Raman spectra confirmed an increase of Csp^3-H bonds with increasing Q_{C2H2} and the possibility of increased Csp^2 bond angle disorder with increasing Q_{C2H2} and $|V_b|$.

- The films had a lamellar structure on a nanometer scale. The layer periodicity depended on Q_{C2H2}, ω_{Rot}, and possibly V_b.

In addition to a refinement of process – property relationships for reactively sputtered TaC/a-C:H films, the results were compared with literature data for various MC/a-C:H films and interpreted with respect to physical mechanisms for simultaneously occurring PVD and PECVD. For example, the Ta incorporation in the film was dependent on sputtering conditions (PVD) whereas the film hydrogen level depended on the

composition of the plasma environment and energetic ion bombardment conditions (PECVD).

4.6   REFERENCES

1. G. L. Doll and B. K. Osborn: Engineering surfaces of precision steel components, in *44th Annual Technical Conference Proceedings*. (Society of Vaccum Coaters, Philadelphia, PA, Apr. 21-26 2001).

2. R. D. Evans, E. P. Cooke, C. R. Ribaudo, and G. L. Doll: Nanocomposite tribological coatings for rolling element bearings, in *Surface Engineering 2002 – Synthesis, Characterization and Applications*, edited by A. Kumar, W. J. Meng, Y. T. Cheng, J. S. Zabinski, G. L. Doll, and S. Veprek. (Mater. Res. Soc. Symp. **750**, Warrendale, PA, 2003), Y4.8 p. 407.

3. H. Sjostrom and V. Wikstrom: Diamond-like carbon coatings in rolling contacts. *Proc. Instn. Mech. Engrs. Part J* **215**, 545 (2001).

4. H. Dimigen and H. Hubsch: Applying low-friction wear-resistant thin solid films by physical vapour deposition. *Philips Tech. Review* **41**, 186 (1983).

5. H. Dimigen and H. Hubsch: Carbon-containing sliding layer. US Patent #4,525,417 (Jun. 25, 1985).

6. H. Dimigen, H. Hubsch, and R. Memming: Tribological and electrical properties of metal-containing hydrogenated carbon films. *Appl. Phys. Lett.* **50**, 1056 (1987).

7. E. Bergmann and J. Vogel: Tribological properties of metal/carbon coatings. *J. Vac. Sci. Tech. A* **4**, 2867 (1986).

8. E. Bergmann and J. Vogel: Influence of composition and process parameters on the internal stress of the carbides of tungsten, chromium, and titanium. *J. Vac. Sci. Tech. A* **5**, 70 (1987).

9. C. P. Klages and R. Memming: Microstructure and physical properties of metal-containing hydrogenated carbon films. *Mater. Sci. Forum* **52 & 53**, 609 (1989).

10. C. Benndorf, M. Grischke, H. Koeberle, R. Memming, A. Brauer, and F. Thieme: Identification of carbon and tantalum chemical states in metal-doped a-C:H films. *Surf. Coat. Tech.* **36**, 171 (1988).

11. W. van Duyn and B. van Lochem: Chemical and mechanical characterization of WC:H amorphous layers. *Thin Solid Films* **181**, 497 (1989).

12. M. Grischke, K. Bewilogua, and H. Dimigen: Preparation, properties and structure of metal containing amorphous hydrogenated carbon films. *Mater. Manuf. Process.* **8**, 407 (1993).

13. K. Bewilogua and H. Dimigen: Preparation of W-C:H coatings by reactive magnetron sputtering. *Surf. Coat. Tech.* **61**, 144 (1993).

14. H. Sjostrom, L. Hultman, J. E. Sundgren, and L. R. Wallenberg: Microstructure of amorphous C:H and metal-containing C:H films deposited on steel substrates. *Thin Solid Films* **232**, 169 (1993).

15. W. J. Meng, T. J. Curtis, L. E. Rehn, and P. M. Baldo: Plasma-assisted deposition and characterization of Ti-containing diamondlike carbon coatings. *J. Appl. Phys.* **83**, 6076 (1998).

16. W. J. Meng and B. A. Gillispie: Mechanical properties of Ti-containing and W-containing diamond-like carbon coatings. *J. Appl. Phys.* **84**, 4314 (1998).

17. A. A. Voevodin, J. P. O'Neill, and J. S. Zabinski: Tribological performance and tribochemistry of nanocrystalline WC/amorphous diamond-like carbon composites. *Thin Solid Films* **342**, 194 (1999).

18. K. I. Schiffmann, M. Fryda, G. Goerigk, R. Lauer, P. Hinze, and A. Bulack: Sizes and distances of metal clusters in Au-, Pt-, W- and Fe-containing diamond-like carbon hard coatings: a comparative study by small angle x-ray scattering, wide angle x-ray diffraction, transmission electron microscopy and scanning tunnelling microscopy. *Thin Solid Films* **347**, 60 (1999).

19. P. Villiger, Ch. Sprechter, and J. A. Peters: Parameter optimization of Ti-DLC coatings using statistically based methods. *Surf. Coat. Tech.* **116-119**, 585 (1999).

20. G. Hakansson, I. Petrov, and J. E. Sundgren: Growth of TaC thin films by reactive direct current magnetron sputtering: composition and structure. *J. Vac. Sci. Tech. A* **8**, 3769 (1990).

21. K. W. Gerstenberg and M. Grischke: Thermal gas evolution studies on a-C:H:Ta films. *J. Appl. Phys.* **69**, 736 (1991).

22. D. P. Palicki and A. Matthews: Recent developments in magnetron sputtering systems. *Finishing* (Nov. 1993) p. 36.

23. D. G. Teer: Magnetron sputter ion plating. US Patent #5,556,519 (Sep. 17, 1996).

24. P. V. Brande, S. Lucas, R. Winand, L. Renard, and A. Weymeersch: Study of the formation of a carbon layer on a sputtering target during magnetron-enhanced reactive sputtering. *Surf. Coat. Tech.* **61**, 151 (1993).

25. I. Safi: Recent aspects concerning DC reactive magnetron sputtering of thin films: a review. *Surf. Coat. Tech.* **127**, 203 (2000).

26. D. G. Montgomery: *Design and Analysis of Experiments*, 5th ed. (John Wiley & Sons, 2001).

27. A. C. Ferrari and J. Robertson: Interpretation of Raman spectra of disordered and amorphous carbon. *Phys. Rev. B* **61**, 14095 (2000).

28. G. R. Gruzalski and D. M. Zehner: Defect states in substoichiometric tantalum carbide. *Phys. Rev. B* **34**, 3841 (1986).

29. NIST X-ray Photoelectron Spectroscopy Database, NIST Standard Reference Database 20, Version 3.4 (Web Version), 2003.

30. A. A. Rempel and A. K. Sinelnichenko: X-ray photoelectron spectra of nonstoichiometric tantalum carbide. *Phys. Metals* **11**, 352 (1992).

31. J. C. Angus and F. Jansen: Dense "diamondlike" hydrocarbons as random covalent networks. *J. Vac. Sci. Tech. A* **6**, 1778 (1988).

32. H. P. Klug and L. E. Alexander: *X-ray diffraction procedures for polycrystalline and amorphous materials*, 2nd ed. (John Wiley & Sons, New York, 1974).

33. S. Logothetidis, E. I. Meletis, and G. Kirouklis: New approach in the monitoring and characterization of titanium nitride thin films. *J. Mater. Res.* **14,** 436 (1999) 436-441.

34. J. Robertson: Diamond-like amorphous carbon. *Mater. Sci. Eng. R* **37**, 129 (2002).

35. M. A. Tamor and W. C. Vassell: Raman "fingerprinting" of amorphous carbon films. *J. Appl. Phys.* **76**, 3823 (1994).

36. G. Adamopoulos, J. Robertson, N. A. Morrison, and C. Godet: Hydrogen content estimation of hydrogenated amorphous carbon by visible Raman spectroscopy. *J. Appl. Phys.* **96**, 6348 (2004).

37. D. Hofmann, H. Schuessler, K. Bewilogua, H. Hubsch, and J. Lemke: Plasma-booster-assisted hydrogenated W-C coatings. *Surf. Coat. Tech.* **73**, 137 (1995).

38. K. Bewilogua, C. V. Cooper, C. Specht, J. Schroder, R. Wittorf, and M. Grischke: Erratum to: "Effect of target material on deposition and properties of metal-containing DLC (Me-DLC) coatings". *Surf. Coat. Tech.* **132**, 275 (2000).

39. S. J. Park, K. R. Lee, D. H. Ko, and K. Y. Eun: Microstructure and mechanical properties of WC-C nanocomposite films. *Diam. Relat. Mater.* **11**, 1747 (2002).

40. M. Hans, R. Buchel, M. Grischke, R. Hobi, and M. Zach: High-volume PVD coating of precision components of large volumes at low process costs. *Surf. Coat. Tech.* **123**, 288 (2000).

41. V. Y. Kulikovsky, F. Fendrych, L. Jastrabik, and D. Chvostova: Study of formation and some properties of Ti-C:H films prepared by d.c. magnetron sputtering. *Surf. Coat. Tech.* **91**, 122 (1997).

42. B. Shi and W. J. Meng: Intrinsic stresses and mechanical properties of Ti-containing hydrocarbon coatings. *J. Appl. Phys.* **94**, 186 (2003).

43. W. Wagner, F. Rauch, and M. Grischke: Stoichiometry of a-C:H(Ta) films determined by means of RBS and the 15N technique. *Nuc. Inst. Meth. Phys. Res. B* **111**, 111 (1996).

44. W. J. Meng, E. I. Meletis, L. E. Rehn, and P. M. Baldo: Inductively coupled plasma assisted deposition and mechanical properties of metal-free and Ti-containing hydrocarbon coatings. *J. Appl. Phys.* **87**, 2840 (2000).

45. W. J. Meng, R. C. Tittsworth, and L. E. Rehn: Mechanical properties and microstructure of TiC/amorphous hydrocarbon nanocomposite coatings. *Thin Solid Films* **377**, 222 (2000).

46. W. J. Meng, R. C. Tittsworth, J. C. Jiang, B. Feng, D. M. Cao, K. Winkler, and V. Palshin: Ti atomic bonding environment in Ti-containing hydrocarbon coatings. *J. Appl. Phys.* **88**, 2415 (2000).

47. A. Czyzniewski: Deposition and some properties of nanocrystalline WC and nanocomposite WC/a-C:H coatings. *Thin Solid Films* **433**, 180 (2003).

48. C. Strondl, G. J. van der Kolk, T. Hurkmans, W. Fleischer, T. Trinh, N. M. Carvalho, and J. Th. M. de Hosson: Properties and characterization of multilayers of carbides and diamond-like carbon. *Surf. Coat. Tech.* **142**, 707 (2001).

49. T. Zehnder and J. Patscheider: Nanocomposite TiC/a-C:H hard coatings deposited by reactive PVD. *Surf. Coat. Tech.* **133**, 138 (2000).

50. T. Zehnder, P. Schwaller, F. Munnik, S. Mikhailov, and J. Patscheider: Nanostructural and mechanical properties of nanocomposite nc-TiC/a-C:H films deposited by reactive unbalanced magnetron sputtering. *J. Appl. Phys.* **95**, 4327 (2004).

51. C. Strondl, N. M. Carvalho, J. Th. M. De Hosson, and G. J. van der Kolk: Investigation on the formation of tungsten carbide in tungsten-containing diamond like carbon coatings. *Surf. Coat. Tech.* **162**, 288 (2003).

52. D. L. Smith: *Thin-Film Deposition: Principles and Practice* (McGraw Hill, Boston, 1995).

53. J. A. Venables, G. D. T. Spiller, and M. Hanbucken: Nucleation and growth of thin films. *Rep. Prog. Phys.* **47**, 399 (1984).

54. J. C. Angus and C. C. Hayman: Low-pressure, metastable growth of diamond and diamondlike phases. *Science* **241**, 913 (1988).

55. J. J. Cuomo, D. L. Pappas, J. Bruley, J. P. Doyle, and K. L. Saenger: Vapor deposition processes for amorphous carbon films with sp^3 fractions approaching diamond. *J. Appl. Phys.* **70**, 1706 (1991).

56. Y. Lifshitz, S. R. Kasi, J. W. Rabalais, and W. Eckstein: Subplantation model for film growth from hyperthermal species. *Phys. Rev. B* **41**, 10468 (1990).

57. J. Robertson: Deposition mechanisms for promoting sp^3 bonding in diamond-like carbon. *Diam. Relat. Mater.* **2**, 984 (1993).

58. J. Robertson: The deposition mechanism of diamond-like a-C and a-C:H. *Diam. Relat. Mater.* **3**, 361 (1994).

59. A. Grill, B. S. Meyerson, V. V. Patel, J. A. Reimer, and M. A. Petrich: Inhomogeneous carbon bonding in hydrogenated amorphous carbon films. *J. Appl. Phys.* **61**, 2874 (1987).

60. A. von Keudell, M. Meier, and C. Hopf: Growth mechanism of amorphous hydrogenated carbon. *Diam. Relat. Mater.* **11**, 969 (2002).

61. A. von Keudell, T. Schwarz-Selinger, and W. Jacob: Simultaneous interaction of methyl radicals and atomic hydrogen with amorphous hydrogenated carbon films. *J. Appl. Phys.* **89**, 2979 (2001).

62. J. F. Ziegler: *The Stopping and Range of Ions in Solids* (Pergammon, New York, 1985). www.srim.org.

63. J. C. Angus: Empirical categorization and naming of "diamond-like" carbon films. *Thin Solid Films* **142**, 145 (1986).

64. H. Windischmann: An intrinsic stress scaling law for polycrystalline thin films prepared by ion beam sputtering. *J. Appl. Phys.* **62**, 1800 (1987).

CHAPTER 5

TaC/a-C:H MECHANICAL PROPERTIES

5.1   INTRODUCTION

Nanocomposite metal carbide/amorphous hydrocarbon thin films (MC/a-C:H) have been used increasingly on precision steel components [1] to reduce friction and make surfaces resistant to adhesive and abrasive wear. One such application is to delay scuffing at the rib-roller end sliding contact in tapered roller bearings when the lubricant supply is interrupted [2].

The relationship between MC/a-C:H film hardness and wear resistance can be described by the Archard equation [3]:

$$V = \frac{k\,L\,x}{H} \qquad (5.1)$$

where V is the volume of material removed, L is the applied load, x is the sliding distance, H is the hardness of the worn surface, and k is a nondimensional wear constant. The Archard equation has been applied to estimate the scuffing protection achievable with MC/a-C:H thin film coatings at the rib-roller end sliding contact [2]. A key insight of this model is that wear resistance is proportional to the hardness of the wear surface. The Archard equation applies to sliding wear surfaces in general, but it is only meaningful for thin films that have adequate adhesion to the substrate. A wear-resistant film is not useful if it is removed from the substrate by delamination. Two mechanical properties can affect the adhesion of thin films in service: residual stress level and elastic modulus. High stress levels can greatly lessen film adhesion to the substrate. In addition, films must have a comparable or lower elastic modulus than the substrate to accommodate

surface deformation without fracture. Thus, hardness, elastic modulus, and film stress level all directly influence the ability of MC/a-C:H films to enhance the wear-resistance of steel rolling element bearing surfaces. An understanding of the relationships between film deposition process conditions and mechanical properties is needed to engineer surfaces that meet specific application requirements.

The relationships between deposition process parameters and MC/a-C:H film mechanical properties have been studied in one-factor-at-a-time experiments previously. Increases in film compressive stress level with increasing $|V_b|$ were observed in WC/a-C:H [4,5] and TiC/a-C:H [6] thin films. Less consistent trends have been observed in the dependency of compressive stress level on composition for MC/a-C:H films [7,8,9]. The achievable hardness and elastic modulus levels for MC/a-C:H have been reported most frequently in the literature. A common observation has been that the hardness and modulus values decrease with increasing carbon and hydrogen levels in the films (e.g., WC/a-C:H [7,9,10,11,12,13,14,15], TiC/a-C:H [13,14,16,17], and TaC/a-C:H [10,18]). It has not been possible thus far to broadly generalize the effect of substrate bias voltage on the hardness and modulus of MC/a-C:H thin films. Meng et al. [19] and Shi and Meng [6] observed different hardness and modulus trends as a function of V_b for TiC/a-C:H with a reactive sputtering system and a hybrid CVD/PVD system, respectively. Kulikovsky et al. [20] and Zehnder et al. [21] both observed increases in hardness with increasing $|V_b|$ in the TiC/a-C:H system within different process ranges. Strondl et al. [5] observed increases in hardness and modulus with increasing $|V_b|$ in the WC/a-C:H system, regardless of whether W or WC sputtering targets were used. A few observations of hardness dependence on multilayer periodicity were reported as well [22,23], with the

primary conclusion being that finer multilayers and a more homogeneous structure result in the highest hardnesses. The MC/a-C:H literature is thus far lacking discussions about the possible atomistic growth mechanisms relating mechanical properties to deposition conditions.

The TaC/a-C:H films examined herein were the subject of Chapter 4, in which correlations between process settings and film structure and chemical composition were identified. As an extension of that initial work, the mechanical properties of the films were measured and analyzed. Nanoindentation was performed to evaluate hardness and elastic indentation modulus, and measurements of wafer curvature combined with Stoney's equation were used to evaluate film compressive stress. In the structure and chemical composition study (Chapter 4), the statistical design of experiments gave an understanding of film property trends attributable to changes in d.c. bias voltage level (V_b), acetylene flow rate (Q_{C2H2}), and substrate rotation rate (ω_{Rot}) during deposition. Insights into film growth mechanisms were obtained by isolating film composition and structure responses with respect to deposition parameters. The designed deposition experiments also enabled the evaluation of the effect of Q_{C2H2}, V_b, and ω_{Rot} on the film stress, hardness, and elastic modulus of TaC/a-C:H films. With that knowledge, an attempt is made to qualitatively rationalize the observed mechanical property development with atomic-level growth phenomena.

5.2   EXPERIMENTAL

Deposition process details have been described in Chapter 4 for the TaC/a-C:H films. To review, the films were deposited in a closed-field unbalanced magnetron sputtering

system, equipped with two diametrically opposite Ta sputtering targets and a substrate carousel set up for single-axis rotation. Substrates were mounted on the carousel in a fixed position approximately 24 cm from the target faces. A 2^3 factorial experiment was used to evaluate the effects of the flow rate of acetylene into the chamber (Q_{C2H2}), applied direct current substrate bias (V_b), and substrate carousel rotation rate (ω_{Rot}) on film properties. Other process settings such as flow rate of argon into the chamber, field coil current, Ta sputtering target power level, chamber base pressure, plasma cleaning sequence, and Ta interlayer deposition sequence were held constant during each film deposition process. Chamber pressure during the TaC/a-C:H layer depositions was 0.1-0.3 Pa. Substrates were not intentionally heated, and the maximum substrate temperature during deposition was ~130-150°C as measured with surface contact thermometers mounted to the substrate bracket. The film architecture, including the plasma etch step and interlayer deposition, was identical for each test film. The film deposition system was equipped with process control hardware and software to ensure repeatable and accurate process sequences and setpoints. Si wafer substrates ($\langle 001 \rangle$) provided a reproducible surface for film growth.

The parameter space for experiments was carefully selected to ensure plasma stability yet demonstrate the sensitivity of film mechanical properties on the deposition process conditions. The set point ranges for variable factors were Q_{C2H2} = 45 to 65 sccm, V_b = -150 to -50 V, and ω_{Rot} = 2 to 3 rpm. The numerical process factor setpoints may not produce identical results in different deposition systems. However, it is the intention of this work to demonstrate mechanical property trends as a function of changes in process parameters that are common to typical reactive sputtering systems. Mathematical

confidence in directional trends was obtained by fitting empirical models to the data with standard multiple linear regression techniques [24] using the JMP statistical analysis software package (SAS, Inc). "Higher" V_b levels are increasingly cathodic and therefore negative in the mathematical analyses. Therefore, the bias voltage magnitude $|V_b|$ is invoked throughout this chapter to maintain consistency between the empirical model results and the concept of "increasing" bias level.

Residual compressive stress measurements were performed by measuring wafer curvature using a MicroXAM Phase Shift optical profilometer, and inserting those values into the Stoney equation [25]:

$$\sigma_f = \frac{1}{6R} \frac{Y_s d_s^2}{(1 - \nu_s) d_f} \qquad (5.2)$$

where σ_f is the film stress, R is the wafer radius of curvature, Y_s is the substrate elastic modulus, ν_s is the substrate Poisson's ratio, and d_s and d_f are the substrate and film thicknesses, respectively. A value of 181 GPa was used for the silicon ($\langle 001 \rangle$) wafer biaxial elastic modulus, $Y_s/(1-\nu_s)$ [26]. A scanning electron microscope was used to measure the film thickness in cross-section at a fractured edge. The compressive stress values are shown as positive values on the plots. The error bars in the plots represent 95% confidence intervals about the mean of each measurement.

Nanoindentation hardness (H) and elastic indentation modulus ($Y_{ind} = Y_f/(1-\nu_f^2)$) measurements were performed using a Nanotest 600 instrument with a Berkovich diamond indenter (Micro Materials LTD). Depth calibrations were performed using a fused silica optical flat (8.8 GPa) prior to testing. Hardness and reduced elastic modulus were derived using the method of Oliver and Pharr [27] to analyze load-displacement

curves for each sample. Each film sample on Si was measured at four indentation loads (100, 50, 25, and 10 mN) ten times each, but only the data from the 25 mN load level are reported herein. Replicate measurements were normally distributed about the mean, and the error bars in the plots represent 95% confidence intervals about the mean. Nanoindentation measurements using the 25 mN load level resulted in maximum indentation depths between ~270-400 nm, or about 10-20% of the film thickness.

5.3   RESULTS

Mechanical property data for each film are shown in Table 5-1. An advantage of using factorial designed experiments is that the effects of multiple factors may be analyzed mathematically with a minimum number of experiments. However, it can be difficult to interpret data from multivariate experiments on a two-dimensional plot. Statistically significant directional trends are presented as two-dimensional projections of the data with respect to one factor (x-axis) at a time in this Chapter. To aid the reader in understanding all of the deposition parameter settings for each datum, each point in the plots is labeled with a letter corresponding to the experiment in Table 5-1. Films B and J were exact replicates to show deposition process variation and to increase statistical confidence in the results. Table 5-2 shows the multiple linear regression models that were fitted to the data. None of the measured mechanical properties was statistically dependent on ω_{Rot} or an interaction term (i.e., dependency on a product of factors) within the parameter space studied.

Table 5-1. TaC/a-C:H film identification and results. Q_{C2H2}, V_b, and ω_{Rot} refer to the acetylene gas flow rate, applied d.c. bias voltage, and substrate carousel rotation rate, respectively.

Film ID	Q_{C2H2} (sccm)	V_b (V)	ω_{Rot} (rpm)	Intrinsic Compressive Stress (GPa)	Hardness (GPa)	Indentation Modulus (GPa)
A	45	-100	2.5	1.23	18.4	212.2
B*	55	-100	2.5	1.04	15.3	173.2
C	65	-100	2.5	0.74	12.7	147.3
D	45	-150	3.0	1.37	19.7	212.7
E	65	-150	2.0	1.31	16.1	176.8
F	45	-150	2.0	1.35	20.7	220.4
G	65	-50	2.0	0.43	9.3	109.9
H	45	-50	2.0	0.52	12.9	164.6
I	65	-50	3.0	0.69	10.3	121.6
J*	55	-100	2.5	1.31	15.6	177.8
K	65	-150	3.0	1.79	16.7	179.0
L	45	-50	3.0	0.70	13.8	173.2

* Films B and J are replicates

Table 5-2. Multiple linear regression models for mechanical property observations. Non-significant terms were left blank in the table. The t-test p-value is listed below each term coefficient in parentheses.

Model Terms →	Intercept	$\left(\dfrac{Q_{C2H2} - 55}{10} \right)$	$\left(\dfrac{V_b - (-100)}{50} \right)$	Whole Model $R^2_{Adj.}$
Intrinsic Compressive Stress (GPa)	1.041	-	-0.435 (0.0001)	0.77
Hardness (GPa)	15.12	-2.034 (<0.0001)	-3.358 (<0.0001)	0.96
Indentation Modulus (GPa)	172.39	-24.837 (<0.0001)	-27.459 (<0.0001)	0.94

5.3.1 Compressive Stress

Compressive stress σ_f increased as $|V_b|$ increased as shown in Figure 5.1. No statistically significant trends were observed between stress and Q_{C2H2} or ω_{Rot}. Thus, σ_f was statistically independent of the TaC volume fraction within the studied parameter space. The compressive stress of TaC/a-C:H was on the order of a few GPa, which is consistent with previously reported ranges for WC/a-C:H [4,5] and TiC/a-C:H [6].

Lower σ_f levels, compared to those in tetrahedrally-bonded amorphous carbon that can exceed 10 GPa [28], make MC/a-C:H films more useful as tribological coatings on steel components. The total residual stress level in the film is typically attributed to a combination of intrinsic ("grown-in") and extrinsic (thermal mismatch) stresses. In this case, the intrinsic stresses are believed to dominate because the calculated thermal mismatch strain was about one order of magnitude lower than the strain values determined from the measured σ_f levels. This was true whether a coefficient of thermal expansion for TiC/a-C:H ($\sim$5.7 x 10^{-6} K^{-1} [29]), TaC (6.3 x 10^{-6} K^{-1} [30]), or Ta (6.5 x 10^{-6} K^{-1} [30]) was used in the calculations. The Ta interlayer was less than $\sim$25% of the total film thickness and deposited identically for all of the test films, so relative differences in σ_f among the films are attributed to differences in the thicker TaC/a-C:H top layer only.
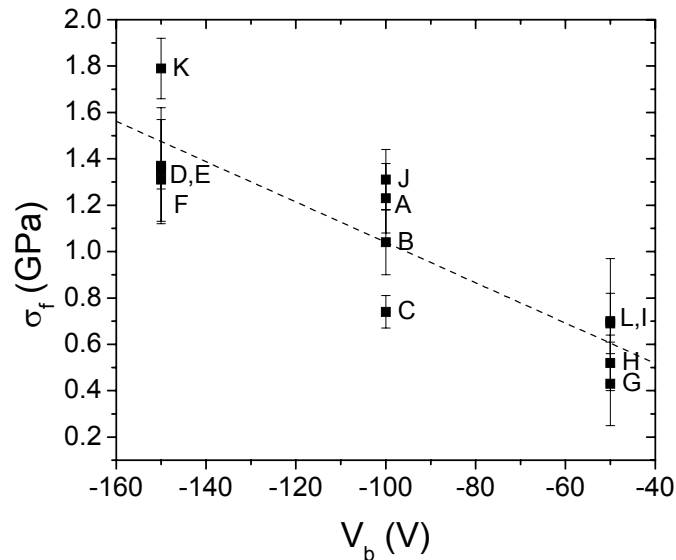
Figure 5.1. Measured film compressive stress as a function of V_b. The error bars indicate 95% confidence intervals on the mean.

5.3.2 Hardness and Elastic Modulus

Hardness H and elastic indentation modulus Y_{ind} varied as a function of both V_b and Q_{C2H2} as shown in Figures 5.2 and 5.3, respectively. The H/Y_{ind} ratio was consistently between 0.08-0.09 within the studied deposition parameter space. Tsui et al. [31] reported results for monolithic aluminum that suggested a surface in compression can produce artificially high hardness results with nanoindentation. This observation was attributed to pile-up around the indenter during the indentation cycle that underestimated the contact area of the diamond indenter. Pile-up was not apparent in SEM images of indents from the TaC/a-C:H films as shown in Figure 5.4. Furthermore, Cheng and Cheng [32] suggested that the Oliver and Pharr analysis method is generally appropriate for highly elastic films with a high yield stress to elastic modulus ratio, such as carbides, nitrides, and diamond-like amorphous carbon.
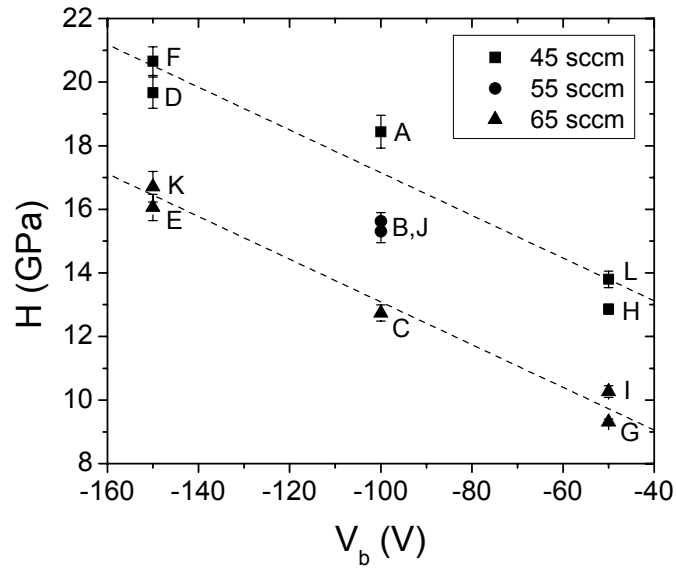
Figure 5.2. Nanoindentation hardness as a function of V_b and Q_{C2H2}. Data were acquired using the 25 mN load level. Guide lines are drawn through the data for Q_{C2H2} = 45 and 65 sccm.
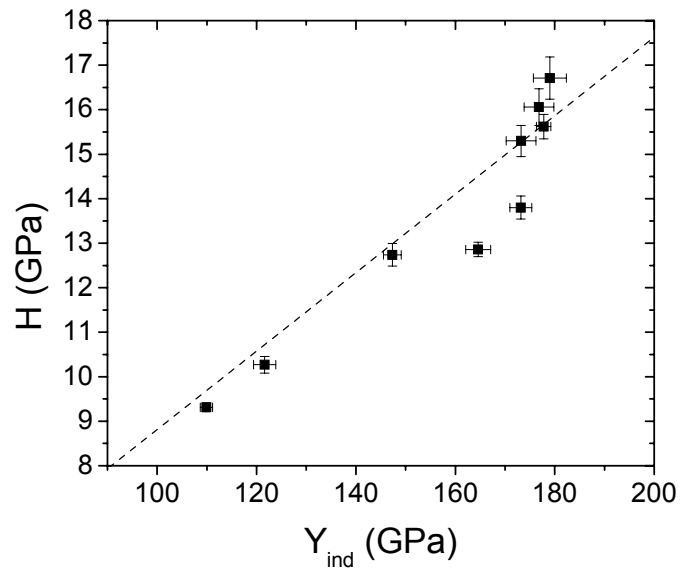
Figure 5.3. Hardness versus elastic indentation modulus for the TaC/a-C:H films.

(a)

(b)
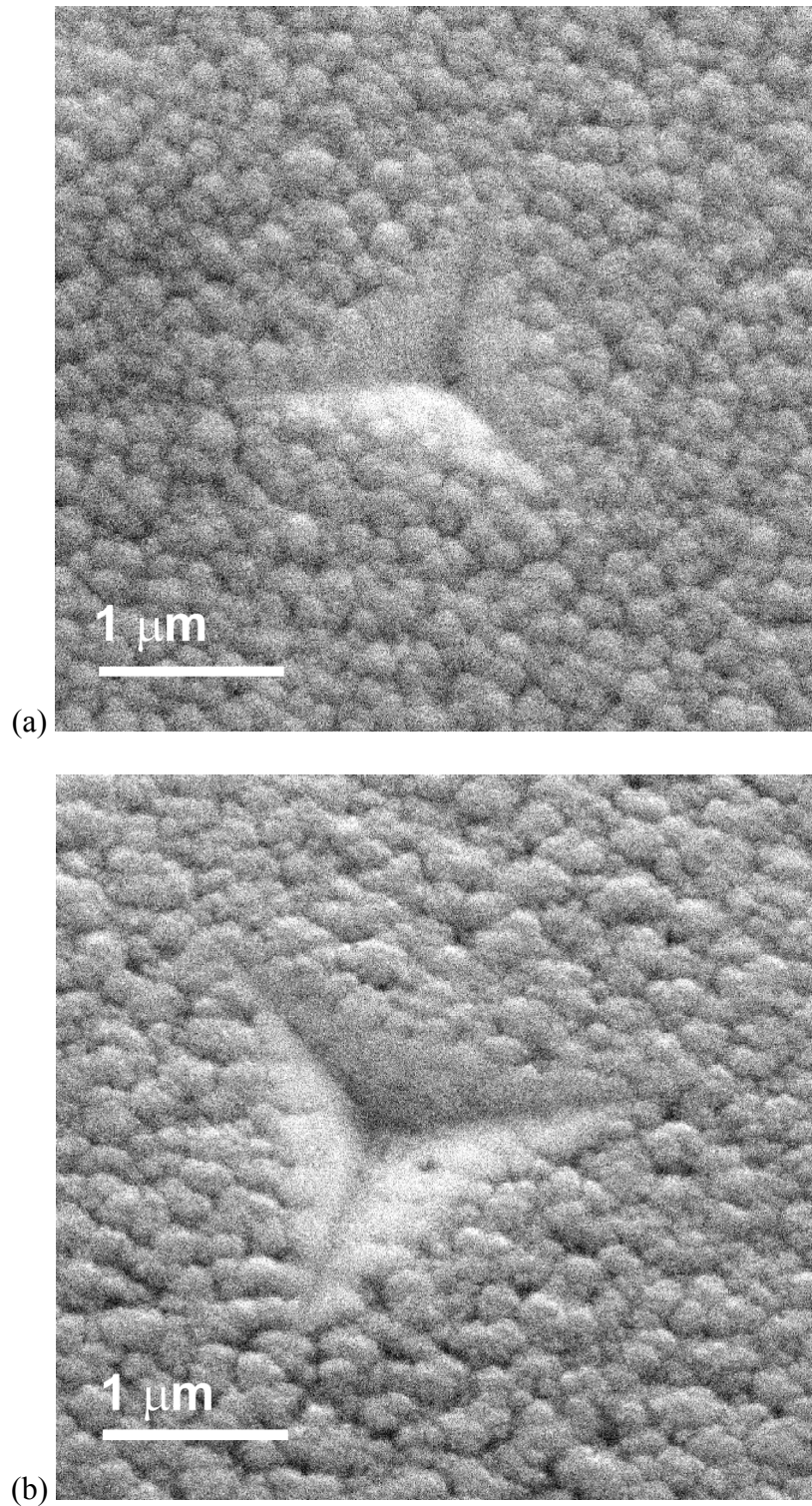
Figure 5.4. Images of indents from the TaC/a-C:H films (a) *D* with V_b = -150 V and (b) *L* with V_b = -50 V.

5.4 DISCUSSION

Stress, hardness, and elastic indentation modulus results for the TaC/a-C:H films were linear within the studied parameter space. The experimental design enabled a ranking of deposition process effects on mechanical properties. An attempt to mechanistically explain the observed relationships is made in this section.

5.4.1 Stress Dependency on V_b

5.4.1.1 Development of Intrinsic Stress

A fundamental assumption in thin film mechanical property analyses is that the linear elastic Hooke's law model applies:

$$\sigma_f = \left(\frac{Y_f}{(1 - \upsilon_f)} \right) \varepsilon_f \qquad (5.3)$$

where σ_f is the biaxial compressive stress level in the film, $Y_f/(1-\upsilon_f)$ is the film biaxial modulus (Y_f is the elastic modulus and υ_f is Poisson's ratio), and ε_f is the biaxial strain in the film. The TaC/a-C:H film data indicated that both Y_f and σ_f were dependent on V_b.

Intrinsic compressive stress development in thin films has been described using "ion peening" concepts [33,34]. These models attribute the development of biaxial film strain to lattice distortion that is created by subsurface collision cascades resulting from hyperthermal atom bombardment of the surface. Knock-on collisions in the cascade force subsurface atoms into positions that are not energetically favorable relative to the surrounding lattice/network. This mechanism was shown schematically for crystalline films [35], and is reasonable in concept for amorphous materials with preferred directional covalent bond configurations. Subsurface damage is quenched-in during growth by the comparatively lower bulk film temperature leading to local bond distortion

and an increase in strain energy. The sum of all the strained regions produces a macroscopic stress state.

It has been reported that σ_f was dependent on the square root of the bombarding ion energy in metal and metallic compounds [33], as well as amorphous hydrocarbon [36] thin films. Windischmann's model [33] provided a derivation of this relationship using analytical "forward sputtering" expressions. Davis [37] expanded the Windischmann model by explaining data that exhibit a maximum in σ_f with increasing ion bombardment energy (E_i) in terms of a "thermal spike" model. The decrease in σ_f at the highest bombarding energy levels was attributed to annealing/relaxation effects in the film structure. The σ_f data in Figure 5.1 showed a monotonic increase with increasing $|V_b|$, and therefore appeared to fall within a low energy bombardment range as described by the Windischmann model, and do not require the thermal spike considerations of Davis.

Inert gas impurities in materials have also been related to the stress levels in films. In bulk diamond studies, Anthony [38] proposed that the presence of impurity concentration gradients may deform the lattice, creating strains that lead to a finite compressive stress state during diamond growth. The strain ε_i imparted to the film was estimated to be proportional to the product of the impurity concentration (at.%) and a constant with a value > 1 that depends on the impurity type and size. The Chapter 4 analysis shows that Ar was incorporated in the TaC/a-C:H films during growth (up to 2 at.% at V_b = -150 V) with the concentration monotonically increasing with $|V_b|$. As such, the concentration of Ar in the TaC/a-C:H films was directly proportional with σ_f in the studied parameter space.

A generalized ion peening model was presented by Smith [39]. In this model, the development of bond distortion strains was attributed to the creation of interstitials in the collision cascade. This approach incorporated the essence of both Windischmann (forward sputtering) and Anthony (impurity interstitials). That is, the atoms within the film structure are forced into volumes that are not energetically favorable, thus generating local "lattice" strains in the surrounding material. The strains associated with these point defects accumulate to produce macroscopic film stress. The Smith model form is as follows:

$$\sigma_f = \left(\frac{Y_f}{(1-\nu_f)}\right)\left(\frac{BJ_iN_i}{J_r}\right) \qquad (5.4)$$

where B is a proportionality constant, J_i is the bombarding ion flux, J_r is the deposition flux, and N_i is the number of interstitials produced per bombarding ion [39]. N_i may be approximated by assuming that Frenkel-type imperfections form within the subsurface collision cascade and sputtering is negligible, such that the number of vacancies equals the number of interstitials ($N_v \sim N_i$). N_v may be approximated analytically using a modified Kinchen-Pease formula for high energy bombardment. For the conditions of thin film growth, Smith [39] recommended the use of TRIM (Transport and Range of Ions in Matter) Monte-Carlo simulations to estimate $N_v \sim N_i$. A similar model form for stress development by the creation of Frenkel imperfections in a-C films was proposed by Zhang et al. [40] and verified using molecular dynamics simulations.

Simulations of thin film growth phenomena with the TRIM algorithm require many assumptions which were summarized in a review by Jacob [41]. For example, the binary collision approximation is assumed and dynamic interactions between moving atoms are not simulated. Thermal annealing of defects and dynamic replacement collisions to fill

subsurface vacancies are not taken into account. TRIM assumes that the surface is amorphous, which is appropriate for the a-C:H phase but not accurate for cubic TaC (NaCl crystal structure). In spite of these limitations, simulation of the collision cascade and statistical quantification of the resulting damage make TRIM an excellent tool for comparing the gross effects of bombarding ion impact with model surfaces. TRIM simulations are used in the next section to estimate the relative extent of vacancy/interstitial creation in the surface as a function of E_i and the surface type. Although it is known that bombarding ions are rapidly neutralized upon approaching real surfaces, atomic species that bombard and implant in the model surfaces are referred to in these discussions as "ions" for simplicity.

5.4.1.2 TRIM Simulations of Damage during TaC/a-C:H Growth

TaC/a-C:H growth conditions were simulated with TRIM [42] to explore the relationship between N_i and V_b and determine if the intrinsic stress model in Equation 5.4 appropriately describes the observations of Figure 5.1. If a collisionless sheath is assumed at the low processing pressures of 0.1-0.3 Pa, the maximum ion energy is approximated as E_i (eV) $= e|V_b| + eV_p$ for singly ionized bombarding ions where e is the charge quantity and V_p is the plasma potential in volts [39]. It was assumed that $V_p \sim 20$ V, and was independent of V_b, as observed in other similar deposition environments [6]. Because Ar^+ and C^+ ions have an implantation depth of ~2 nm at the energies relevant to TaC/a-C:H deposition, bombardment of single-phase TaC or a-C:H surfaces was simulated. The model surfaces were defined as stoichiometric TaC with a density of 14.5 g/cm^3 and $C_{0.55}H_{0.45}$ with an estimated density of 1.5 g/cm^3. The default values for the displacement energies E_d (28 eV for C and 10 eV for H) from the TRIM software were

used in this study for all atoms in both the a-C:H and TaC phases. In a-C:H studies, Jacob [41] used the values of 25 eV and 2.5 eV for C and H, respectively. All general conclusions from the present simulations were consistent with results obtained after repeating the simulations using the Jacob E_d values.

Bombardment of the model a-C:H and TaC surfaces by Ar^+, C^+, and H^+ ions was simulated for E_i = 30-170 eV. The binary collision approximation is not accurate for E_i levels less than ~30 eV. Simulation results near this lower E_i limit are important to show the effects of low energy implantation from fragments of molecular ions (e.g., C from $C_2H_2^+$) that receive only a fraction of the original kinetic energy upon impact and dissociation [43]. Because $C_xH_y^+$ ions are prevalent in C_2H_2-containing plasmas, it is likely that individual C atoms implant with lower energies on average than Ar^+. The TRIM output gave a distribution of vacancies/ion/depth for each simulation, so those data were numerically integrated to get an average N_v (vacancies/ion) for each bombardment scenario. The reported TRIM data were calculated from distributions of 10,000 bombarding ions.

TRIM simulations revealed that Ar^+ bombardment created mostly C vacancies in the model a-C:H with the significant creation of H vacancies only at E_i greater than 110 eV. C^+ bombardment displaced both C and H to create vacancies in the model a-C:H, while H^+ bombardment produced only H vacancies with nominally no C vacancy creation. Bombarding Ar^+ and C^+ created about the same amount of C vacancies/ion across the energy range. However, Ar^+ created more C vacancies/ion at higher E_i than C^+. Furthermore, the relationship between N_v (~ N_i) and E_i (~ $|V_b|$) for Ar^+ and C^+ bombardment was linear as shown in Figure 5.5(a).

Simulations of Ar^+, C^+, and H^+ bombardment of the model TaC surface resulted in several key observations. Ar^+ bombardment created both Ta and C vacancies, with N_v increasing linearly with increasing E_i. C^+ bombardment likewise created C vacancies, but could only create significant Ta vacancies at E_i greater than 150 eV. H^+ bombardment could not create Ta or C vacancies within the studied E_i range. Ar^+ and C^+ bombardment created approximately the same number of C vacancies in the TaC, and both displayed a linear relationship between N_v and E_i. A comparison between the C vacancies/ion created by bombarding Ar^+ in both a-C:H and TaC model surfaces is shown in Figure 5.5(b). For the same E_i level, energetic Ar^+ bombardment created more C vacancies/ion in the a-C:H phase than in the TaC phase. A summary of the subsurface damage results for each bombarding ion type from the TRIM simulations is presented in Table 5-3.
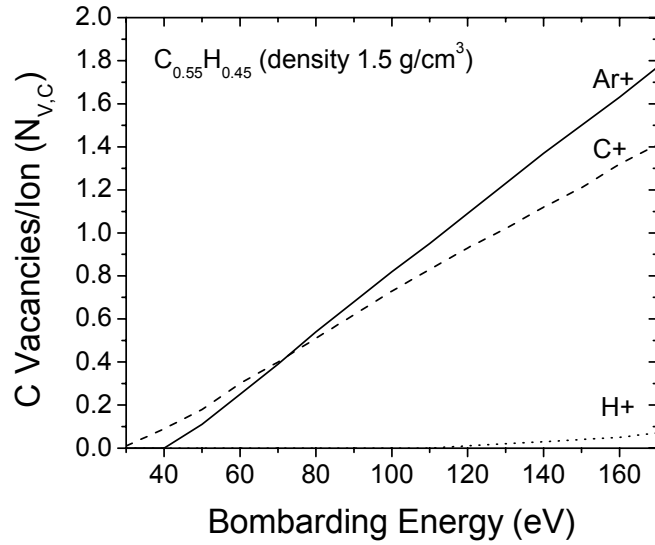
(a)
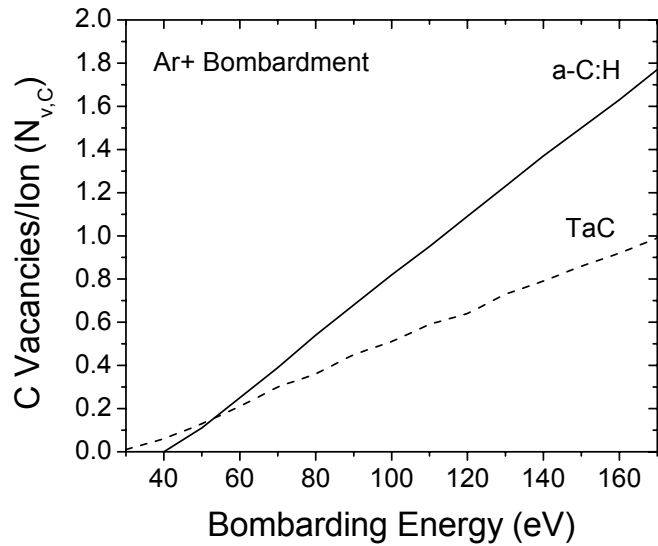
(b)

Figure 5.5. (a) Number of C vacancies/ion created in the model a-C:H surface as a function of bombarding energy for Ar^+, C^+, and H^+ impingement. (b) Number of C vacancies/ion as a function of Ar^+ bombarding energy for a-C:H and TaC model surfaces.

Table 5-3. Summary of vacancy creation in model a-C:H and TaC surfaces by bombarding Ar^+, C^+, and H^+ from TRIM simulations. A "yes" indication is given if the average vacancies/ion exceeded a value of 0.1. The bombarding energy that satisfies that criterion is shown in parenthesis. A "no" indication is given if the criterion was not met over the total simulated range of 30-170 eV.

Model Surface →	a-C:H ($C_{0.55}H_{0.45}$)		TaC	
Displaced Atom →	C	H	C	Ta
Ar+	yes (> 50 eV)	yes (> 110 eV)	yes (> 60 eV)	yes (> 60 eV)
C+	yes (> 40 eV)	yes (> 50 eV)	yes (> 50 eV)	yes (> 150 eV)
H+	no	yes (> 30 eV)	no	no

5.4.1.3 Validation of the Stress Model for TaC/a-C:H Films

It is assumed that differences in J_i and J_r among the test films were negligible in the studied parameter space, which is not unreasonable because the substrate current density levels were approximately the same for all of the test film depositions and the resulting film thicknesses were on the same order of magnitude. Therefore, a linear relationship would be expected for σ_f and the product of Y and N_i if the Equation 5.4 model accurately describes the mechanism for compressive stress generation in the TaC/a-C:H films. Given that $Y_f/(1-\nu_f)$ is equivalent to $Y_{ind}(1+\nu_f)$, and N_i is proportional to E_i (Figure 5.5(a)), a plot of σ_f versus $Y_{ind}*E_i$ represents the form of Equation 5.4 if ν_f is constant for the films tested. Data were plotted in this format in Figure 5.6, and the linearity of the data suggests some agreement with the form of Equation 5.4. However, it is noteworthy that a plot of σ_f versus $Y_{ind}*E_i^{1/2}$ was also linear. Although a marginally better R^2 correlation

statistic was found for the $Y_{ind}*E_i$ dependency, it is easy to see how an agreement

between σ_f and $Y_{ind}*E_i^{1/2}$ could be deduced [33,36] within a bombarding energy range of

a few hundred eV.
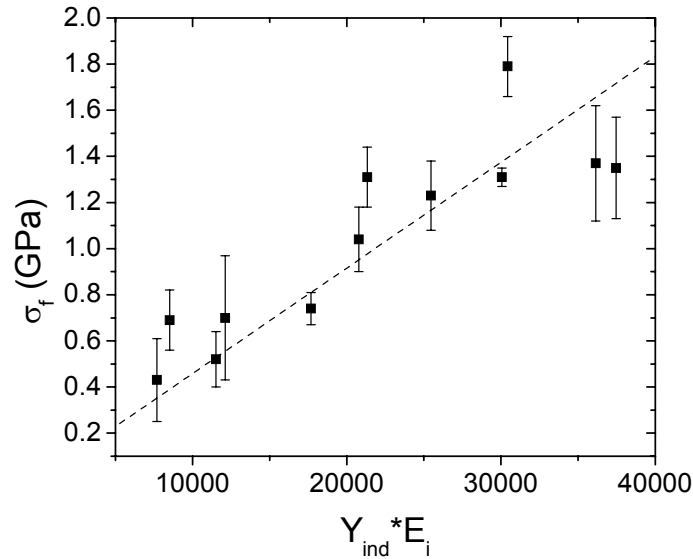
Figure 5.6. Film compressive stress level as a function of the indentation modulus times the estimated maximum bombarding ion energy for the TaC/a-C:H deposition experiments. This linear relationship suggests some agreement between the Equation 5.4 model and the stress state in the TaC/a-C:H films.

Although the Smith model (Equation 5.4) did not explicitly account for two-phase

composites, the overall form of the model appears to be consistent with the data (Figure

5.6). If the model mechanism is correct, the bond distortion strains must be located in at

least one or possibly both phases of the TaC/a-C:H composite. It is suggested by the

present work that the local distortion strains are accommodated by the continuous C-

skeleton in the a-C:H matrix, not the dispersed TaC phase. For example, the TRIM

simulations indicated that as the Ar^+ bombardment energy increased, the number of C

interstitials created in the model a-C:H surface increased linearly in the energy interval

examined, which was consistent with the trend between σ_f and V_b. The same simulations suggested that more C vacancies are created in a-C:H than in TaC for the same Ar^+ bombardment energy. It has been shown in Chapter 4 for the TaC/a-C:H films that V_b influenced the a-C:H matrix structure by affecting the hydrogen content and Raman scattering (G-peak width) data, whereas no evidence has been found that the stoichiometry of the TaC phase was affected by V_b. Since it is generally accepted that dislocations cannot exist in suspended nanometer-scale crystallites [44], it is speculated that interstitial point defects are not stable as well. Thus, any volumetric strain distortion that might occur within the TaC phase under bombardment is likely to be annealed out during growth. In addition to this reasoning, the concept that bond distortion strains can be accommodated by "single-phase" amorphous solids has been applied elsewhere [37,45] to explain intrinsic stress states in thin films.

Additional evidence about the location of distortion strains in the TaC/a-C:H composites can be inferred from the elastic modulus data. For example, Meng and Gillispie [13] interpreted reactively sputtered TiC/a-C:H thin film mechanical property results using macromechanical bounds developed for composites. The Paul upper and lower bounds on the elastic modulus of two-phase composites were applied [46]:

$$\frac{1}{\left((1-f)/Y_1\right)+\left(f/Y_2\right)} \leq Y \leq (1-f)Y_1 + fY_2 \qquad (5.5)$$

where Y_1 is the elastic modulus of the matrix material, Y_2 is the elastic modulus of the dispersed material, and f is the volume fraction of dispersed material. These bounds were derived by assuming that different stress-strain distributions exist within the composite structure. The upper bound assumes that the matrix and dispersed phases have the same strain level while the lower bound assumes an equal stress state for both constituent

phases. Despite the uncertainties in this approach, Meng and Gillispie were able to determine that the TiC/a-C:H indentation modulus more closely tracked the lower bound than the upper bound. They suggested that a similar stress state must therefore exist in the TiC crystallites and the a-C:H matrix. Those calculations were reproduced in the present research for the TaC/a-C:H data, using the same calculation approach and assumptions as Meng and Gillispie with the following properties for B1-TaC: $Y \sim 550$ GPa and $v \sim 0.21$ [47]. The TaC/a-C:H indentation modulus data likewise tracked evenly or fell below the Paul lower bound. This general agreement with the Meng and Gillispie data suggests that the constituent phases of the TaC/a-C:H composites also have equal stress levels but differing local strain levels. Assuming that the stress levels in each phase are equal, much more strain is expected for the a-C:H matrix phase ($Y_{ind} \sim$ 80-200 GPa) than the TaC phase ($Y_{ind} \sim 575$ GPa). Therefore, any grown-in bond distortion strains most likely are located in the a-C:H matrix rather than the crystalline TaC dispersed phase.

5.4.2 Hardness and Elastic Modulus Dependency on V_b and Q_{C2H2}

Like the film stress, the TaC/a-C:H film hardness and elastic modulus were most significantly affected by V_b within the studied parameter space. However, the hardness and elastic modulus were also found to depend on Q_{C2H2} in a second statistically significant relationship that was not present for the film stress.

5.4.2.1 V_b Effects

In the previous section, the linear dependency of σ_f on V_b for the TaC/a-C:H films was attributed to the linear relationship between the Ar$^+$ ion bombardment energy and the

extent of subsurface collision cascade damage to the C-skeleton in the a-C:H matrix (i.e., via interstitial creation). It was hypothesized that the overall compressive stress state of the films could be attributed to quenched-in bond distortion strain within the a-C:H matrix phase. Similarly, it is hypothesized that the dependency of hardness and modulus on V_b is attributable to the structural and chemical configuration of the a-C:H matrix. For example, the film hardness versus the measured film hydrogen concentration is shown in Figure 5.7. The films with the highest hardness had the lowest hydrogen content.
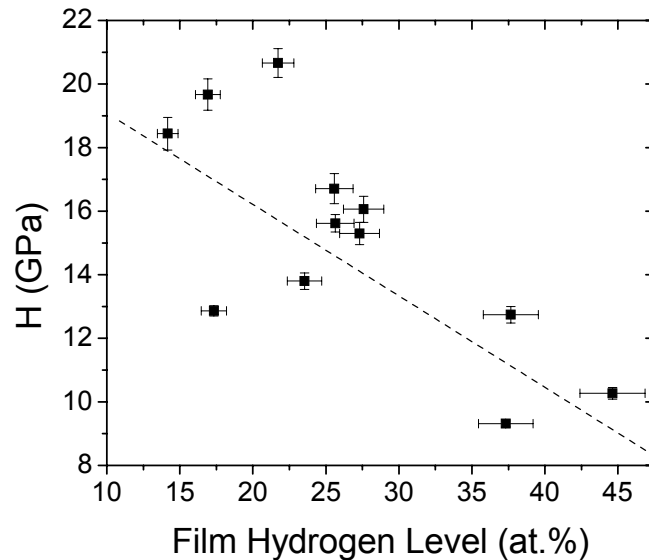
Figure 5.7. Hardness versus hydrogen concentration in the films (at.%).

Angus and Jansen [48] modeled the structure of a-C:H films by applying random covalent network concepts of Phillips [49] and Thorpe [50]. A random covalent network is completely constrained when the number of bond length and angle constraints per atom equals the number of mechanical degrees of freedom. The average number of constraints

per atom in a network can be quantified in terms of the mean nearest-neighbor coordination, m. Thorpe demonstrated that a percolation threshold for network rigidity exists at $m = 2.4$ and that m in excess of that value results in an over constrained and increasingly rigid network [50]. Angus and Jansen recognized that hydrogen does not contribute to network rigidity because it forms monovalent bonds to the carbon atoms that comprise the network "skeleton" [48]. They also found that the percolation threshold for rigidity of the C-skeleton occurs at $m_c = 2.4$ for a network containing fully dispersed Csp^3, Csp^2, and H. Thus, the general principles of random covalent networks are applicable to describe the rigidity of the C-skeleton within the a-C:H phase.

Robertson [51] extended the random covalent network analyses for a-C:H in the following ways: (i) by adapting the zero-frequency modes calculation of Thorpe [50] for a-C:H, (ii) by showing that the presence of graphitic clusters in a-C:H does not contribute to overall network rigidity, and (iii) by applying the analysis of He and Thorpe [52] to suggest that the extent of network over-constraint ($m_c > 2.4$) in a-C:H is related to the elastic modulus of the network. Robertson also proposed the following a-C:H structure trajectory with increasing $|V_b|$ for films deposited by plasma enhanced chemical vapor deposition [51]. The a-C:H network is "floppy" at $|V_b| < 100$ V with a high fraction of =CH_2 content. As $|V_b|$ is increased, the hydrogen content decreases and more $\equiv$CH and =C= groups are present in the network until graphitic clustering prevails at high $|V_b|$ levels (> 200 V).

Many of the concepts from the random covalent network analysis of a-C:H are applicable to the TaC/a-C:H films. As $|V_b|$ increases, the amount of hydrogen in the TaC/a-C:H film decreases (Chapter 4). Increasing $|V_b|$ presumably brings about a slight

increase in m_c for the a-C:H phase by two related mechanisms: (i) hydrogen abstraction from the carbon skeleton resulting in dangling bond formation and subsequent cross-linking [53], and (ii) carbon interstitial formation due to knock-on collisions initiated by bombarding ions such as Ar^+. The increase of m_c with increasing $|V_b|$ would result in a more rigid, possibly over-constrained network that gives an elastic modulus Y according to [43,52]:

$$Y = k(m_c - 2.4)^{1.5} \qquad (5.6)$$

where k is a constant and m_c is greater than 2.4. As mentioned previously, the monotonic increase of σ_f with $|V_b|$ for the TaC/a-C:H films suggests that the high bias levels which bring about more extensive graphitic clustering was not reached in these experiments.

A common link between the observed increases in σ_f, H, and Y with increasing $|V_b|$ in the TaC/a-C:H films is the idea that hyperthermal ion bombardment during growth may cause increased m_c levels to the point of over-constraint thus producing a rigid network with significant strain distortion. The principles of the Smith stress analysis (Equation 5.4) and the random covalent network model of the a-C:H phase are connected by this theme, and the experimental data appear to be as well. If these mechanistic hypotheses are correct, then both physical (knock-on damage by momentum transfer) and chemical (hydrogen abstraction and cross-linking reactions) processes in the a-C:H matrix phase during film growth are jointly responsible for determining mechanical properties.

The hardness and modulus of physical vapor deposited thin films have been shown to depend on the microstructure or "zone-type" of the film, which can be affected by V_b under certain processing conditions [54]. Fracture cross-sections for each of the TaC/a-C:H test films were examined using scanning electron microscopy and the

microstructures were both dense. These observations support the hypothesis that hardness and modulus differences as a function of V_b are attributable to atomic-level differences in the a-C:H structure, rather than macroscopic film morphology.

5.4.2.2 Q_{C2H2} Effects

The dependence of TaC/a-C:H film hardness and elastic modulus on Q_{C2H2} is attributed to variations in film composition with Q_{C2H2}. The hydrogen concentration in the films increased with increasing Q_{C2H2} (Chapter 4). Film hardness decreased with increasing hydrogen concentration, as shown in Figure 5.7. The volume fraction of TaC crystallites in the films is also believed to influence film hardness and elastic modulus. The Ta concentration in the films depended statistically only on Q_{C2H2} (Chapter 4). The TaC volume fraction for the films was calculated by assuming that all Ta is bound to C as TaC, all hydrogen is located in the a-C:H phase, and the density of the a-C:H phase is 1.5 g/cm^3. The measured film hardness is plotted as a function of the calculated TaC volume fraction in Figure 5.8 (for each V_b level). The hardness of polycrystalline TaC may reach 24 GPa [55], so there is no evidence of enhanced hardness beyond that of pure TaC.

These results for TaC/a-C:H are consistent with previous reports of the hardness dependency on the volume fraction of carbide in composite films using one-at-a-time experiments with different hydrocarbon gas flow levels [10,19]. Shi et al. [56] observed with high-resolution TEM that TiC crystallites increased in size with increasing metal content in TiC/a-C:H films deposited at 600°C. In addition, images indicated that separate TiC crystallites tended to coalesce and touch at the high Ti levels. The increased

connectivity of the crystallites throughout the films corresponded to higher hardness levels and lower electrical resistivity than the films with lower Ti content.
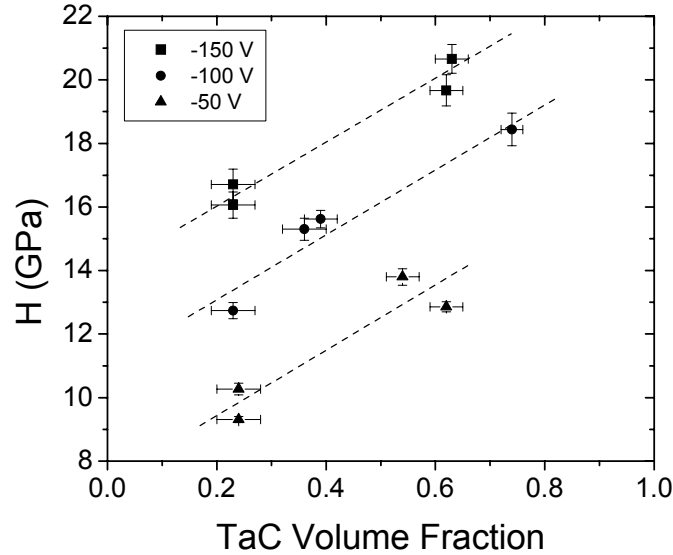
Figure 5.8. Hardness versus calculated TaC volume fraction. The data for films deposited with different V_b are distinguished by symbol type and guide lines.

5.5 CONCLUSIONS

- The compressive stress level in the TaC/a-C:H films was statistically dependent only on V_b, not Q_{C2H2} or ω_{Rot}, within the studied parameter space.

- The nanoindentation hardness and elastic modulus were statistically dependent primarily on V_b and secondarily on Q_{C2H2} with no ω_{Rot} dependence within the studied parameter space.

- The linear dependency of stress on V_b could be explained by an increase in carbon interstitial creation with increasing $|V_b|$, as suggested by TRIM simulations. The number of simulated interstitials created per ion varied

linearly with bombarding ion energy (i.e., V_b) within the studied parameter space.

- It is suggested that volumetric strain is accommodated by the a-C:H matrix phase rather than the TaC phase, because 1) TRIM simulations suggest that more C vacancies/ion are created by Ar^+ in a-C:H than in TaC, 2) dispersed TaC crystallites are ostensibly defect-free, 3) V_b statistically affected the a-C:H phase hydrogen content and structure, 4) the elastic modulus levels were consistent with the Paul lower bound, suggesting that the film constituents are under the same stress level but potentially have different local strain levels according to their elastic moduli.

- It is proposed that the dependency of hardness and elastic modulus on V_b is related to the phenomena responsible for the development of intrinsic stress. The mean coordination of C atoms in the a-C:H network is hypothesized to increase with $|V_b|$ by both chemical mechanisms (hydrogen level decrease due to chemical abstraction and displacement accompanied by additional crosslinking) and physical mechanisms (momentum transfer in knock-on collisions that produce bond distortion). If a random covalent network is assumed, an increase in the mean coordination within the C-skeleton is expected to result in a higher elastic modulus.

- Decreases in hardness and elastic modulus with increasing Q_{C2H2} are attributed to increased hydrogen concentration in the films and decreased volume fraction of TaC crystallites in the films.

5.6   REFERENCES

1. G. L. Doll and B. K. Osborn: Engineering surfaces of precision steel components, in *44th Annual Technical Conference Proceedings*. (Society of Vacuum Coaters, Philadelphia, PA, Apr. 21-26, 2001).

2. G. L. Doll, R. D. Evans, and S. P. Johnson: Providing oil-out protection to rolling element bearings with coatings, in *48th Annual Technical Conference Proceedings*. (Society of Vacuum Coaters, Denver, CO, Apr. 23-28, 2005).

3. E. Rabinowicz: *Friction and Wear of Materials*. (John Wiley & Sons, New York, 1965).

4. M. Grischke, K. Bewilogua, and H. Dimigen: Preparation, properties and structure of metal containing amorphous hydrogenated carbon films. *Mater. Manuf. Process.* **8**, 407 (1993).

5. C. Strondl, N. M. Carvalho, J. Th. M. De Hosson, and T. G. Krug: Influence of energetic ion bombardment on W-C:H coatings deposited with W and WC targets. *Surf. Coat. Tech.* **200**, 1142 (2005).

6. B. Shi and W. J. Meng: Intrinsic stresses and mechanical properties of Ti-containing hydrocarbon coatings. *J. Appl. Phys.* **94**, 186 (2003).

7. S. J. Park, K. R. Lee, D. H. Ko, and K. Y. Eun: Microstructure and mechanical properties of WC-C nanocomposite films. *Diam. Relat. Mater.* **11**, 1747 (2002).

8. B. Shi, W. J. Meng, L. E. Rehn, and P. M. Baldo: Intrinsic stress development in Ti-C:H ceramic nanocomposite coatings. *Appl. Phys. Lett.* **81**, 352 (2002).

9. C. Strondl, N. M. Carvalho, J. Th. M. De Hosson, and G. J. van der Kolk: Investigation on the formation of tungsten carbide in tungsten-containing diamond like carbon coatings. *Surf. Coat. Tech.* **162**, 288 (2003).

10. C. P. Klages and R. Memming: Microstructure and physical properties of metal-containing hydrogenated carbon films. *Mater. Sci. Forum* **52 & 53**, 609 (1989).

11. W. van Duyn and B. van Lochem: Chemical and mechanical characterization of WC:H amorphous layers. *Thin Solid Films* **181**, 497 (1989).

12. K. Bewilogua and H. Dimigen: Preparation of W-C:H coatings by reactive magnetron sputtering. *Surf. Coat. Tech.* **61**, 144 (1993).

13. W. J. Meng and B. A. Gillispie: Mechanical properties of Ti-containing and W-containing diamond-like carbon coatings. *J. Appl. Phys.* **84**, 4314 (1998).

14. W. Precht and A. Czyzniewski: Deposition and some properties of carbide/amorphous carbon nanocomposites for tribological application. *Surf. Coat. Tech.* **174**, 979 (2003).

15. A. Czyzniewski: Deposition and some properties of nanocrystalline WC and nanocomposite WC/a-C:H coatings. *Thin Solid Films* **433**, 180 (2003).

16. W. J. Meng, R. C. Tittsworth, and L. E. Rehn: Mechanical properties and microstructure of TiC/amorphous hydrocarbon nanocomposite coatings. *Thin Solid Films* **377**, 222 (2000).

17. B. Feng, D. M. Cao, W. J. Meng, L. E. Rehn, P. M. Baldo, and G. L. Doll: Probing for mechanical and tribological anomalies in the TiC/amorphous hydrocarbon nanocomposite coating system. *Thin Solid Films* **398**, 210 (2001).

18. H. Dimigen and C. P. Klages: Microstructure and wear behavior of metal-containing diamond-like coatings. *Surf. Coat. Tech.* **49**, 543 (1991).

19. W. J. Meng, T. J. Curtis, L. E. Rehn, and P. M. Baldo: Plasma-assisted deposition and characterization of Ti-containing diamondlike carbon coatings. *J. Appl. Phys.* **83**, 6076 (1998).

20. V. Kulikovsky, A. Tarasenko, F. Fendrych, L. Jastrabik, D. Chvostova, F. Franc, and L. Soukup: The mechanical, tribological and optical properties of Ti-C:H coatings, prepared by dc magnetron sputtering. *Diam. Relat. Mater.* **7**, 774 (1998).

21. T. Zehnder, P. Schwaller, F. Munnik, S. Mikhailov, and J. Patscheider: Nanostructural and mechanical properties of nanocomposite nc-TiC/a-C:H films deposited by reactive unbalanced magnetron sputtering. *J. Appl. Phys.* **95**, 4327 (2004).

22. D. P. Monaghan, D. G. Teer, P. A. Logan, I. Efeoglu, and R. D. Arnell: Deposition of wear resistant coatings based on diamond like carbon by unbalanced magnetron sputtering. *Surf. Coat. Tech.* **60**, 525 (1993).

23. C. Strondl, G. J. van der Kolk, T. Hurkmans, W. Fleischer, T. Trinh, N. M. Carvalho, and J. Th. M. de Hosson: Properties and characterization of multilayers of carbides and diamond-like carbon. *Surf. Coat. Tech.* **142**, 707 (2001).

24. D. G. Montgomery: *Design and Analysis of Experiments*, 5th ed. (John Wiley & Sons, 2001).

25. M. Ohring: *The Materials Science of Thin Films.* (Academic Press, Boston, 1992).

26. W. A. Brantley: Calculated elastic constants for stress problems associated with semiconductor devices. *J. Appl. Phys.* **44**, 534 (1973).

27. W. C. Oliver and G. M. Pharr: An improved technique for determining hardness and elastic modulus using load and displacement sensing indentation experiments. *J. Mater. Res.* **7**, 1564 (1992).

28. A. C. Ferrari, B. Kleinsorge, N. A. Morrison, A. Hart, V. Stolojan, and J. Robertson: Stress reduction and bond stability during thermal annealing of tetrahedral amorphous carbon. *J. Appl. Phys.* **85**, 7191 (1999).

29. B. Shi, W. J. Meng and T. L. Daulton: Thermal expansion of Ti-containing hydrogenated amorphous carbon nanocomposite thin films. *Appl. Phys. Lett.* **85**, 4352 (2004).

30. H. O. Pierson: *Handbook of refractory carbides and nitrides – properties, characteristics, processing and applications.* (Noyes Publications, Westwood, New Jersey, 1996).

31. T. Y. Tsui, W. C. Oliver, and G. M. Pharr: Influences of stress on the measurement of mechanical properties using nanoindentation: Part I. Experimental studies in an aluminum alloy. *J. Mater. Res.* **11**, 752 (1996).

32. Y. T. Cheng and C. M. Cheng: Scaling, dimensional analysis, and indentation measurements. *Mater. Sci. Eng. R* **44**, 91 (2004).

33. H. Windischmann: An intrinsic stress scaling law for polycrystalline thin films prepared by ion beam sputtering. *J. Appl. Phys.* **62**, 1800 (1987).

34. F. M. d'Heurle and J. M. E. Harper: Note on the origin of intrinsic stresses in films deposited via evaporation and sputtering. *Thin Solid Films* **171**, 81 (1989).

35. O. Knotek, R. Elsing, G. Kramer, and F. Jungblut: On the origin of compressive stress in PVD coatings – an explicative model. *Surf. Coat. Tech.* **46**, 265 (1991).

36. D. Nir: Summary abstract: Energy dependence of the stress in diamondlike carbon films. *J. Vac. Sci. Technol. A* **4**, 2954 (1986).

37. C. A. Davis: A simple model for the formation of compressive stress in thin films by ion bombardment. *Thin Solid Films* **226**, 30 (1993).

38. T. R. Anthony: Stresses generated by impurities in diamond. *Diam. Relat. Mater.* **4**, 1346 (1995).

39. D. L. Smith: *Thin-Film Deposition: Principles and Practice* (McGraw Hill, Boston, 1995).

40. S. Zhang, H. T. Johnson, G. J. Wagner, W. K. Liu, and K. J. Hsia: Stress generation mechanisms in carbon thin films grown by ion-beam deposition. *Acta Mater.* **51**, 5211 (2003).

41. W. Jacob: Surface reactions during growth and erosion of hydrocarbon films. *Thin Solid Films* **326**, 1 (1998).

42. J. F. Ziegler: *The Stopping and Range of Ions in Solids* (Pergammon, New York, 1985). www.srim.org.

43. J. Robertson: Diamond-like amorphous carbon. *Mater. Sci. Eng. R* **37**, 129 (2002).

44. S. Veprek: Electronic and mechanical properties of nanocrystalline composites when approaching molecular size. *Thin Solid Films* **297**, 145 (1997).

45. Y. Yin, D. McKenzine, and M. Bilek: Intrinsic stress induced by substrate bias in amorphous hydrogenated silicon thin films. *Surf. Coat. Tech.* **198**, 156 (2005).

46. B. Paul: Prediction of elastic constants of multiphase materials. *Trans. AIME* **218**, 36 (1960).

47. S. P. Dodd, M. Cankurtaran, and B. James: Ultrasonic determination of the elastic and nonlinear acoustic properties of transition-metal carbide ceramics: TiC and TaC. *J. Mater. Sci.* **38**, 1107 (2003).

48. J. C. Angus and F. Jansen: Dense "diamondlike" hydrocarbons as random covalent networks. *J. Vac. Sci. Technol. A* **6**, 1778 (1988).

49. J. C. Phillips: Topology of covalent non-crystalline solids I: Short-range order in chalcogenide alloys. *J. Non-Cryst. Solids* **34**, 153 (1979).

50. M. F. Thorpe: Continuous deformations in random networks. *J. Non-Cryst. Solids* **57**, 355 (1983).

51. J. Robertson: Mechanical properties and coordinations of amorphous carbons. *Phys. Rev. Lett.* **68**, 220 (1992).

52. H. He and M. F. Thorpe: Elastic properties of glasses. *Phys. Rev. Lett.* **54**, 2107 (1985).

53. A. von Keudell, M. Meier, and C. Hopf: Growth mechanism of amorphous hydrogenated carbon. *Diam. Relat. Mater.* **11**, 969 (2002).

54. J. A. Thornton: The microstructure of sputter-deposited coatings. *J. Vac. Sci. Technol. A* **4**, 3059 (1986).

55. J. F. Lynch, C. G. Ruderer, and W. H. Duckworth, eds: *Engineering Properties of Selected Ceramic Materials*. (American Ceramic Society, Columbus, OH, 1966).

56. B. Shi, W. J. Meng, and R. D. Evans: Characterization of high temperature deposited Ti-containing hydrogenated carbon thin films. *J. Appl. Phys.* **96**, 7705 (2004).

CHAPTER 6

EFFECTS OF APPLIED BIAS DURING TaC/a-C:H DEPOSITION

6.1 INTRODUCTION

Nanocomposite tantalum carbide/amorphous hydrocarbon (TaC/a-C:H) thin film properties depend on the d.c. bias voltage (V_b) level applied to the substrate during reactive sputter deposition. All surfaces in contact with plasma are bombarded by positive ions with energy of a few tens of eV due to the presence of the plasma potential. The addition of a cathodic V_b to substrate surfaces can increase the ion bombardment energy to a level that greatly influences the development of film composition, structure, and especially mechanical properties. Ion bombardment is a component of several reactive sputtering process steps, including substrate cleaning prior to deposition (V_b ~ -500 V), Ta-interlayer deposition (V_b ~ -50 V), and TaC/a-C:H top layer deposition (V_b ~ -50 to -150 V – see Chapters 4 and 5).

The V_b level during deposition and TaC/a-C:H film properties are closely related, making V_b a critical parameter when designing films for tribological applications. Factorial experiments in Chapters 4 and 5 revealed process-property relationships for TaC/a-C:H across the range V_b = -50 to -150 V. For example, the hydrogen concentration decreased and the argon content increased with increasing $|V_b|$. The film thickness decreased with increasing $|V_b|$. The width of the fitted G-peak in the Raman spectrum increased with increasing $|V_b|$. The x-ray diffraction data suggested that the average TaC crystallite size (dispersed phase) increased with increasing $|V_b|$. The film intrinsic compressive stress level increased with increasing $|V_b|$, as did the hardness and elastic indentation modulus. The use of V_b during reactive sputtering of TaC/a-C:H in an

argon/hydrocarbon plasma appeared to be responsible for certain process-property trend similarities to plasma-enhanced chemical vapor deposition (PECVD) of hard a-C:H thin films.

Chapter 5 reported that film hardness increased with $|V_b|$, independent of Ta content. This could be beneficial for tribological applications that require sliding contact, because the friction coefficient depends only on the film chemical composition (i.e., carbon content) and not V_b across the range V_b = -50 to -150 V [1]. Therefore, a film composition (e.g., Ta/C atomic ratio) may be selected to give the optimal friction performance, and then fine-tuned for desired hardness by adjusting V_b. However, there may be limitations on this approach, including the degradation of film adhesion with increasing film stress and hardness at high $|V_b|$. Thus, it is important to know how the film stress behaves across a wide range of V_b. The dependency of MC/a-C:H stress level on V_b has been addressed a few times in the literature in addition to the results of Chapter 5 for TaC/a-C:H. Grischke et al. [2] showed that compressive stress increased linearly for WC/a-C:H in the range V_b = 0 to -80 V using reactive sputter deposition. Strondl et al. [3] also found a linear stress relationship over the range V_b = 0 to -150 V for WC/a-C:H using unbalanced magnetron reactive sputtering. In contrast, Shi and Meng [4] showed that TiC/a-C:H compressive stress increased in the range V_b = 0 to -60 V, then remained approximately constant from -60 to -100 V. It is notable that the Shi and Meng deposition tool was a hybrid inductively coupled plasma and balanced magnetron sputtering apparatus, different than the other examples. The author is not aware of any other reactively sputtered MC/a-C:H stress data across a wider V_b range in the literature.

This Chapter seeks to further clarify the effects of V_b on nanocomposite TaC/a-C:H film properties across an expanded voltage range. A set of TaC/a-C:H films was deposited across the range V_b = 0 to -300 V with all other deposition parameters held constant except substrate temperature, which was allowed to reach its steady state during the depositions. An improved understanding of the effects of V_b on film composition and structure was sought, especially related to TaC crystallite size and dispersion. In addition, the upper limit on stress, if any, with increasing $|V_b|$ was of interest.

6.2   EXPERIMENTAL

The TaC/a-C:H films were deposited in the same closed-field unbalanced magnetron sputtering chamber described in Chapter 4, utilizing two diametrically opposite Ta sputtering targets. The substrate carousel and fixturing were exactly as before, including a Si wafer substrate ($\langle 001 \rangle$) and a polished steel coupon. There were a few minor differences in the deposition process for these films compared to those in Chapter 4. Argon plasma cleaning was performed prior to film deposition with V_b = -500 V as before, but for 600 s instead of 900 s. The argon flow rate during film deposition was 50 sccm rather than 30 sccm. The Ta interlayer deposition duration was reduced by 25%, resulting in a thinner interlayer. The acetylene flow rate (Q_{C2H2}) was 50 sccm and the substrate rotation rate (ω_{Rot}) was 2.5 rpm for all samples. The chamber base pressure was less than 6 x 10^{-3} Pa, and the pressure during film deposition was within the range 0.14 – 0.23 Pa. Other process settings such as the field coil current and Ta target sputtering power level were held constant at the same level as the previous TaC/a-C:H film deposition experiments.

In contrast to the studies described in Chapters 4 and 5 that relied on designed experiments to empirically model responses to different process condition combinations, one-factor-at-a-time experiments were performed to isolate the effect of V_b on film properties. V_b was varied from 0 to -300V in 25V increments. The films were deposited in a random order, and replicates were deposited at V_b = -100 and -250 V.

The substrate temperature was not controlled during the depositions, but it was measured using a surface thermometer mounted on the back of the bracket that holds the substrates. The thermometers only revealed the maximum temperature reached during deposition. The maximum temperature increased with increasing $|V_b|$ as shown in Figure 6.1. Likewise, the power level on the substrate carousel during deposition increased with increasing $|V_b|$, while the current remained approximately constant (P=V*I). All of the films were deposited using identical plasma etch and Ta interlayer deposition conditions, so maximum deposition temperature differences among the films are attributed to the unique power level corresponding to each V_b setpoint during the TaC/a-C:H top layer deposition.
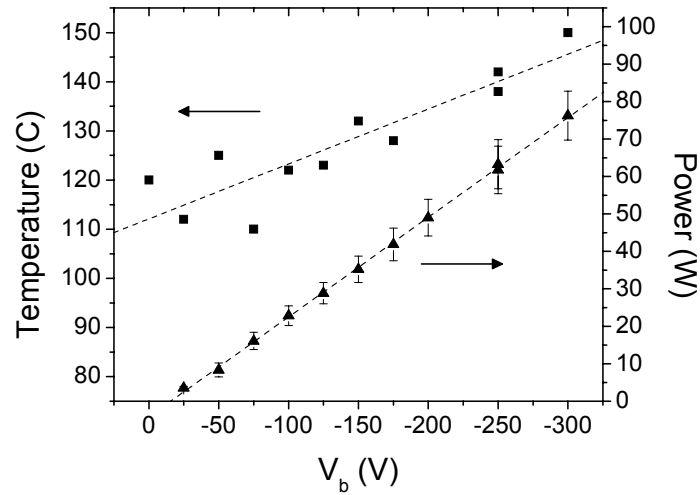
Figure 6.1. Maximum process temperature and substrate carousel power level as a function of V_b. The power level was averaged over the entire top layer deposition duration, and the error bars represent ± 1 standard deviation.

The Ta/C atomic ratio and Ar concentration were measured using an Oxford Instruments x-ray energy dispersive spectrometer (EDS) in an Amray scanning electron microscope (SEM). A few percent of Si was observed in each EDS measurement, which suggests that the analytical sampling volume exceeded the total film thickness. The Ta/C atomic ratio measurements include contributions from the Ta interlayer as a result. Thus, the reported Ta/C ratio and Ar concentration measurements may not reflect the actual TaC/a-C:H top layer composition precisely. However, the Ta interlayer was deposited exactly the same in each experiment, so relative differences are believed to be accurate. Hydrogen concentration was not detected with EDS. The film thickness was measured at the fracture edges of cleaved Si substrates in the SEM. The film hydrogen concentrations were measured using elastic recoil detection analysis (ERDA). A 4 MeV beam of alpha particles was used to dislodge hydrogen atoms in the top ~1 μm of film depth, which

were then filtered using an Al foil and detected. The technique was calibrated using mica and carbon tape standards, and the measurement error was estimated to be ±5%.

The TaC crystallites were analyzed using grazing angle x-ray diffraction with a PANalytical X'Pert Pro instrument with a Cu K_α x-ray source. The scans were conducted over a 15-85° 2θ angle range, with a step size of 0.02° and a dwell (counting) time of 1 s at each step. The angle of the beam was fixed at 0.6° (omega). A 10-point fast Fourier transform (FFT) smoothing operation was performed on the spectra, followed by linear baseline subtraction. Peaks were fit with Lorentzians, and the full peak width at half height was used with the Scherrer method to estimate the crystallite size [5]. The peak widths were not corrected for instrument broadening, which was assumed to be minimal relative to particle size broadening. Therefore the calculated average crystallite sizes are expected to represent a lower limit. Curve-fitting error estimates for the peak widths were calculated using the Origin data analysis software.

Micro-Raman spectrometry was performed in the backscattering configuration with a Jobin Yvon Horiba LabRam Micro-Raman instrument with a 20 mW HeNe laser (632.8 nm wavelength). Density filters were used to attenuate the incident beam such that spectra were obtained with 2 mW of laser power with the beam focused to a spot several micrometers in size. Beam damage was not apparent on the film surfaces or in the spectra. All spectra were collected under steady state conditions with the same settings to enable comparison of peak intensities as a measure of scattering signal strength. Raw Raman spectra were fitted with a linear background and two Gaussian peaks for analysis. Curve-fitting error estimates for the peak widths were calculated using the Origin data analysis software.

Transmission electron microscopy (TEM) samples of the films deposited with V_b = -25, -175, and -300 V were prepared in cross-section. Final preparations included dimple grinding followed by ion milling in a Gatan Precision Ion Polishing System. Conventional and high resolution TEM observations were conducted in a JEOL JEM2010 microscope operated at 200 kV.

Residual compressive stress measurements were performed by measuring wafer curvature using a MicroXAM-Phase Shift optical profilometer, and inserting those values into the Stoney equation [6]. The compressive stress values are shown as positive values on the plots. Error bars in the plot indicate measurement error and represent 95% confidence intervals about the mean stress value for each sample.

6.3 RESULTS

6.3.1 Film Composition and Thickness

The Ta/C atomic ratio as measured with SEM/EDS did not change significantly with V_b (Figure 6.2). The data scatter was statistically random. On the other hand, the amount of argon incorporated in the films measured with the same technique increased with increasing $|V_b|$ (Figure 6.3). The hydrogen concentration in the films as measured with ERDA decreased with increasing $|V_b|$ (Figure 6.4). In addition, the total film thickness decreased ~15% with increasing $|V_b|$ (Figure 6.5).
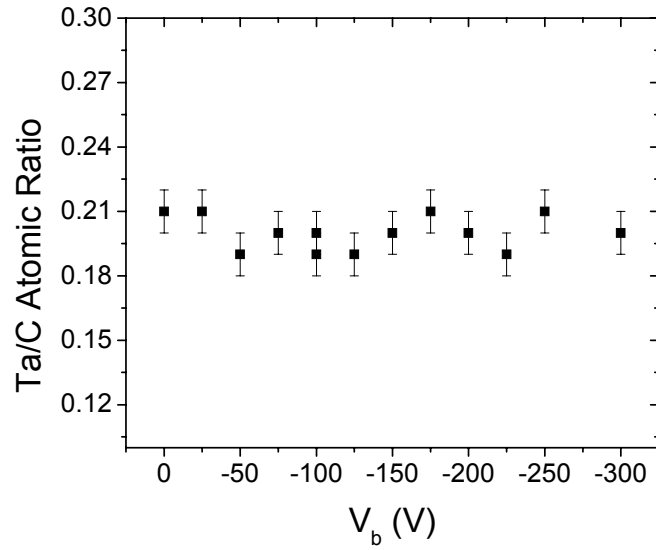
Figure 6.2. Ta/C atomic ratio measured with SEM/EDS as a function of V_b. The error bars represent a ±0.01 error estimate per measurement.
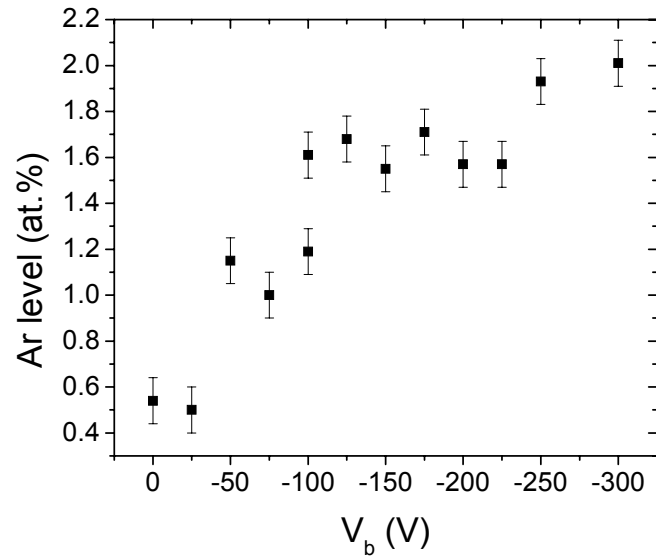
Figure 6.3. Argon concentration measured with SEM/EDS as a function of V_b. The error bars represent a ±0.1 at.% error estimate per measurement.
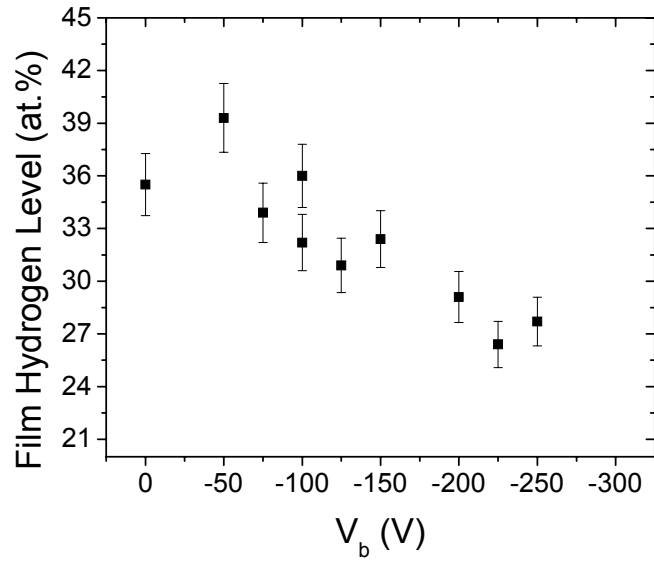
Figure 6.4. Hydrogen concentration measured with ERDA as a function of V_b. The error bars represent a ±5% error estimate per measurement.
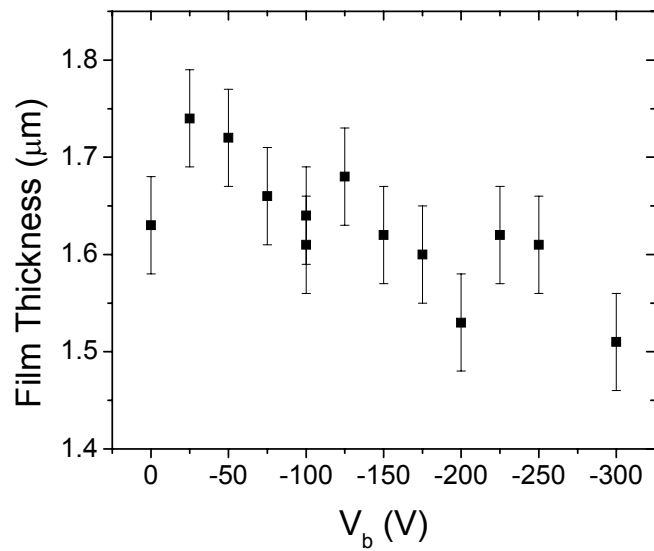
Figure 6.5. Total film thickness measured by SEM as a function of V_b. The error bars represent a ±0.05 μm error estimate per measurement.

6.3.2   Film Structure

6.3.2.1   X-ray Diffraction

The crystallinity of the TaC/a-C:H films was evaluated with grazing angle x-ray diffraction (XRD). The films contained cubic B1-TaC crystallites as expected. The average crystallite size was estimated using the Scherrer equation [5]:

$$L_{hkl} = \frac{K \cdot \lambda}{\beta \cos \theta} \qquad (6.1)$$

where L_{hkl} is a volume-average crystallite dimension perpendicular to the reflecting planes hkl, λ is the x-ray wavelength, β is the peak width (on the 2θ scale), and θ is the Bragg angle. K is a constant assumed to be unity, given the definition of L_{hkl} [5]. If the crystallites are equiaxed, L_{hkl} is an estimate of average crystallite diameter. The (111), (200), and (220) reflections were curve-fit and Scherrer calculations were performed with the resulting β values. The calculated average crystallite size increased with increasing $|V_b|$ as shown in Figure 6.6, independent of the reflection. However, the data for each reflection are shifted vertically relative to the other reflections, indicating an error type inherent to this technique. Portions of the spectra are overlapped in Figure 6.7 to further illustrate the peak differences across the range V_b = -25 to -300V. In summary, the XRD trends suggest an average crystallite size increase of about 20% from V_b = -25 to -300 V, regardless of the reflection used in the Scherrer calculation, with an average crystallite size range of 1.5 – 2.3 nm.
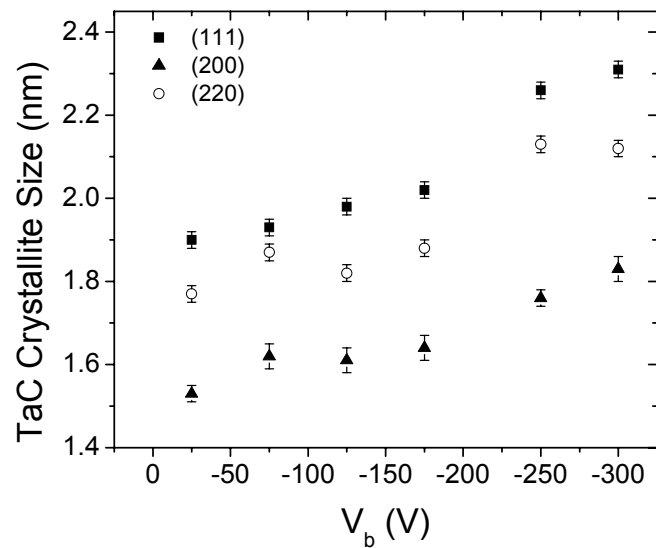
Figure 6.6. Relationship between the average TaC crystallite diameter, assuming equiaxed crystallites, and V_b from grazing angle XRD measurements. Scherrer calculations were performed on three different reflections from each spectrum as indicated in the legend. The error bars represent curve-fitting error only.
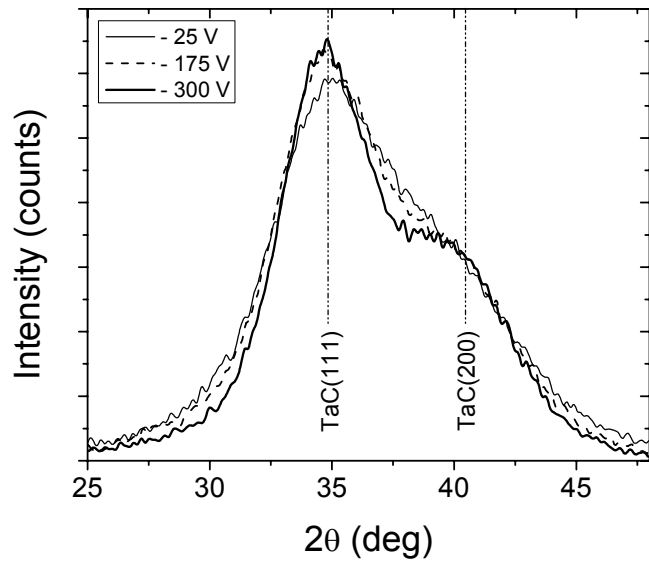
(a)
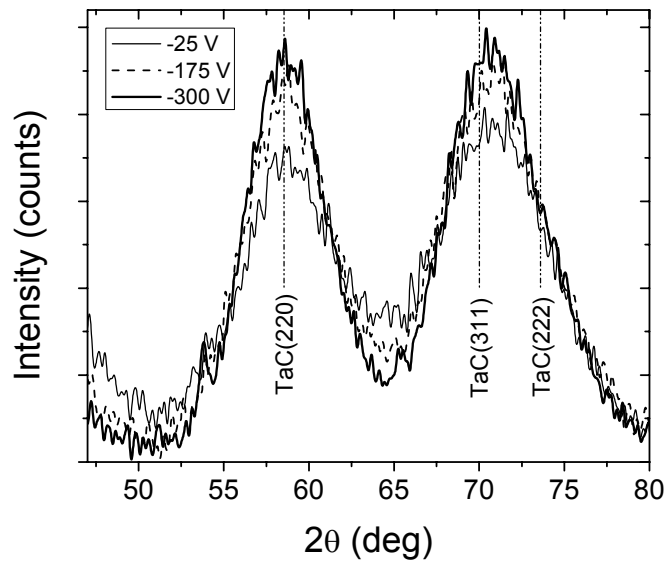
(b)

Figure 6.7. XRD spectra from the TaC/a-C:H films that are overlapped to enable peak comparisons as a function of V_b. The spectra are indexed to cubic B1-TaC. 2θ ranges of (a) 25-48° and (b) 47-80° are shown.

6.3.2.2 Raman Spectroscopy

While grazing angle XRD is useful for identifying crystallinity in MC/a-C:H thin films, Raman spectroscopy is useful for evaluating the a-C:H phase structure. The broad spectral peak between 1000 and 1800 cm^{-1} is of particular interest for amorphous carbon films. It is typically quantified by curve-fitting a G peak (1500-1600 cm^{-1}) and D peak (1300-1400 cm^{-1}). The G peak is associated with stretching vibrations of pairs of Csp^2 sites, while the D peak intensity is attributed to a breathing mode of Csp^2 sites in rings [7,8]. Raman scattering with visible photons is not directly sensitive to Csp^3 content, but if the hydrogen content of the films is known, the spectra can provide information about C-H content indirectly via the effect of such content on the Csp^2 configuration.

The G peak position, G peak width, and ratio of D and G peak intensities (I_D/I_G) are useful for characterizing a-C:H phases. Decreases in G peak position and I_D/I_G ratio are associated generally with increasing Csp^3-H content in a-C:H [9]. The G peak width (full width at half maximum) is expected to increase with Csp^2 site disorder in a-C:H [8,9]. Example spectra for the films deposited with V_b = -25, -175, and -300 V are shown in Figure 6.8(a). With the exception of the films deposited with V_b = 0 and -25 V, the TaC/a-C:H films did not show a trend in G peak position or I_D/I_G ratio as a function of V_b. The films with V_b = 0 and -25 V had a higher G peak position and I_D/I_G ratio than the other films. It is shown in Figure 6.8(b) that the G peak width increased with increasing $|V_b|$.
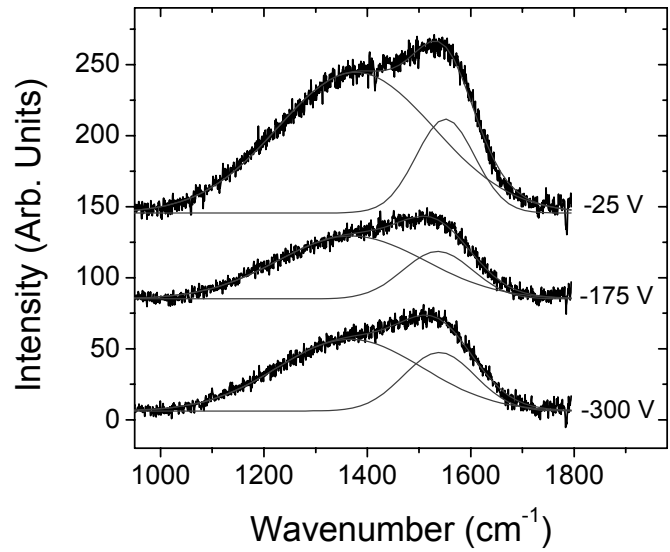
(a)
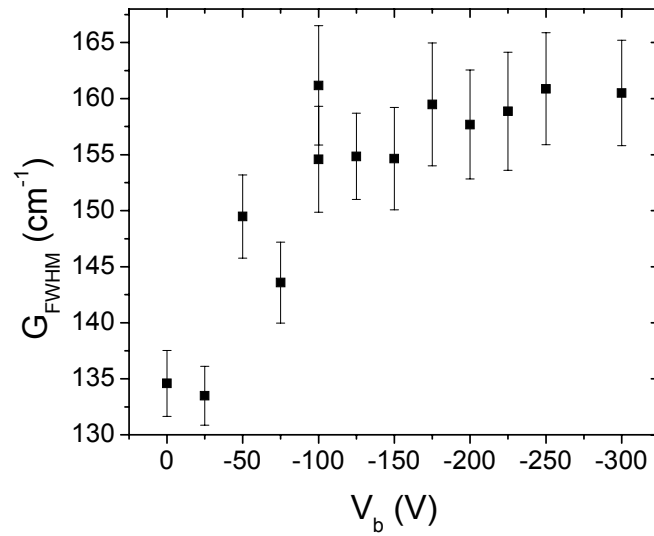
(b)

Figure 6.8. (a) Selected Raman spectra from the TaC/a-C:H films that represent the V_b range. Each spectrum is fit with Gaussian-type D and G peaks. The plots are identified by the V_b levels to the right of each spectrum. (b) G peak width trend with increasing $|V_b|$. The error bars represent curve-fitting error only.

6.3.2.3 High Resolution Transmission Electron Microscopy (HRTEM)

Unlike XRD and Raman spectroscopy, high resolution transmission electron spectroscopy (HRTEM) is used to examine film structure with nearly atomic-scale spatial resolution. Films deposited with V_b = -25, -175, and -300 V were investigated with HRTEM in a cross-sectional view. An example image with diffraction patterns from the TaC/a-C:H layer of the V_b = -175 V film is shown in Figure 6.9. The films had a nanometer-scale lamellar structure with alternating dark crystalline and bright amorphous layers. The lamellae were oriented approximately parallel to the substrate surface plane (normal to the growth direction). The selected area diffraction (SADP) inset in the lower right corner of Figure 6.9 indicates cubic TaC with the B1 (NaCl) structure type, consistent with XRD. Although the base structure appears to consist of TaC crystallites suspended in an a-C:H matrix, the dark layers had a higher content of crystalline TaC as compared to the brighter a-C:H containing layers. No medium- or long-range order was detectable in the a-C:H matrix regions. The a-C:H-rich layers appear bright in the images because they have lower density than the darker Ta-rich regions (Z-contrast). The dark regions with lattice fringes indicate TaC crystallites.

In Chapter 4 it was shown that the periodicity of the lamellae was highly dependent on the substrate carousel rotation rate (Figure 4.11) and also on the acetylene flow rate during deposition (Table 4-2). The high resolution SADP in the upper left corner of Figure 6.9 indicates a side-band intensity modulation around the transmitted beam spot. This results from large scale density and/or composition fluctuations in the sample, i.e., the lamellae. The modulation period was calculated from the pattern to be ~3.4 nm, giving a deposit thickness of ~6.8 nm per substrate carousel revolution. This is consistent

with the results presented in Table 4-2 (Film D, in particular). The film deposited with V_b = -25 V appeared to have the most poorly layered structure, with nearly indistinguishable side-band intensity modulations as compared to the V_b = -175 and -300 V samples.
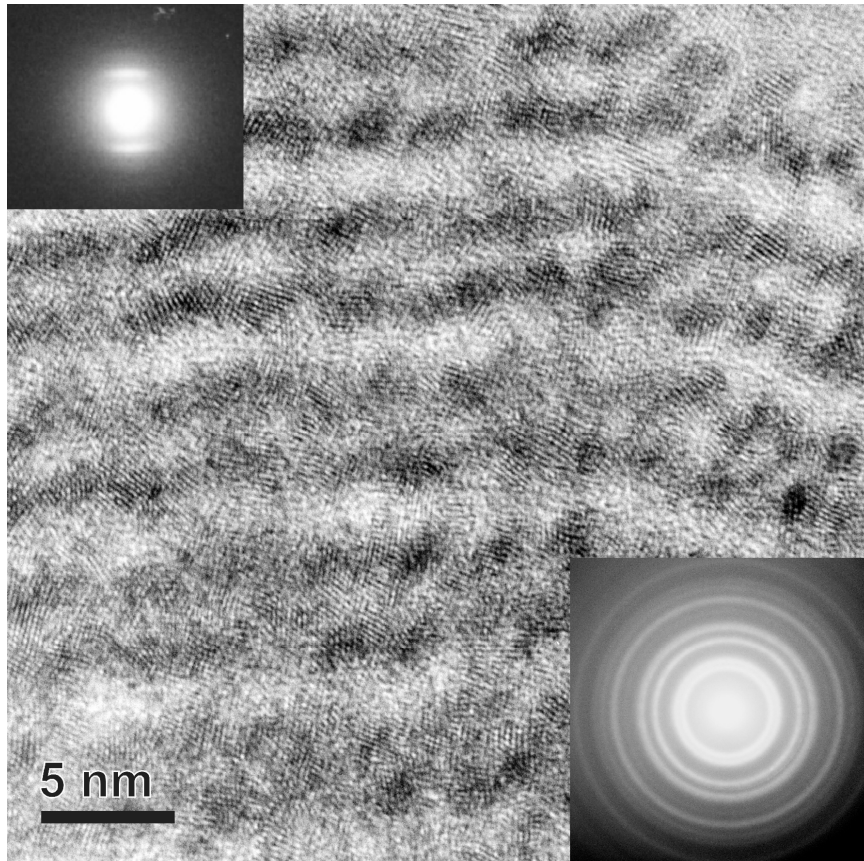
Figure 6.9. HRTEM image from the TaC/a-C:H film deposited with V_b = -175 V. A selected area diffraction pattern (SADP) from the film is inset in the lower right corner, and was indexed to B1-TaC. A high resolution SADP is inset in the upper left corner that shows side-band intensity modulation around the transmitted beam spot.

High resolution images of individual TaC crystallites from the V_b = -25V, -175V, and -300V films are shown in Figure 6.10. The crystallites appeared to have an equiaxed shape, justifying the assumption that L_{hkl} from the Scherrer calculations is representative of a mean crystallite diameter. The interface between the crystallites and matrix appeared to be somewhat abrupt at the length scale of Figure 6.10, although not necessarily abrupt on an atomic level. The crystallites did not appear to be surrounded by oriented graphene layers as observed in sputtered nanocomposites with a hydrogen-free a-C matrix phase [10]. The observed crystallite sizes were on the same order of magnitude as indicated by the XRD Scherrer calculation results (Figure 6.6). However, the distribution of crystallite sizes observed in the images made it impractical to compare average TaC crystallite size among the films, and if anything, suggested that all of the films have nearly the same crystallite size distribution as a function of V_b. That is, the HRTEM observations did not confirm or disprove the XRD measurements suggesting a 20% increase in crystallite size across the V_b range. HRTEM did confirm that the distribution of crystallite sizes was ~1.5-3.5 nm, in approximate agreement with the XRD results.
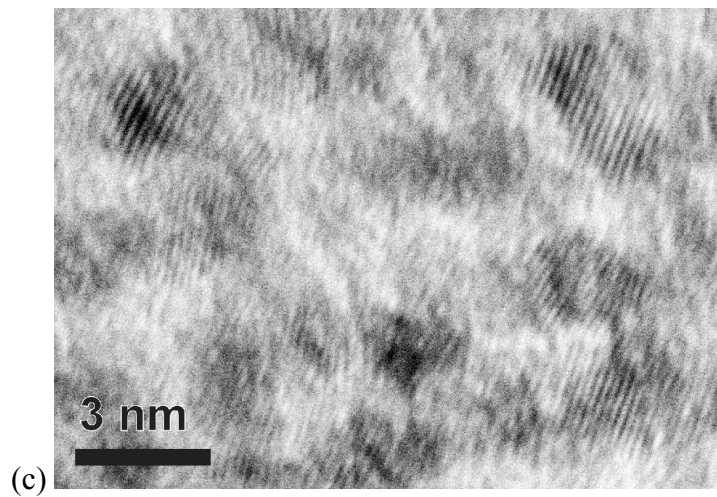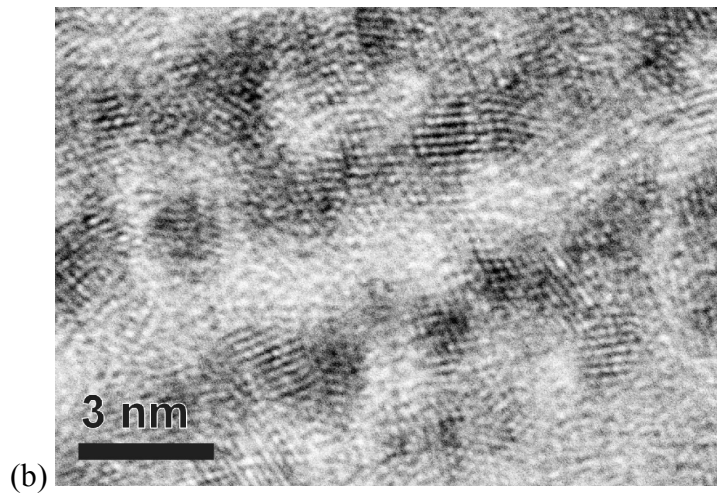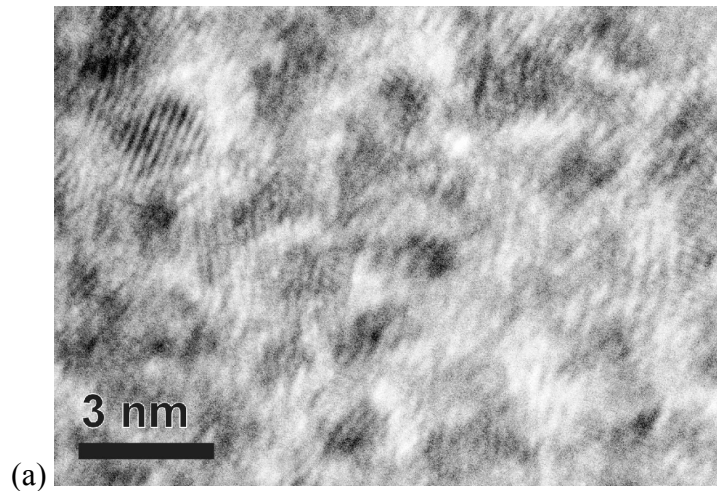
Figure 6.10. HRTEM images of individual TaC crystallites from the V_b = (a) -25 V, (b) -175 V, and (c) -300 V samples.

6.3.3 Compressive Stress

The film compressive stress σ_f increased with increasing $|V_b|$, reached a maximum around V_b = -175 V, and then appeared to remain constant or possibly decrease. The compressive stress data are shown in Figure 6.11 as a function of V_b. The stress is believed to be intrinsic in nature, and contributions from extrinsic stress such as thermal mismatch stress are neglected here for the same reasons given in Section 5.3.1. The error bars for certain samples are large relative to the others due to excessive data scatter attributable to measurement error. The σ_f levels of a few GPa were consistent with expectations for MC/a-C:H films in general. The films deposited at V_b greater than -200 V were very delicate and prone to delamination, which indicates the negative impact of high stress levels on film adhesion.
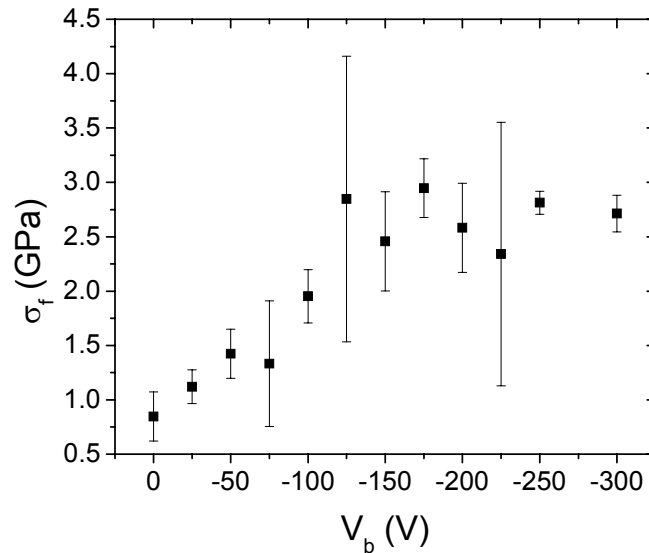
Figure 6.11. Film compressive stress as a function of V_b. The error bars indicate 95% confidence intervals on the mean of each measurement.

6.4   DISCUSSION

The composition and thickness trends across the range V_b = 0 to -300 V were consistent with the results described in Chapter 4 for the range V_b = -50 to -150 V. Furthermore, the interpretation of results in Chapter 4 is supported by the new data. For example, the Ta/C atomic ratio was found to depend only on the acetylene gas flow rate and target sputtering conditions in Chapter 4 for the range V_b = -50 to -150 V. Accordingly, the Ta/C atomic ratio was constant across the larger range V_b = 0 to -300 V because those conditions were held constant. The increase in film argon concentration with increasing $|V_b|$ was consistent with previous explanations attributing it to ion implantation. As Ar^+ bombardment energy increases with $|V_b|$, Ar atoms implant at greater film depths thus making Ar diffusion out of the film less rapid. The hydrogen concentration in the films decreased with increasing $|V_b|$, which was consistent with the interpretation that increased H^+ implantation depth at high $|V_b|$ increases the probability of hydrogen abstraction reactions that tend to reduce the overall hydrogen concentration in the film. The film thickness decrease may be attributable to a-C:H phase densification by ion bombardment and/or hydrogen abstraction, or possibly even sputtering effects at V_b ~ -300 V.

The grazing angle XRD spectra indicated the presence of cubic B1-TaC crystallites in the films. The peak widths in the spectra were broader for the films deposited at lower $|V_b|$. According to Scherrer analysis, the average TaC crystallite size (lower limit) increased approximately 20% as V_b was changed from 0 to -300 V. This small difference was not distinguishable in the HRTEM images; instead a distribution of crystallite sizes in the 1.5 − 3.5 nm range was observed in the films (V_b = -25, -175, and -300 V),

consistent with the XRD analysis. As suggested in Chapter 5, it is likely that differences in film hardness, elastic modulus, and/or compressive stress with V_b are attributable to the a-C:H matrix rather than subtle changes in TaC average crystallite size (i.e., the 20% increase with $|V_b|$ via XRD measurements). Patscheider et al. [11] concluded from studies of nanocomposite TiN/a-Si_3N_4 and TiC/a-C:H that the film mechanical properties are determined by the amorphous phase alone when the mean crystallite separation exceeds ~0.5 nm and the crystallite size is less than 10 nm. The lamellar structure of the TaC/a-C:H films ensures that the crystallite separation between layers exceeds the Patscheider heuristic, and the Chapter 5 mechanical property analyses likewise pointed to the importance of the a-C:H matrix in determining the TaC/a-C:H film mechanical properties. Furthermore, the crystallite size did not appear to decrease with increasing $|V_b|$ in either the XRD or HRTEM results as observed by Zehnder et al. [12] for TiC/a-C:H films deposited with rf biasing. It is noteworthy that the Zehnder et al. experiments apparently did not include substrate rotation, so a lamellar film structure was probably not observed. Since crystallite growth presumably is limited in part by the coverage rate of a-C:H phase material during the deposition process, the nature of the substrate movement relative to the targets within the chamber is one of several variables that must be considered when comparing data from different laboratories.

It is speculated that the XRD-observed average crystallite size increase with $|V_b|$ under the conditions of the present study was attributable to higher substrate surface temperatures with increasing $|V_b|$. It was shown in Figure 6.1 that the maximum temperature on the substrate bracket during deposition increased with increasing $|V_b|$.

This is expected, as the temperature rise due to ion bombardment is expected to have the following general form [13]:

$$\Delta T \approx C \cdot f(P,t) \qquad (6.2)$$

where ΔT is the substrate surface temperature increase, C represents constants that depend on geometry and substrate thermal properties, and $f(P, t)$ is a function dependent on the ion beam power P and time t. Accordingly, the measured power level on the substrate carousel during the experiments increased linearly with increasing $|V_b|$ (Figure 6.1). Every film deposition was conducted for the same duration. If adatom diffusivity is explainable using an Arhennius expression, then the typical surface diffusion length would be expected to increase with increasing surface temperature. The following expressions illustrate these simple relationships [14]:

$$\ell \approx 2\sqrt{Dt} \qquad (6.3)$$

$$D = D_0 e^{-E_s/RT} \qquad (6.4)$$

where ℓ is the surface diffusion path length, D is the surface diffusivity, t is time, D_0 is a frequency factor, E_s is the activation energy for diffusion, R is the gas constant, and T is temperature. Increased adatom diffusion path lengths may favor TaC grain coarsening on the surface during deposition rather than the formation of many separate nuclei that are frozen in place. It is clear that additional studies are needed to elucidate the atomistic mechanisms of carbide crystallite growth in reactively sputtered MC/a-C:H films with and without substrate rotation.

Another observation from the TEM data was that the TaC/a-C:H films with $V_b = -175$ and -300 V had a more well-defined lamellar structure than the film with -25 V. This may be due to increased compression of the a-C:H phase by ion bombardment during

deposition at the higher $|V_b|$ levels, especially when the substrates are positioned away from the targets during each carousel rotation. Additional support for this explanation is the trend towards increased Raman G peak widths with increasing $|V_b|$, which suggests higher levels of disorder in the interlinked Csp^2 content. On the other hand, Raman analysis suggested that the low $|V_b|$ films contained less distorted Csp^2 content (G peak width) and lower concentrations of Csp^3-H, even though the total hydrogen concentration was highest in those films. In summary, the low $|V_b|$ films appeared to have a lower density and a more highly hydrogenated a-C:H matrix with minor distortion of the Csp^2 content. In comparison, the high $|V_b|$ films appeared to have a more highly compressed a-C:H matrix containing more Csp^3-H content and highly distorted Csp^2 content.

Compressive stress σ_f increased with increasing $|V_b|$, reached a maximum around $V_b =$ -175 V, and then appeared to remain constant or possibly decrease. The monotonic σ_f trend within the range $V_b =$ -50 to -150 V was explained using a model based on interstitial creation in the a-C:H matrix by Ar^+ (and/or C^+) bombardment damage during growth in Chapter 5. However, a stress relaxation mechanism apparently became significant at ion bombardment energies greater than that corresponding to the stress maximum ($V_b =$ -175 V).

Stress relaxation at high ion bombardment energies has been considered extensively in the thin films and amorphous carbon literature. However, studies have usually focused on single phase films, especially the case where the bombarding ion is the same element as the film atoms, such as tetrahedral amorphous carbon. Davis [15] addressed stress relaxation at high ion bombardment energy in thin film growth by combining

Windischmann [16] knock-on implantation with classical thermal spike principles via a steady state analysis to arrive at the following simple analytical expression for σ_f:

$$\sigma_f(E_i) \propto \left(\frac{Y_f}{(1-v_f)}\right)\left(\frac{E_i^{1/2}}{(J_r/J_i)+0.016\rho(E_i/E_0)^{5/3}}\right) \qquad (6.5)$$

where Y_f is the film elastic modulus, v_f is the film Poisson's ratio, E_i is the bombarding ion energy, J_r is the deposition flux, J_i is the ion flux, ρ is a material parameter of order 1, and E_0 is an effective excitation energy for relaxation by atomic migration [15]. The thermal spike term $0.016\rho(E_i/E_0)^{5/3}$ was also used in the original Robertson subplantation model [17] to describe the "relaxation" from Csp^3 back to Csp^2 at high C^+ ion energies. Although classical thermal spike analysis may not be completely appropriate for carbon films, it provides a conceptual basis for thinking about how energy from hyperthermal bombarding particles can be transferred into heat (phonons) and affect local structure (i.e., "relax") as the ions are stopped in the near surface region. A conceptual alternative to thermal defect (or $Csp^3 \rightarrow Csp^2$ in subplantation) relaxation at high ion bombardment energies is radiation-enhanced diffusion or thermal migration relaxation, such as that applied by Hirvonen et al. [18]. Robertson recently generalized his simple subplantation model to account for radiation-enhanced diffusion and substrate temperature differences [19]. It is unclear whether these simple analytical models properly account for the stress relaxation shown for the TaC/a-C:H case shown in Figure 6.11. It is believed that the combination of high-energy Ar^+ and C^+ ion bombardment at high $|V_b|$ produced stress saturation or relaxation by some thermally-driven means, but additional experiments with controlled substrate temperatures are required to verify that hypothesis.

The data offer some clues about structural changes as a function of V_b that may be related to stress relaxation. Ion bombardment at high $|V_b|$ did not appear to produce an increase in long-range graphitic ordering of the a-C:H phase. Such differences among the films as a function of V_b would have been detectable in the Raman spectra [20] and hydrogen concentration data. The film lamellar structure and TaC crystallite size and shape did not change appreciably from V_b = -175 to -300 V in HRTEM observations. Future investigations should examine whether crystallite-matrix interactions affect stress saturation or relaxation at high $|V_b|$. Another interesting observation was the location of the stress maximum with respect to the ion bombardment energy per carbon atom. The bombarding energy would be ~100 eV per carbon atom if the energy is divided equally when a $C_2H_y^+$ molecular ion impacts the surface at V_b = -175 V (or E_i ~ 195 eV, assuming a plasma potential of ~20 V). This is consistent with the C^+ bombardment energy that produces the maximum Csp^3 content in tetrahedral amorphous carbon deposition with certain filtered beam deposition processes [21].

6.5   SUMMARY AND CONCLUSIONS

The following trends were observed for reactively sputtered TaC/a-C:H films deposited across the range V_b = 0 to -300 V with all other deposition conditions held constant except temperature, which was allowed to vary with the plasma conditions:

- Ta/C atomic ratio in the films was unaffected by V_b.

- Ar concentration in the films increased with increasing $|V_b|$.

- Hydrogen concentration in the films decreased with increasing $|V_b|$.

- Film thickness decreased with increasing $|V_b|$.

- Grazing angle XRD indicated that the average TaC crystallite size in the films increased ~20% as V_b was changed from -25 to -300 V.

- The Raman G-peak width increased with increasing $|V_b|$.

- Films contained cubic B1-TaC crystallites mostly in the size range ~1.5-3.5 nm in an a-C:H matrix for the three films examined in HRTEM (V_b = -25, -175, and -300 V).

- Nanometer-scale layers in the film were less well-defined in the V_b = -25 V film as compared to the -175 and -300 V films in HRTEM.

- Film compressive stress increased with increasing $|V_b|$, reached a maximum at V_b ~ -175 V, and then remained constant or possibly decreased.

The new process-property trends did not conflict with previous data for the TaC/a-C:H films from Chapters 4 and 5, and the previous interpretations appear to be valid for these new results. Although XRD suggested the TaC crystallite size increased with $|V_b|$ on average, it was not discernable in HRTEM. Any average crystallite size increase is speculated to be related to the increase in substrate temperature with increasing $|V_b|$ that would promote greater adatom mobility during deposition. The most noticeable structural difference observed in TEM was that the V_b = -25 V film contained less well-defined lamellae than the V_b = -175 or -300 V films. This observation may further highlight the role of E_i in creating a compressed a-C:H phase during film deposition. This is believed to be the first time that a stress level saturation or decrease was reported for MC/a-C:H films deposited using magnetron reactive sputtering. Modeling of structural relaxation processes that are dependent on E_i is a topic of on-going research in the tetrahedral amorphous carbon community. Although data from the present study

offer clues about possible mechanisms for stress relaxation at high $|V_b|$ levels, additional

experiments and modeling studies are needed.

6.6 REFERENCES

1. R. D. Evans, G. L. Doll, J. T. Glass: in preparation for *Tribol. Trans.*

2. M. Grischke, K. Bewilogua, and H. Dimigen: Preparation, properties and structure of metal containing amorphous hydrogenated carbon films. *Mater. Manuf. Process.* **8**, 407 (1993).

3. C. Strondl, N. M. Carvalho, J. Th. M. De Hosson, and T. G. Krug: Influence of energetic ion bombardment on W-C:H coatings deposited with W and WC targets. *Surf. Coat. Tech.* **200**, 1142 (2005).

4. B. Shi and W. J. Meng: Intrinsic stresses and mechanical properties of Ti-containing hydrocarbon coatings. *J. Appl. Phys.* **94**, 186 (2003).

5. H. P. Klug and L. E. Alexander: *X-ray diffraction procedures for polycrystalline and amorphous materials*, 2nd ed. (John Wiley & Sons, New York, 1974).

6. M. Ohring: *The Materials Science of Thin Films.* (Academic Press, Boston, 1992).

7. A. C. Ferrari and J. Robertson: Interpretation of Raman spectra of disordered and amorphous carbon. *Phys. Rev. B* **61**, 14095 (2000).

8. J. Roberston: Diamond-like amorphous carbon. *Mat. Sci. Eng. R* **37**, 129 (2002).

9. M. A. Tamor and W. C. Vassell: Raman "fingerprinting" of amorphous carbon films. *J. Appl. Phys.* **76**, 3823 (1994).

10. D. Babonneau, T. Cabioc'h, A. Naudon, J. C. Girard, and M. F. Denanot: Silver nanoparticles encapsulated in carbon cages obtained by co-sputtering of the metal and graphite. *Surf. Sci.* **409**, 358 (1998).

11. J. Patscheider, T. Zehnder, and M. Diserens: Structure-performance relations in nanocomposite coatings. *Surf. Coat. Tech.* **146**, 201 (2001).

12. T. Zehnder, P. Schwaller, F. Munnik, S. Mikhailov, and J. Patscheider: Nanostructural and mechanical properties of nanocomposite nc-TiC/a-C:H films deposited by reactive unbalanced magnetron sputtering. *J. Appl. Phys.* **95**, 4327 (2004).

13. M. E. Mack, Wafer cooling and wafer charging in ion implantation, in *Handbook of Ion Implantation Technology*, J. F. Ziegler, ed. (Elsevier, Amsterdam, 1992).

14. D. L. Smith: *Thin-Film Deposition: Principles and Practice* (McGraw Hill, Boston, 1995).

15. C. A. Davis: A simple model for the formation of compressive stress in thin films by ion bombardment. *Thin Solid Films* **226**, 30 (1993).

16. H. Windischmann: An intrinsic stress scaling law for polycrystalline thin films prepared by ion beam sputtering. *J. Appl. Phys.* **62**, 1800 (1987).

17. J. Robertson: The deposition mechanism of diamond-like a-C and a-C:H. *Diam. Relat. Mater.* **3**, 361 (1994).

18. J. P. Hirvonen, J. Koskinen, M. Kaukonen, R. Nieminen, and H. J. Scheibe: Dynamic relaxation of the elastic properties of hard carbon films. *J. Appl. Phys.* **81**, 7248 (1997).

19. J. Robertson: Mechanism of sp^3 bond formation in the growth of diamond-like carbon. *Diam. Relat. Mater.* **14**, 942 (2005).

20. B. Shi, W. J. Meng, and R. D. Evans: Characterization of high temperature deposited Ti-containing hydrogenated carbon thin films. *J. Appl. Phys.* **96**, 7705 (2004).

21. Y. Lifshitz: Diamond-like carbon—present status. *Diam. Relat. Mater.* **8**, 1659 (1999).

CHAPTER 7

SUMMARY AND FUTURE WORK

7.1   SUMMARY

Tribological thin films are of critical interest to designers and end-users of friction management and load transmission components such as steel rolling element bearings. Their presence on bearing surfaces is inevitable via *in situ* chemical reactions with species from the environment and/or lubricant. Oxygen promotes the formation of iron oxide thin films on steel bearing surfaces during tribological contact. Most often, lubricant additives are used with the intention of producing "antiwear" films on tribological surfaces. Alternatively, engineered thin films may be deposited or formed intentionally on tribological surfaces prior to service with the goal of improving friction and wear performance. The research reported herein sought to reveal new information about the nature and properties of thin films on steel rolling element bearing surfaces, spanning the scope of their technical evolution: natural oxide films → antiwear films from lubricant additives → engineered nanocomposite metal carbide/amorphous hydrocarbon (MC/a-C:H) films.

The presence of oxide and/or antiwear films on steel rolling element bearing surfaces can either minimize or accelerate wear, depending on the film properties and application conditions. Prior to this work, the structure of natural oxide films on steel rolling element bearing surfaces as a function of tribological conditions had not been characterized in cross-section with nanometer-scale spatial resolution. The same was true for antiwear films formed by conventional, commercially available gear oil additives. It was known that MC/a-C:H films could help to enhance bearing performance by (i) minimization of

adhesive interactions by contacting asperities, and (ii) micro-polishing of uncoated counterface asperities during service. It was known also that MC/a-C:H properties could be tailored to meet these objectives by selecting proper deposition process conditions. However, an improved understanding of process-property relationships for reactively sputtered MC/a-C:H was needed to optimize these films for wear applications and to probe the limits of nanocomposite material properties.

The present research addressed those needs by characterizing the cross-sectional composition and structure of naturally-occurring oxide films and additive antiwear films. Commercially-available bearing surfaces were examined as a function of tribological contact severity using transmission electron microscopy (TEM) of specimens prepared with focused ion beam (FIB) milling. The role of reactive sputtering deposition process conditions on the composition, structure, and mechanical properties of TaC/a-C:H thin films was determined using designed experiments. This isolated process-property relationships and enabled mechanistic interpretation of the film growth processes. The role of d.c. bias voltage applied to the substrates during growth was further explored for TaC/a-C:H films by one-factor-at-a-time experiments across an expanded voltage parameter space compared to the initial designed experiments.

In Chapter 2, TEM analyses were performed on the near-surface material from tapered roller bearing inner rings (cones) that were tested at two levels of boundary-lubrication severity ($\Lambda \sim 1.1$ and 0.3, where Λ is the ratio of lubricant film thickness to initial composite surface roughness) with a mineral oil base stock. TEM was used to obtain surface layer images, crystallographic information, and chemical compositions from cone near-surface material (depth < 500 nm) with nanometer-scale spatial

resolution. The near-surface material in an untested steel tapered roller bearing cone was mostly ferrite (with possible martensite), had a grain size gradient as a function of depth, and microstructural distortion in a direction parallel to the cone raceway surface. Two types of oxide surface layers (or boundary films) were characterized in cross-section, each one corresponding to a different severity of local boundary lubrication during testing. For the cone tested at $\Lambda \sim 1.1$, a continuous, coherent and partially crystalline surface layer containing Fe_3O_4 and ferrite was observed. For the cone tested at $\Lambda \sim 0.3$, a mostly amorphous oxygen-rich surface layer containing α-Fe_2O_3 crystallites and possibly Fe_3O_4 and $Fe_{1-x}O$ was observed. Microcracks were observed in the near-surface material of the cone tested at $\Lambda \sim 0.3$. Energy dispersive spectroscopy analysis revealed a significant amount of oxygen and carbon in the cracks. The differences in oxidation state of the iron oxide surface films as a function of contact severity were attributed in part to the oxidation level of the mineral oil lubricant.

Gear oil lubricants containing sulfur- and phosphorus-containing additives (S-P additives) are used widely in power transmission equipment, including industrial gear drives and both light and heavy truck transmissions and axles. Steel tapered roller bearings are used in these applications and sometimes experience corrosive wear and micropitting. For this reason, a better understanding of the interaction between S-P gear oil additives and rolling element bearing contact surfaces was of interest and was discussed in Chapter 3. FIB sample preparation and TEM techniques were used to analyze cross-sectional samples of antiwear films on steel tapered roller bearing cone surfaces tested in mineral oil with sulfur- and phosphorus-containing gear oil additives (S-P additives). Continuous and adherent antiwear surface layers (20-100 nm thick) were

found on the cone surfaces after bearing testing at $\Lambda \sim 1.1$ and 0.3. A sharp interface < ~10 nm thick separated the antiwear surface layer and base steel. No evidence of S or P diffusion into the steel near-surface material was found. Irregular image contrast and electron diffraction indicated that the $\Lambda \sim 1.1$ and 0.3 antiwear surface layers had a heterogeneous structure consisting of local crystalline and amorphous regions. The antiwear surface layers from cones tested at $\Lambda \sim 1.1$ and 0.3 both contained Fe, O, and P in iron oxide and phosphate/phosphite forms as determined by XPS and EDS. Crystalline wustite ($Fe_{1-x}O$) was identified in the antiwear surface layer from the cone tested at $\Lambda \sim 1.1$ using convergent beam electron diffraction. Measured planar spacings from other crystalline regions within the $\Lambda \sim 1.1$ and 0.3 surface layers were consistent with various mixed iron oxides. In the antiwear surface layers from the cone tested at $\Lambda \sim 0.3$, EDS spectra and elemental image mapping suggested that elements tended to segregate into three types of regions: (i) Fe, O, P, and Ca (crystalline), (ii) Fe, O (crystalline), and (iii) Fe, O, S, and C (amorphous). Near-surface ferrite grains from the cones tested at $\Lambda \sim 1.1$ appeared to be more equiaxed in the dimensions studied than those from the cones tested at $\Lambda \sim 0.3$, regardless of the presence of S-P additives in the lubricant. In contrast to the results for base mineral oil tests (Chapter 2), no microcracks were observed in the near-surface material of the cone tested at $\Lambda \sim 0.3$ with S-P additives. The antiwear film formation mechanism was not established during this S-P additive formulation study. However, similarities between the films observed in this study and features of popular zinc dialkyl dithiophosphate film deposition schematic models were discovered.

MC/a-C:H thin films are being used on precision steel component surfaces and steel rolling element bearings as low friction, wear-resistant coatings. The purpose of the

work described in Chapter 4 was to deposit and analyze a set of TaC/a-C:H films in a statistically rigorous manner to summarize the responses of composition and structure to changes in three key deposition process control variables: acetylene flow rate (Q_{C2H2}), applied d.c. bias voltage (V_b), and substrate rotation rate (ω_{Rot}). The key property trends within the studied parameter space can be summarized as follows:

- Film Ta/C atomic ratio increased with decreasing Q_{C2H2} only.

- Hydrogen concentration in the films increased with increasing Q_{C2H2} and decreased with increasing $|V_b|$. A statistically significant interaction term, $Q_{C2H2} * V_b$, indicated that the magnitude of the V_b effect on hydrogen concentration depended on the Q_{C2H2} level.

- Total film thickness increased with increasing Q_{C2H2} and decreased with increasing $|V_b|$.

- TaC crystallite size increased with decreasing Q_{C2H2}. Measurement precision limitations prevented conclusive determination of the V_b effect on crystallite size.

- Peak fits to Raman spectra confirmed an increase of Csp^3-H bonds with increasing Q_{C2H2} and the possibility of increased Csp^2 site disorder with increasing Q_{C2H2} and $|V_b|$.

- The films had a lamellar structure on a nanometer scale. The layer periodicity depended on Q_{C2H2}, ω_{Rot}, and possibly V_b.

In addition to a refinement of process-property relationships for reactively sputtered TaC/a-C:H films, the results were compared with literature data for various MC/a-C:H films and interpreted with respect to physical mechanisms for simultaneously occurring physical vapor deposition (PVD) and plasma-enhanced chemical vapor deposition

(PECVD). For example, the Ta incorporation in the film depended on sputtering conditions (PVD) whereas the hydrogen concentration in the films depended on the composition of the plasma environment and energetic ion bombardment conditions (PECVD).

The designed deposition experiments also enabled the evaluation of the effect of Q_{C2H2}, V_b, and ω_{Rot} on the film stress, hardness, and elastic modulus of TaC/a-C:H films in Chapter 5. With that knowledge, an attempt was made to qualitatively rationalize the observed mechanical property development with respect to atomic-level growth phenomena. The compressive stress level in the TaC/a-C:H films was statistically dependent only on V_b, not Q_{C2H2} or ω_{Rot}, within the studied parameter space. The nanoindentation hardness and elastic modulus were statistically dependent primarily on V_b and secondarily on Q_{C2H2} with no ω_{Rot} dependence within the studied parameter space. The linear dependency of stress on V_b could be explained by an increase in carbon interstitial creation with increasing $|V_b|$, as suggested by TRIM simulations. The number of simulated interstitials created per ion varied linearly with bombarding ion energy (i.e., V_b) within the studied parameter space. It is suggested that the volumetric strain is accommodated by the a-C:H matrix phase rather than the TaC phase, because 1) TRIM simulations suggest that more C vacancies/ion are created by Ar^+ in a-C:H than in TaC, 2) dispersed TaC crystallites are ostensibly defect-free, 3) V_b statistically affected the a-C:H phase hydrogen content and structure, 4) the elastic modulus levels were consistent with the Paul lower bound, suggesting that the film constituents are under the same stress level but potentially have different local strain levels according to their elastic moduli. It is proposed that the dependency of hardness and elastic modulus on V_b is related to the

phenomena responsible for the development of intrinsic stress. The mean coordination of C atoms in the a-C:H network is hypothesized to increase with $|V_b|$ by both chemical mechanisms (hydrogen level decrease due to chemical abstraction and displacement accompanied by additional crosslinking) and physical mechanisms (momentum transfer in knock-on collisions that produce bond distortion). If a random covalent network is assumed, an increase in the mean coordination within the C-skeleton is expected to result in a higher elastic modulus. Decreases in hardness and elastic modulus with increasing Q_{C2H2} are attributed to increased hydrogen concentration in the films and decreased volume fraction of TaC crystallites in the films. Improved understanding of mechanical property development in TaC/a-C:H thin film deposition enables the efficient design of wear-resistant coatings for steel rolling element bearing applications.

The purpose of the work described in Chapter 6 was to further clarify the effect of V_b during deposition on nanocomposite TaC/a-C:H thin film composition, structure, and compressive stress. The following trends were observed for reactively sputtered TaC/a-C:H films deposited across the range $V_b = 0$ to -300 V with all other deposition conditions held constant except temperature, which was allowed to vary with the plasma conditions:

- Ta/C atomic ratio in the films was unaffected by V_b.

- Ar concentration in the films increased with increasing $|V_b|$.

- Hydrogen concentration in the films decreased with increasing $|V_b|$.

- Film thickness decreased with increasing $|V_b|$.

- Grazing angle XRD indicated that the average TaC crystallite size in the films increased ~20% as V_b was changed from -25 to -300 V.

- The Raman G-peak width increased with increasing $|V_b|$.

- Films contained cubic B1-TaC crystallites mostly in the size range ~1.5-3.5 nm in an a-C:H matrix for the three films examined in HRTEM (V_b = -25, -175, and -300 V).

- Nanometer-scale layers in the film were less well-defined in the V_b = -25 V film as compared to the -175 and -300 V films in HRTEM.

- Film compressive stress increased with increasing $|V_b|$, reached a maximum at V_b ~ -175 V, and then remained constant or possibly decreased.

The new process-property trends did not conflict with previous data for the TaC/a-C:H films from Chapters 4 and 5, and the previous interpretations appear to be valid for these new results. Although XRD suggested the TaC crystallite size increased with $|V_b|$ on average, it was not discernable in HRTEM. An increase in average crystallite size is speculated to be related to the increase in substrate temperature with increasing $|V_b|$ that would promote greater adatom mobility during deposition. The most noticeable structural difference observed in TEM was that the V_b = -25 V film contained less well-defined lamellae than the V_b = -175 or -300 V films. This observation may further highlight the role of E_i in creating a compressed a-C:H phase during film deposition. This is believed to be the first time that a stress level saturation or decrease was reported for MC/a-C:H films deposited using magnetron reactive sputtering. Modeling of structural relaxation processes that are dependent on E_i is a topic of on-going research in the tetrahedral amorphous carbon community. Although data from the present study offer clues about possible mechanisms for stress relaxation at high $|V_b|$ levels, additional experiments and modeling studies are needed.

7.2 FUTURE WORK

Almost all heavy mechanical equipment relies on some type of steel rolling element bearing to reduce friction and transmit mechanical power. Additional improvements in the understanding and control of tribological thin films will translate into real improvements to society, including improved durability and energy efficiency of tribological components. A few opportunities for future development are proposed in the following sections.

7.2.1 Kinetics of Oxide Formation on Steel Surfaces

Environmental regulations on emissions and lubricant disposal demand a reduction in sulfur and phosphorus content of lubricants. The desired lubricant will be environmentally benign, perhaps only consisting of a mineral or polyalphaolefin base stock. Another trend is toward the use of vegetable oils or other bio-based lubricants. The results of Chapter 2 indicated that an iron oxide thin film will form on the contacting surfaces of steel rolling element bearings, the nature of which is determined by the severity of the lubrication conditions and condition of the lubricant. Future research should be conducted to better understand the mechanisms of natural oxide formation under temperature, pressure, and shear conditions that are relevant to rolling element bearing applications. This could be done by performing experiments on a ball-on-disk tribology tester, and carefully controlling the temperature, pressure, rolling speed, slide-to-roll ratio, and oxidation state of the lubricant. Cross-sectional TEM studies of FIB samples from the test disk surfaces would allow for quantification of the oxidation kinetics as a function of the test variables. Additional useful studies would include

examining the effect of steel type (including high-performance carburizable stainless steels), near-surface materials treatments including vibrational finishing or ion implantation, and traction conditions on the near-surface material durability.

7.2.2 Mechanisms of Lubricant Additive Interactions with Surfaces

Although the trend is toward eliminating the use of S-P additives in automotive and industrial lubricants, such additives are still critical to the performance of certain gearing applications. The studies in Chapter 3 did not indicate any corrosion damage or clues about why certain S-P additives can be detrimental to bearing fatigue life. Additional bearing tests with S-P additives should be conducted to fatigue life durations, followed by cross-sectional surface analysis using TEM of FIB samples to search for evidence of nanometer-scale chemical wear or material degradation. In addition, a broader range of bearing test conditions should be evaluated with lubricants containing S-P additives. Traction tests should be conducted with additive blends to evaluate the possibility of sliding or skidding in rolling element bearings operating with lubricants containing S-P lubricant additives. Commercially-available additive formulations with unknown chemical constituents were evaluated in Chapter 3 for engineering relevance. However, further studies should be conducted with known blends of additive chemicals to evaluate and isolate mechanisms of additive action. Caution must be practiced in using this approach because additive synergies are known to be substantial and single chemical studies can be misleading. New additive chemistries are being developed to replace or supplement S-P additives and their mechanisms of action and effects on steel surface durability should be the subject of future investigations.

7.2.3 Other Topics Related to Nanocomposite Tribological Thin Films

As shown in Chapters 4, 5, and 6, the growth of MC/a-C:H thin films during reactive sputter deposition is a dynamic process relying on many concurrent mechanisms for film composition and structure development. Additional experiments should be performed to further study the atomistic mechanisms of nucleation and growth of metal carbide crystallites during deposition. "Single-pass" deposition experiments and *ex situ* TEM investigations were performed as part of the present work without success. Future experiments should rely on *in situ* analysis of the film growth front. Deposition experiments with substrate temperature control should be performed to evaluate the influence of substrate temperature on crystallite size and compressive stress development at high ion bombardment energies with substrate carousel rotation. An atomically-abrupt crystallite/matrix interface and control over crystallite separation (i.e., matrix width between crystallites) are critical features of super-hard nanocomposite materials such as nc-TiN/Si_3N_4 that enable the attainment of "super-hardness" – hardness in excess of the rule of mixture predictions. Super-hardness has not been observed widely in MC/a-C:H films, probably because of limited control over crystallite separation distances and a semi-diffuse interface between the carbide and amorphous hydrocarbon phases (i.e., some trace dissolution of metal in the a-C:H phase). Experiments could be conducted to determine if super-hard MC/a-C:H films can be deposited in an industrially-relevant, economical way. Atom probe field ion microscopy would be valuable for studying the three-dimensional structure of the films with atomic resolution, including the diffusivity of the crystallite-matrix interfaces. This technique works by applying transient high-voltage pulses to a needle-shaped specimen at low temperatures resulting in field

evaporation and detection by a phosphor screen or mass spectrometer. The data can be constructed into a three-dimensional image of the sample with atomic-level resolution. This technique has been used thus far to study the segregation of atoms in metals and the composition of nanometer-scale precipitates.

CHAPTER 8

BIBLIOGRAPHY

G. Adamopoulos, J. Robertson, N. A. Morrison, and C. Godet: Hydrogen content estimation of hydrogenated amorphous carbon by visible Raman spectroscopy. *J. Appl. Phys.* **96**, 6348 (2004).

A. W. Adamson and A. P. Gast: *Physical Chemistry of Surfaces*, 6th ed. (John Wiley & Sons, New York, 1997).

G. Altshuller: *The Innovation Algorithm: TRIZ, Systematic Innovation and Technical Creativity*. (Technical Innovation Center, Worcester, MA, 2000).

J. C. Angus: Empirical categorization and naming of "diamond-like" carbon films. *Thin Solid Films* **142**, 145 (1986).

J. C. Angus and C. C. Hayman: Low-pressure, metastable growth of diamond and diamondlike phases. *Science* **241**, 913 (1988).

J. C. Angus and F. Jansen: Dense "diamondlike" hydrocarbons as random covalent networks. *J. Vac. Sci. Tech. A* **6**, 1778 (1988).

T. R. Anthony: Stresses generated by impurities in diamond. *Diam. Relat. Mater.* **4**, 1346 (1995).

D. Babonneau, T. Cabioc'h, A. Naudon, J. C. Girard, and M. F. Denanot: Silver nanoparticles encapsulated in carbon cages obtained by co-sputtering of the metal and graphite. *Surf. Sci.* **409**, 358 (1998).

Balzers Balinit Product Catalog. (Balzers AG, Liechtenstein, 1991).

A. W. Batchelor, G. W. Stachowiak, and A. Cameron: The relationship between oxide films and the wear of steels. *Wear* **113,** 203 (1986).

R. O. Bejerk: Oxygen – an 'extreme-pressure agent'. *ASLE Trans.* **16**, 97 (1973).

P. Bellon and R. S. Averback: Preface to viewpoint set on: materials under driving forces. *Scr. Mater.* **49**, 921 (2003).

C. Benndorf, M. Grischke, H. Koeberle, R. Memming, A. Brauer, and F. Thieme: Identification of carbon and tantalum chemical states in metal-doped a-C:H films. *Surf. Coat. Tech.* **36**, 171 (1988).

E. Bergmann and J. Vogel: Tribological properties of metal/carbon coatings. *J. Vac. Sci. Tech. A* **4**, 2867 (1986).

E. Bergmann and J. Vogel: Influence of composition and process parameters on the internal stress of the carbides of tungsten, chromium, and titanium. *J. Vac. Sci. Tech. A* **5**, 70 (1987).

K. Bewilogua, C. V. Cooper, C. Specht, J. Schroder, R. Wittorf, and M. Grischke: Erratum to: "Effect of target material on deposition and properties of metal-containing DLC (Me-DLC) coatings". *Surf. Coat. Tech.* **132**, 275 (2000).

K. Bewilogua and H. Dimigen: Preparation of W-C:H coatings by reactive magnetron sputtering. *Surf. Coat. Tech.* **61**, 144 (1993).

V. Bhargava, G. T. Hahn, and C. A. Rubin: Rolling contact deformation and microstructural changes in high strength bearing steel. *Wear* **133**, 65 (1989).

A. F. Bower and K. L. Johnson: The influence of strain hardening on cumulative plastic deformation in rolling and sliding line contact. *J. Mech. Phys. Solids* **37**, 471 (1989).

W. F. Bowman and G. W. Stachowiak: The effect of base oil oxidation on scuffing. *Tribol. Lett.* **4**, 59 (1998).

P. V. Brande, S. Lucas, R. Winand, L. Renard, and A. Weymeersch: Study of the formation of a carbon layer on a sputtering target during magnetron-enhanced reactive sputtering. *Surf. Coat. Tech.* **61**, 151 (1993).

W. A. Brantley: Calculated elastic constants for stress problems associated with semiconductor devices. *J. Appl. Phys.* **44**, 534 (1973).

C. Brin, J. P. Riviere, J. P. Eymery, and J. P. Villain: Structural characterization of wear debris produced during friction between two austenitic stainless steel antagonists. *Tribol. Lett.* **11**, 127 (2001).

J. J. Bush, W. L. Grube, and G. H. Robinson: Microstructural and residual stress changes in hardened steel due to rolling contact. *ASM Trans.* **54**, 390 (1961).

M. K. Chaudhury: Interfacial interaction between low-energy surfaces. *Mater. Sci. Eng. R* **16**, 97 (1996).

Y. T. Cheng and C. M. Cheng: Scaling, dimensional analysis, and indentation measurements. *Mater. Sci. Eng. R* **44**, 91 (2004).

C. C. Chou and J. F. Lin: A new approach to the effect of EP additive and surface roughness on the pitting fatigue of a line-contact system. *ASME J. Tribol.* **124**, 245 (2002).

J. J. Cuomo, D. L. Pappas, J. Bruley, J. P. Doyle, and K. L. Saenger: Vapor deposition processes for amorphous carbon films with sp³ fractions approaching diamond. *J. Appl. Phys.* **70**, 1706 (1991).

E. C. Cutiongco and Y. W. Chung: Prediction of scuffing failure based on competitive kinetics of oxide formation and removal: Application to lubricated sliding of AISI 52100 steel on steel. *Tribol. Trans.* **37**, 622 (1994).

A. Czyzniewski: Deposition and some properties of nanocrystalline WC and nanocomposite WC/a-C:H coatings. *Thin Solid Films* **433**, 180 (2003).

C. A. Davis: A simple model for the formation of compressive stress in thin films by ion bombardment. *Thin Solid Films* **226**, 30 (1993).

F. M. d'Heurle and J. M. E. Harper: Note on the origin of intrinsic stresses in films deposited via evaporation and sputtering. *Thin Solid Films* **171**, 81 (1989).

H. Dimigen and H. Hubsch: Applying low-friction wear-resistant thin solid films by physical vapour deposition. *Philips Tech. Review* **41**, 186 (1983).

H. Dimigen and H. Hubsch: Carbon-containing sliding layer. US Patent #4,525,417 (Jun. 25, 1985).

H. Dimigen, H. Hubsch, and R. Memming: Tribological and electrical properties of metal-containing hydrogenated carbon films. *Appl. Phys. Lett.* **50**, 1056 (1987).

H. Dimigen and C. P. Klages: Microstructure and wear behavior of metal-containing diamond-like coatings. *Surf. Coat. Tech.* **49**, 543 (1991).

S. P. Dodd, M. Cankurtaran, and B. James: Ultrasonic determination of the elastic and nonlinear acoustic properties of transition-metal carbide ceramics: TiC and TaC. *J. Mater. Sci.* **38**, 1107 (2003).

G. L. Doll: Internal memo. (The Timken Company, Canton, OH, Mar. 5, 2002).

G. L. Doll, R. D. Evans, and S. P. Johnson: Providing oil-out protection to rolling element bearings with coatings, in *48th Annual Technical Conference Proceedings*. (Society of Vacuum Coaters, Denver, CO, Apr. 23-28, 2005).

G. L. Doll and B. K. Osborn: Engineering surfaces of precision steel components, in *44th Annual Technical Conference Proceedings*. (Society of Vacuum Coaters, Philadelphia, PA, Apr. 21-26, 2001).

G. L. Doll, C. R. Ribaudo, and R. D. Evans: Engineered surfaces for steel rolling element bearings and gears, in *Materials Science & Technology Conference Proceedings* **2.** (New Orleans, LA, Sept. 26-29, 2004).

W. E. Dowling, Jr., W. T. Donlon, W. B. Copple, and C. V. Darragh: The influence of heat treat process and alloy on the surface microstructure and fatigue strength of carburized alloy steel. *SAE Tech. Paper Ser.* 1999-01-0600 (1999).

D. Dowson and G. R. Higginson: *Elasto-hydrodynamic Lubrication.* (Pergamon Press, Oxford, 1977).

R. D. Evans, E. P. Cooke, C. R. Ribaudo, and G. L. Doll: Nanocomposite tribological coatings for rolling element bearings, in *Surface Engineering 2002 – Synthesis, Characterization and Applications*, edited by A. Kumar, W. J. Meng, Y. T. Cheng, J. S. Zabinski, G. L. Doll, and S. Veprek. (Mater. Res. Soc. Symp. **750**, Warrendale, PA, 2003).

R. D. Evans, G. L. Doll, and J. T. Glass: Relationships between the thermal stability, friction, and wear properties of reactively sputtered Si-aC:H thin films. *J. Mater. Res.* **17**, 2888 (2002).

R. D. Evans, G. L. Doll, P. W. Morrison Jr., J. Bentley, K. L. More, and J. T. Glass: The effects of structure, composition, and chemical bonding on the mechanical properties of Si-aC:H thin films. *Surf. Coat. Tech.* **157**, 197 (2002).

R. D. Evans, J. Y. Howe, J. Bentley, G. L. Doll, and J. T. Glass: Influence of deposition parameters on the composition and structure of reactively sputtered nanocomposite TaC/a-C:H thin films. *J. Mater. Res.* **20**, 2583 (2005).

R. D. Evans, K. L. More, C. V. Darragh, and H. P. Nixon: Transmission electron microscopy of boundary-lubricated bearing surfaces. Part I: Mineral oil lubricant. *Tribol. Trans.* **47**, 430 (2004).

R. D. Evans, K. L. More, C. V. Darragh, and H. P. Nixon: Transmission electron microscopy of boundary-lubricated bearing surfaces. Part II: Mineral oil lubricant with sulfur- and phosphorus-containing gear oil additives. *Tribol. Trans.* **48**, 299 (2005).

R. S. Fein: Boundary lubrication relations, in *Tribology Data Handbook*, edited by E. R. Booser. (CRC Press, New York, 1997).

R. S. Fein and K. L. Kreuz: Chemistry of boundary lubrication of steel by hydrocarbons. *ASLE Trans.* **8**, 29 (1965).

B. Feng, D. M. Cao, W. J. Meng, L. E. Rehn, P. M. Baldo, and G. L. Doll: Probing for mechanical and tribological anomalies in the TiC/amorphous hydrocarbon nanocomposite coating system. *Thin Solid Films* **398**, 210 (2001).

A. C. Ferrari, B. Kleinsorge, N. A. Morrison, A. Hart, V. Stolojan, and J. Robertson: Stress reduction and bond stability during thermal annealing of tetrahedral amorphous carbon. *J. Appl. Phys.* **85**, 7191 (1999).

A. C. Ferrari and J. Robertson: Interpretation of Raman spectra of disordered and amorphous carbon. *Phys. Rev. B* **61**, 14095 (2000).

A. J. Gellman and N. D. Spencer: Surface chemistry in tribology. *Proc. I. Mech. E. Ser. J.* **216**, 443 (2002).

K. W. Gerstenberg and M. Grischke: Thermal gas evolution studies on a-C:H:Ta films. *J. Appl. Phys.* **69**, 736 (1991).

A. E. Giannakopoulos, T. A. Venkatesh, T. C. Lindley, and S. Suresh: The role of adhesion in contact fatigue. *Acta. Mater.* **47**, 4653 (1999).

L. A. Girifalco and R. J. Good: A theory for the estimation of surface and interfacial energies. I. Derivation and application to interfacial tension. *J. Phys. Chem.* **61**, 904 (1957).

D. Godfrey: Iron oxides and rust (hydrated iron oxides) in tribology. *Lub. Eng.* **55**, 33 (1999).

B. J. Griffiths: Mechanisms of white layer generation with reference to machining and deformation processes. *J. Tribol.* **109**, 525 (1987).

A. Grill, B. S. Meyerson, V. V. Patel, J. A. Reimer, and M. A. Petrich: Inhomogeneous carbon bonding in hydrogenated amorphous carbon films. *J. Appl. Phys.* **61**, 2874 (1987).

M. Grischke, K. Bewilogua, and H. Dimigen: Preparation, properties and structure of metal containing amorphous hydrogenated carbon films. *Mater. Manuf. Process.* **8**, 407 (1993).

M. Grischke, A. Hieke, F. Morgenweck, and H. Dimigen: Variation of the wettability of DLC-coatings by network modification using silicon and oxygen. *Diam. Relat. Mater.* **7**, 454 (1998).

G. R. Gruzalski and D. M. Zehner: Defect states in substoichiometric tantalum carbide. *Phys. Rev. B* **34**, 3841 (1986).

S. Haizuka, R. Nemoto, and C. Naruse: Study on limiting load for scuffing and specific wear of spur gears (effects of lubricating oil and tooth form). *JSME Int. J. – Ser. C* **38**, 149 (1995).

G. Hakansson, I. Petrov, and J. E. Sundgren: Growth of TaC thin films by reactive direct current magnetron sputtering: composition and structure. *J. Vac. Sci. Tech. A* **8**, 3769 (1990).

M. Hans, R. Buchel, M. Grischke, R. Hobi, and M. Zach: High-volume PVD coating of precision components of large volumes at low process costs. *Surf. Coat. Tech.* **123**, 288 (2000).

S. J. Harris and A. M. Weiner: Scaling relationships for the abrasion of steel by diamondlike carbon coatings. *Wear* **223**, 31 (1998).

T. A. Harris: *Rolling Bearing Analysis*, 2nd ed. (John Wiley & Sons, New York, 1984).

H. He and M. F. Thorpe: Elastic properties of glasses. *Phys. Rev. Lett.* **54**, 2107 (1985).

J. P. Hirvonen, J. Koskinen, M. Kaukonen, R. Nieminen, and H. J. Scheibe: Dynamic relaxation of the elastic properties of hard carbon films. *J. Appl. Phys.* **81**, 7248 (1997).

D. Hofmann, H. Schuessler, K. Bewilogua, H. Hubsch, and J. Lemke: Plasma-booster-assisted hydrogenated W-C coatings. *Surf. Coat. Tech.* **73**, 137 (1995).

H. S. Hong, M. E. Huston, B. M. O'Connor, and N. M. Stadnyk: Evaluation of surface fatigue performance of gear oils. *Lubri. Sci.* **10**, 365 (1998).

R. G. Horn: Measurement of Surface Forces and Adhesion, in *ASM Handbook: Vol. 18 - Friction, Lubrication, and Wear Technology*. (ASM International, 1992).

S. M. Hsu and E. E. Klaus: Some chemical effects in boundary lubrication Part I: Base oil-metal interaction. *ASLE Trans.* **22**, 135 (1977).

W. Jacob: Surface reactions during growth and erosion of hydrocarbon films. *Thin Solid Films* **326**, 1 (1998).

S. C. Kang and K. C. Ludema: The 'breaking-in' of lubricated surfaces. *Wear* **108**, 375 (1986).

M. Kasrai, M. S. Fuller, G. M. Bancroft, E. S. Yamaguchi, and P. R. Ryason: X-ray absorption study of the effect of calcium sulfonate on antiwear film formation generated from neutral and basic ZDDPs: Part 1 – phosphorus species. *Tribol. Trans.* **46**, 534 (2003).

M. Kasrai, M. S. Fuller, G. M. Bancroft, E. S. Yamaguchi, and P. R. Ryason: X-ray absorption study of the effect of calcium sulfonate on antiwear film formation generated from neutral and basic ZDDPs: Part 2 – sulfur species. *Tribol. Trans.* **46**, 543 (2003).

K. Kato: Wear in boundary or mixed lubrication regimes, in *Boundary and Mixed Lubrication: Science and Applications*, edited by D. Dowson, G. Dalmaz, and A. Lubrecht. (Elsevier Science, Amsterdam, 2002).

C. P. Klages and R. Memming: Microstructure and physical properties of metal-containing hydrogenated carbon films. *Mater. Sci. Forum* **52 & 53**, 609 (1989).

H. P. Klug and L. E. Alexander: *X-ray diffraction procedures for polycrystalline and amorphous materials*, 2nd ed. (John Wiley & Sons, New York, 1974).

O. Knotek, R. Elsing, G. Kramer, and F. Jungblut: On the origin of compressive stress in PVD coatings – an explicative model. *Surf. Coat. Tech.* **46**, 265 (1991).

K. Komvopoulos, V. Chiaro, B. Pakter, E. S. Yamaguchi, and P. R. Ryason: Antiwear tribofilm formation on steel surfaces lubricated with gear oil containing borate, phosphorus, and sulfur additives. *Tribol. Trans.* **45**, 568 (2002).

H. Kong, E. S. Yoon, and O. K. Kwon: Self-formation of protective oxide films at dry sliding mild steel surfaces under a medium vacuum. *Wear* **181-183**, 325 (1995).

I. I. Kudish, and K. W. Burris: Modern state of experimentation and modeling in contact fatigue phenomenon: Part I—Contact fatigue. *Tribol. Trans.* **43**, 187 (2000).

V. Y. Kulikovsky, F. Fendrych, L. Jastrabik, and D. Chvostova: Study of formation and some properties of Ti-C:H films prepared by d.c. magnetron sputtering. *Surf. Coat. Tech.* **91**, 122 (1997).

V. Kulikovsky, A. Tarasenko, F. Fendrych, L. Jastrabik, D. Chvostova, F. Franc, and L. Soukup: The mechanical, tribological and optical properties of Ti-C:H coatings, prepared by dc magnetron sputtering. *Diam. Relat. Mater.* **7**, 774 (1998).

A. Leyland and A. Matthews: On the significance of the H/E ratio in wear control: a nanocomposite coating approach to optimised tribological behavior. *Wear* **246**, 1 (2000).

D. R. Lide, ed.: *CRC Handbook of Chemistry and Physics*, 81st ed. (CRC Press, Boca Raton, FL, 2000).

M. A. Lieberman and A. J. Lichtenberg: *Principles of Plasma Discharges and Materials Processing.* (John Wiley & Sons, New York, 1994).

Y. Lifshitz: Diamond-like carbon—present status. *Diam. Relat. Mater.* **8**, 1659 (1999).

Y. Lifshitz, S. R. Kasi, J. W. Rabalais, and W. Eckstein: Subplantation model for film growth from hyperthermal species. *Phys. Rev. B* **41**, 10468 (1990).

W. E. Littmann, R. L. Widner, J. O. Wolfe, and J. D. Stover: The role of lubrication in propagation of contact fatigue cracks. *J. Tribol.* **90**, 89 (1968).

S. Logothetidis, E. I. Meletis, and G. Kourouklis: New approach in the monitoring and characterization of titanium nitride thin films. *J. Mater. Res.* **14,** 436 (1999) 436-441.

C. Longching, C. Qing, and S. Eryu: Study on initiation and propagation angles of subsurface cracks in GCr15 bearing steel under rolling contact. *Wear* **133**, 205 (1989).

K. C. Ludema: A review of scuffing and running-in of lubricated surfaces, with asperities and oxides in perspective. *Wear* **100**, 315 (1984).

J. F. Lynch, C. G. Ruderer, and W. H. Duckworth, eds: *Engineering Properties of Selected Ceramic Materials.* (American Ceramic Society, Columbus, OH, 1966).

M. E. Mack, Wafer cooling and wafer charging in ion implantation, in *Handbook of Ion Implantation Technology*, J. F. Ziegler, ed. (Elsevier, Amsterdam, 1992).

D. Mann: *Hands-On Systematic Innovation.* (Creax, Belgium, 2002).

J. A. Martin, S. F. Borgese, and A. D. Eberhardt: Microstructural alterations of rolling bearing steel undergoing cyclic stressing. *J. Basic Eng.* **88**, 555 (1966).

J. M. Martin: Antiwear mechanisms of zinc dithiophosphate: a chemical hardness approach. *Tribol. Lett.* **6**, 1 (1999).

J. M. Martin, C. Grossiord, T. L. Mogne, S. Bec, and A. Tonck: The two-layer structure of Zndtp tribofilms Part I: AES, XPS and XANES analysis. *Tribol. Int.* **34**, 523 (2001).

D. M. Mattox: *Handbook of Physical Vapor Deposition (PVD) Processing.* (Noyes Publications, New Jersey, 1998).

W. J. Meng, T. J. Curtis, L. E. Rehn, and P. M. Baldo: Plasma-assisted deposition and characterization of Ti-containing diamondlike carbon coatings. *J. Appl. Phys.* **83**, 6076 (1998).

W. J. Meng and B. A. Gillispie: Mechanical properties of Ti-containing and W-containing diamond-like carbon coatings. *J. Appl. Phys.* **84**, 4314 (1998).

213

W. J. Meng, E. I. Meletis, L. E. Rehn, and P. M. Baldo: Inductively coupled plasma assisted deposition and mechanical properties of metal-free and Ti-containing hydrocarbon coatings. *J. Appl. Phys.* **87**, 2840 (2000).

W. J. Meng, R. C. Tittsworth, J. C. Jiang, B. Feng, D. M. Cao, K. Winkler, and V. Palshin: Ti atomic bonding environment in Ti-containing hydrocarbon coatings. *J. Appl. Phys.* **88**, 2415 (2000).

W. J. Meng, R. C. Tittsworth, and L. E. Rehn: Mechanical properties and microstructure of TiC/amorphous hydrocarbon nanocomposite coatings. *Thin Solid Films* **377**, 222 (2000).

D. P. Monaghan, D. G. Teer, P. A. Logan, I. Efeoglu, and R. D. Arnell: Deposition of wear resistant coatings based on diamond like carbon by unbalanced magnetron sputtering. *Surf. Coat. Tech.* **60**, 525 (1993).

D. G. Montgomery: *Design and Analysis of Experiments*, 5th ed. (John Wiley & Sons, 2001).

R. S. Montgomery: Run-in and glaze formation on gray cast iron surfaces. *Wear* **14**, 99 (1969).

K. L. More, D. W. Coffey, B. A. Pint, K. S. Trent, and P. F. Tortorelli: TEM specimen preparation of oxidized Ni-base alloys using the focused ion beam (FIB) technique, in *Proc. of Microscopy and Microanalysis*. (Philadelphia, PA, 2000).

A. Muroga and H. Saka: Analysis of rolling contact fatigued microstructure using focused ion beam sputtering and transmission electron microscopy observation. *Scr. Metall. Mater.* **33**, 151 (1995).

K. S. Murphy, K. L. More, and M. J. Lance: As-deposited mixed zone in thermally grown oxide beneath a thermal barrier coating. *Surf. Coat. Tech.*, **146-147**, 152 (2001).

D. Nir: Summary abstract: Energy dependence of the stress in diamondlike carbon films. *J. Vac. Sci. Technol. A* **4**, 2954 (1986).

NIST X-ray Photoelectron Spectroscopy Database, NIST Standard Reference Database 20, Version 3.4 (Web Version), 2003.

H. P. Nixon and H. Zantopulos: Lubricant additives, friend or foe what the equipment designer needs to know. *Lubr. Eng.* 815 (Oct. 1995).

M. Ohring: *The Materials Science of Thin Films.* (Academic Press, Boston, 1992).

W. C. Oliver and G. M. Pharr: An improved technique for determining hardness and elastic modulus using load and displacement sensing indentation experiments. *J. Mater. Res.* **7**, 1564 (1992).

M. H. F. Overwijk, F. C. van den Heuvel, and C. W. T. Bulle-Lieuwma: Novel scheme for the preparation of transmission electron microscopy specimens with a focused ion beam. *J. Vac. Sci. Technol. B* **11**, 2021 (1993).

D. P. Palicki and A. Matthews: Recent developments in magnetron sputtering systems. *Finishing* (Nov. 1993) p. 36.

S. J. Park, K. R. Lee, D. H. Ko, and K. Y. Eun: Microstructure and mechanical properties of WC-C nanocomposite films. *Diam. Relat. Mater.* **11**, 1747 (2002).

J. Patscheider, T. Zehnder, and M. Diserens: Structure-performance relations in nanocomposite coatings. *Surf. Coat. Tech.* **146**, 201 (2001).

B. Paul: Prediction of elastic constants of multiphase materials. *Trans. AIME* **218**, 36 (1960).

M. B. Peterson and W. O. Winer: *Wear Control Handbook.* (American Society of Mechanical Engineers, 1980).

J. C. Phillips: Topology of covalent non-crystalline solids I: Short-range order in chalcogenide alloys. *J. Non-Cryst. Solids* **34**, 153 (1979).

M. R. Phillips and T. F. J. Quinn: The effect of surface roughness and lubricant film thickness on the contact fatigue life of steel surfaces lubricated with a sulfur-phosphorus type of extreme pressure additive. *Wear* **51**, 11 (1978).

H. O. Pierson: *Handbook of refractory carbides and nitrides – properties, characteristics, processing and applications.* (Noyes Publications, Westwood, New Jersey, 1996).

I. A. Polonsky, T. P. Chang, L. M. Keer, and W. D. Sproul: A study of rolling-contact fatigue of bearing steel coated with physical vapor deposition TiN films: Coating response to cyclic contact stress and physical mechanisms underlying coating effect on the fatigue life. *Wear* **215**, 191 (1998).

W. Precht and A. Czyzniewski: Deposition and some properties of carbide/amorphous carbon nanocomposites for tribological application. *Surf. Coat. Tech.* **174**, 979 (2003).

B. H. Pruitt: *Timken: From Missouri to Mars - A century of leadership in manufacturing.* (Harvard Business School Press, Boston, 1998).

E. Rabinowicz: *Friction and Wear of Materials.* (John Wiley & Sons, New York, 1965).

W. M. Rainforth, A. J. Leonard, C. Perrin, A. Bedolla-Jacuinde, Y. Wang, H. Jones, and Q. Luo: High resolution observations of friction-induced oxide and its interaction with the worn surface. *Tribol. Int.* **35**, 731 (2002).

A. A. Rempel and A. K. Sinelnichenko: X-ray photoelectron spectra of nonstoichiometric tantalum carbide. *Phys. Metals* **11**, 352 (1992).

D. A. Rigney: Large strains associated with sliding contact of metals. *Mater. Res. Innovat.* **1**, 231 (1998).

J. Robertson: Mechanical properties and coordinations of amorphous carbons. *Phys. Rev. Lett.* **68**, 220 (1992).

J. Robertson: Deposition mechanisms for promoting sp^3 bonding in diamond-like carbon. *Diam. Relat. Mater.* **2**, 984 (1993).

J. Robertson: The deposition mechanism of diamond-like a-C and a-C:H. *Diam. Relat. Mater.* **3**, 361 (1994).

J. Robertson: Diamond-like amorphous carbon. *Mater. Sci. Eng. R* **37**, 129 (2002).

J. Robertson: Mechanism of sp^3 bond formation in the growth of diamond-like carbon. *Diam. Relat. Mater.* **14**, 942 (2005).

F. G. Rounds: Some effects of additives on rolling contact fatigue. *ASLE Trans.* **10**, 243 (1967).

F. G. Rounds: Influence of steel composition on additive performance. *ASLE Trans.* **15**, 54 (1972).

I. Safi: Recent aspects concerning DC reactive magnetron sputtering of thin films: a review. *Surf. Coat. Tech.* **127**, 203 (2000).

T. Saito, Y. Imada, K. Sugita, and F. Honda: Tribological study of chemical states of protective oxide film formed on steel after sliding in humid atmosphere and in aqueous solutions. *J. Tribol.* **119**, 613 (1997).

E. Sauger, L. Ponsonnet, J. M. Martin, and L. Vincent: Study of the tribologically transformed structure created during fretting tests. *Tribol. Int.* **33**, 743 (2000).

K. I. Schiffmann, M. Fryda, G. Goerigk, R. Lauer, P. Hinze, and A. Bulack: Sizes and distances of metal clusters in Au-, Pt-, W- and Fe-containing diamond-like carbon hard coatings: a comparative study by small angle x-ray scattering, wide angle x-ray

diffraction, transmission electron microscopy and scanning tunnelling microscopy. *Thin Solid Films* **347**, 60 (1999).

J. Schofer, P. Rehbein, U. Stolz, D. Lohe, and K. H. Zum Gahr: Formation of tribochemical films and white layers on self-mated bearing steel surfaces in boundary lubricated sliding contact. *Wear* **248**, 7 (2001).

B. Shi and W. J. Meng: Intrinsic stresses and mechanical properties of Ti-containing hydrocarbon coatings. *J. Appl. Phys.* **94**, 186 (2003).

B. Shi, W. J. Meng and T. L. Daulton: Thermal expansion of Ti-containing hydrogenated amorphous carbon nanocomposite thin films. *Appl. Phys. Lett.* **85**, 4352 (2004).

B. Shi, W. J. Meng, and R. D. Evans: Characterization of high temperature deposited Ti-containing hydrogenated carbon thin films. *J. Appl. Phys.* **96**, 7705 (2004).

B. Shi, W. J. Meng, L. E. Rehn, and P. M. Baldo: Intrinsic stress development in Ti-C:H ceramic nanocomposite coatings. *Appl. Phys. Lett.* **81**, 352 (2002).

S. Shirahama, M. Miyajima, and A. Okamura: Influence of phosphorus additives on rolling fatigue. *Jpn. J. Tribol.* **46**, 193 (2001).

S. Shirahama and J. Nakamura: Influence of sulfur-type additives on rolling fatigue. *Jpn. J. Tribol.* **46**, 205 (2001).

H. Sjostrom, L. Hultman, J. E. Sundgren, and L. R. Wallenberg: Microstructure of amorphous C:H and metal-containing C:H films deposited on steel substrates. *Thin Solid Films* **232**, 169 (1993).

H. Sjostrom and V. Wikstrom: Diamond-like carbon coatings in rolling contacts. *Proc. Instn. Mech. Engrs. Part J* **215**, 545 (2001).

D. L. Smith: *Thin Film Deposition: Principles and Practice*. (McGraw Hill, Boston, 1995).

G. C. Smith, A. B. Hopwood, and K. J. Titchener: Microcharacterization of heavy-duty diesel engine piston deposits. *Surf. Interf. Anal.* **33**, 259 (2002).

H. Spikes: The history and mechanisms of ZDDP. *Tribol. Lett.* **17**, 469 (2004).

C. Strondl, N. M. Carvalho, J. Th. M. De Hosson, and T. G. Krug: Influence of energetic ion bombardment on W-C:H coatings deposited with W and WC targets. *Surf. Coat. Tech.* **200**, 1142 (2005).

C. Strondl, N. M. Carvalho, J. Th. M. De Hosson, and G. J. van der Kolk: Investigation on the formation of tungsten carbide in tungsten-containing diamond like carbon coatings. *Surf. Coat. Tech.* **162**, 288 (2003).

C. Strondl, G. J. van der Kolk, T. Hurkmans, W. Fleischer, T. Trinh, N. M. Carvalho, and J. Th. M. de Hosson: Properties and characterization of multilayers of carbides and diamond-like carbon. *Surf. Coat. Tech.* **142**, 707 (2001).

H. Swahn, P. C. Becker, and O. Vingsbo: Martensite decay during rolling contact fatigue in ball bearings. *Metall. Trans. A* **7A,** 1099 (1976).

M. A. Tamor and W. C. Vassell: Raman "fingerprinting" of amorphous carbon films. *J. Appl. Phys.* **76**, 3823 (1994).

D. G. Teer: Magnetron sputter ion plating. US Patent #5,556,519 (Sep. 17, 1996).

J. A. Thornton: The microstructure of sputter-deposited coatings. *J. Vac. Sci. Technol. A* **4**, 3059 (1986).

M. F. Thorpe: Continuous deformations in random networks. *J. Non-Cryst. Solids* **57**, 355 (1983).

A. A. Torrance, J. E. Morgan, and G. T. Y. Wan: An additive's influence on the pitting and wear of ball bearing steel. *Wear* **192**, 66 (1996).

T. Y. Tsui, W. C. Oliver, and G. M. Pharr: Influences of stress on the measurement of mechanical properties using nanoindentation: Part I. Experimental studies in an aluminum alloy. *J. Mater. Res.* **11**, 752 (1996).

W. van Duyn and B. van Lochem: Chemical and mechanical characterization of WC:H amorphous layers. *Thin Solid Films* **181**, 497 (1989).

K. Varlot, M. Kasrai, J. M. Martin, B. Vacher, G. M. Bancroft, E. S. Yamaguchi, and P. R. Ryason: Antiwear film formation of neutral and basic ZDDP: influence of the reaction temperature and of the concentration. *Tribol. Lett.* **8**, 9 (2000).

J. A. Venables, G. D. T. Spiller, and M. Hanbucken: Nucleation and growth of thin films. *Rep. Prog. Phys.* **47**, 399 (1984).

S. Veprek: Electronic and mechanical properties of nanocrystalline composites when approaching molecular size. *Thin Solid Films* **297**, 145 (1997).

P. Villiger, Ch. Sprechter, and J. A. Peters: Parameter optimization of Ti-DLC coatings using statistically based methods. *Surf. Coat. Tech.* **116-119**, 585 (1999).

A. A. Voevodin, J. P. O'Neill, and J. S. Zabinski: Tribological performance and tribochemistry of nanocrystalline WC/amorphous diamond-like carbon composites. *Thin Solid Films* **342**, 194 (1999).

A. von Keudell, M. Meier, and C. Hopf: Growth mechanism of amorphous hydrogenated carbon. *Diam. Relat. Mater.* **11**, 969 (2002).

A. von Keudell, T. Schwarz-Selinger, and W. Jacob: Simultaneous interaction of methyl radicals and atomic hydrogen with amorphous hydrogenated carbon films. *J. Appl. Phys.* **89**, 2979 (2001).

A. P. Voskamp: Material response to rolling contact loading. *J. Tribol.* **107**, 359 (1985).

A. P. Voskamp, R. Osterlund, P. C. Becker, and O. Vingsbo: Gradual changes in residual stress and microstructure during contact fatigue in ball bearings. *Met. Technol.* **7**, 14 (1980).

W. Wagner, F. Rauch, and M. Grischke: Stoichiometry of a-C:H(Ta) films determined by means of RBS and the 15N technique. *Nuc. Inst. Meth. Phys. Res. B* **111**, 111 (1996).

G. T. Y. Wan, E. V. Amerongen, and H. Lankamp: Effect of extreme-pressure additives on fatigue life of rolling bearings. *J. Phys. D: Appl. Phys.* **25**, A147 (1992).

R. Wang, C. Mercer, A. G. Evans, C. V. Cooper, and H. K. Yoon: Delamination and spalling of diamond-like carbon tribological surfaces. *Diam. Relat. Mater.* **11**, 1797 (2002).

Y. Wang, J. E. Fernandez, and D. G. Cuervo: Rolling contact fatigue lives of steel AISI 52100 balls with eight mineral and synthetic lubricants. *Wear* **196**, 110 (1996).

Y. Wang, C. Q. Gao, T. C. Lei, and H. X. Lu: Amorphous structure of worn surface in 52100 steel. *Scr. Metall.* **22**, 1251 (1988).

Y. Wang, T. C. Lei, and C. Q. Gao: An observation of a filiform wear product in bearing steel 52100. *Wear* **134**, 231 (1989).

O. L. Warren, J. F. Graham, P. R. Norton, J. E. Houston, and T. A. Michalske: Nanomechanical properties of films derived from zinc dialkyldithiophoshpate. *Tribol. Lett.* **4**, 189 (1998).

R. Wei, P. J. Wilbur, M. J. Liston, and G. Lux: Rolling-contact-fatigue wear characteristics of diamond-like hydrocarbon coatings on steels. *Wear* **162-164**, 558 (1993).

D. R. Wheeler and D. H. Buckley: Texturing in metals as a result of sliding. *Wear* **33**, 65 (1975).

R. L. Widner, ed.: Failures of Rolling Element Bearings, in *Metals Handbook: Failure Analysis and Prevention, vol. 11*, 9th ed. (American Society for Metals, Metals Park, OH, 1986).

H. Windischmann: An intrinsic stress scaling law for polycrystalline thin films prepared by ion beam sputtering. *J. Appl. Phys*. **62**, 1800 (1987).

H. A. Wriedt: Iron-Oxygen Binary Phase Diagram, in *ASM Handbook: Alloy Phase Diagrams, vol. 3* (American Society for Metals, Metals Park, OH, 1992).

X. Wu: The effect of S-P gear oil on load capacity of carburized gears, in *Proc. of 4th World Congress on Gearing and Power Transmission.* (Paris, France, MCI, 1999).

Z. Yin, M. Kasrai, G. M. Bancroft, K. Fyfe, M. L. Colaianni, and K. H. Tan: Application of soft x-ray absorption spectroscopy in chemical characterization of antiwear films generated by ZDDP Part II: the effect of detergents and dispersants. *Wear* **202**, 192 (1997).

Z. Yin, M. Kasrai, M. Fuller, G. M. Bancroft, K. Fyfe, and K. H. Tan: Application of soft x-ray absorption spectroscopy in chemical characterization of antiwear films generated by ZDDP Part I: the effects of physical parameters. *Wear* **202**, 172 (1997).

Y. Yin, D. McKenzine, and M. Bilek: Intrinsic stress induced by substrate bias in amorphous hydrogenated silicon thin films. *Surf. Coat. Tech.* **198**, 156 (2005).

T. Zehnder and J. Patscheider: Nanocomposite TiC/a-C:H hard coatings deposited by reactive PVD. *Surf. Coat. Tech.* **133**, 138 (2000).

T. Zehnder, P. Schwaller, F. Munnik, S. Mikhailov, and J. Patscheider: Nanostructural and mechanical properties of nanocomposite nc-TiC/a-C:H films deposited by reactive unbalanced magnetron sputtering. *J. Appl. Phys.* **95**, 4327 (2004).

S. Zhang, H. T. Johnson, G. J. Wagner, W. K. Liu, and K. J. Hsia: Stress generation mechanisms in carbon thin films grown by ion-beam deposition. *Acta Mater.* **51**, 5211 (2003).

Y. W. Zhao, J. J. Liu, and L. Q. Zheng: The oxide film and oxide coating on steels under boundary lubrication, in *Proc. of 16th Leeds Lyon Symposium on Tribology.* (Elsevier, New York, 1990).

J. F. Ziegler: *The Stopping and Range of Ions in Solids* (Pergammon, New York, 1985). www.srim.org.